AN INVESTIGATION OF P-WAVE REFLECTIVITY OF THE SOUTHERN APPALACHIAN LITHOSPHERE USING GLOBAL SEISMIC PHASES

by

DEVON NICOLE VERELLEN

(Under the Direction of Robert Hawman)

ABSTRACT

The Southeastern Suture of the Appalachian Margin Experiment (SESAME) was designed to investigate the role of lithospheric deformation associated with Alleghanian collision and Mesozoic extension across the southeastern United States. In this study, we use zero-offset reflections generated by global seismic phases, PKiKP/PKIKP, as a virtual source to image lithospheric structure. Results from migrated images along the three profile lines of the SESAME array indicate Moho reflections from ~30 km beneath the Coastal Plain to ~45 km beneath the Blue Ridge and a lithosphere-asthenosphere boundary reflection at ~100 km. Two sets of reflectors with differing orientations, at Moho depths to ~70 km and ~70 km to ~100 km, likely indicate frozen anisotropy from fossil plate motion. Deeper reflections in the asthenosphere (~100-250 km) could indicate preserved present plate motion in the study area. These findings provide insight into the complex deformational history of the southern Appalachian system.

INDEX WORDS: southern Appalachians, global seismic phases, SESAME

INVESTIGATION OF P-WAVE REFLECTIVITY OF THE SOUTHERN APPALACHIAN LITHOSPHERE USING GLOBAL SEISMIC PHASES

by

DEVON NICOLE VERELLEN

B.S., Auburn University, 2015

A Thesis Submitted to the Graduate Faculty of The University of Georgia in Partial Fulfillment of the Requirements for the Degree

MASTER OF SCIENCE

ATHENS, GEORGIA

2017

AN INVESTIGATION OF P-WAVE REFLECTIVITY OF THE SOUTHERN APPALACHIAN LITHOSPHERE USING GLOBAL SEISMIC PHASES

by

DEVON NICOLE VERELLEN

Major Professor: Robert Hawman

Committee: Christian Klimczak
Michael Roden

Electronic Version Approved:

Suzanne Barbour
Dean of the Graduate School
The University of Georgia
December 2017

ACKNOWLEDGEMENTS

I would like to thank Dr. Robert Hawman for his tireless effort and support through this process. Without his hard work, and numerous in-house programs, the completion of this thesis would not have been possible. Additionally I would like to thank my committee members, Dr. Christian Klimczak and Dr. Michael Roden, for their patience and guidance. Finally, I would like to acknowledge the funding sources of this study: the Watts-Wheelers Fund, the Joseph W. Berg Fund, and NSF grant EAR-0844154 (R. Hawman).

TABLE OF CONTENTS

Page

LIST OF FIGURES

Page

CHAPTER 1

INTRODUCTION

Southeastern Suture of the Appalachian Margin Experiment

The Southeastern Suture of the Appalachian Margin Experiment (SESAME) was designed to investigate the role of crustal and subcrustal deformation associated with Alleghanian collision and Mesozoic extension of the lithosphere across the southeastern United States. Operational from 2010-2014, this 85-seismometer array consisted of three profiles with a total length of 1200 kilometers (Figure 1.1). The NW-SE trending D line extends approximately 200 km from the Valley & Ridge through the Blue Ridge, Inner Piedmont, and Carolina Terrane. The N-S trending W line extends approximately 530 km from the Blue Ridge in North Georgia to the Coastal Plain in Florida. The approximately 420 km N-S trending E line is entirely sediment-rooted in the Coastal Plain of southeast Georgia. A main goal of the study, and therefore a factor in choosing the array geometry, was to supplement the active source reflection profiles previously completed in the southern Appalachians by the Consortium for Continental Reflection Profiling (COCORP). The three lines of the SESAME array approximately parallel the COCORP lines (Figure 1.1) and provide information regarding the long-wavelength components of structure that complement the shorter-wavelength details imaged by COCORP. Additionally, the W and E lines cross the proposed Suwannee-Wiggins suture, which should reveal characteristics of Laurentian versus Gondwanan lithosphere and help seismically define the deep terrane boundary.

The NSF funded SESAME project has also supported outreach opportunities in the community. Bi-annual trips to the Georgia Mountain Research and Education Center in Blairsville, GA have given us the opportunity to serve the community through educational programs for local middle and elementary school students.

Geologic Setting

The Appalachian orogen was produced by a complex series of events including three major orogenies: the Taconic (480-450 Ma), Acadian/Neoacadian (409-350 Ma), and Alleghenian (330-260 Ma). The Taconic orogeny involved arc accretion (Hatcher, 2010), with age constraints from the Blue Ridge and Inner Piedmont supporting the presence of a Taconic event preserved in the interior of the southern Appalachians (Russell, 1978; Odom et al., 1982; Dallmeyer et al., 1986; Hatcher, 1989). The Acadian/Neoacadian orogeny marks the transpressional collision of the peri-Gondwanan Carolina Terrane in the southern Appalachians (Hatcher, 2010). Others, however, have speculated that the Carolina Terrane could have been accreted early in the Alleghenian (Hatcher, 2002). There is less evidence for an Acadian signature in the southern Appalachians as compared to the northern Appalachians, where the bulk of plutonic activity has an Acadian age (Hatcher, 1989; Hatcher, 2010). However, there is convincing evidence for an Acadian signature in the southern Appalachians that can be seen in the Talladega belt in Alabama and Georgia; the metamorphic grade of the Talledega belt can be correlated with the Acadian-age Murphy sequence in North Carolina (Tull, 1978; 1982; Hatcher, 1989). Next, zippered north-south collision in the northern Appalachians, followed by head-on collision of Gondwana with Laurentia in the central and southern Appalachians occurred during the diachronous Alleghenian orogeny, producing extensive northwest-trending thrust faulting with some minor dextral strike-slip components and complex folds in the southern Appalachians

(Hatcher, 1989; Hatcher, 2002; Hatcher, 2010). Taconic and Acadian structures dominate the interior of the southern Appalachians, while Alleghenian deformation dominates the flanks (Hatcher, 1989). In the Mesozoic, following the break-up of Pangea, an extensional regime, resulting in normal faulting, formation of rift basins, sedimentation, and intrusion of diabase dikes, was prevalent in the southern Appalachians (Manspeizer, 1988; Hubbard et al., 1991). This Mesozoic history is attributed to the cooling and contracting mechanisms that occurred during the extension of this time (Hatcher, 1989). This extension triggered the Central Atlantic magmatic province-related magmatism (Hames et al., 2000) that dominates much of the southern Appalachians. The Suwannee-Wiggins suture separates Laurentian crust from Gondwanan terranes that collided during the Alleghenian orogeny (Mueller et al., 2014) and separated during Mesozoic extension; it is marked by an east-west trending zone of seismic reflectors, visible on COCORP and ADCOH profiles, that truncate crustal structure and coincide with the Brunswick magnetic anomaly (Hatcher, 1989). This exotic terrane is the only remaining evidence of the completion of an entire Wilson cycle in the Appalachians (Hatcher, 1989).

Previous Work

Numerous studies, including nonseismic techniques such as gravity, magnetics, heat flow, and resistivity, have been used to study the deep structure of the Appalachians. Karner and Watts (1983), Fischer (2002), and Hawman et al. (2012) investigated gravity anomalies and their relation to lithospheric flexure, isostatic compensations, and the associated crustal root in the southern Appalachians. Other investigations of crustal thickness and average crustal compensation have used wide-angle reflections (Hawman, 2008; Hawman et al., 2012; Parker et al., 2016), broadband receiver functions (Parker et al., 2013; 2015; Hopper et al., 2017), and wavefield migration of the scattered incident P wavefield (Hopper et al., 2016). These results

reveal a thickening crust from ~30-35 km beneath the Coastal Plain to ~50-60 km beneath the Blue Ridge. However, the timing and mechanisms for preserving this crustal root beneath the Blue Ridge are still unclear (Parker et al., 2013; 2016). Parker et al. (2013) suggest the preserved crustal root is a response to Alleghenian thrust loading, however, it may be inherited from Grenville continental collision. Findings from analyses of shear-wave splitting have provided insights into the nature of anisotropy in the subcrustal lithosphere and asthenosphere (Vauchez and Barruol, 1996; Gaherty, 2004; Rychert et al., 2005; 2007; Deschamps et al., 2008; Wagner et al., 2012; Yuan and Levin, 2014; Biryol et al., 2016).

Investigations of the Coastal Plain and underlying Mesozoic rift basins (Petersen et al., 1984; McBride et al., 1987; 1989; Nelson et al., 1987; McBride, 1991; Heffner et al., 2012) have determined thickness and seismic wave velocities of the sedimentary cover. In the southern Appalachians, a thin-skinned tectonic model is supported by a combination of seismic reflection profiles (Cook et al., 1979; Coruh et al., 1987; Cook and Vasudevan, 2006) and high-frequency receiver functions (Parker et al., 2015). COCORP profiles show a zone of southward dipping reflectors in the Coastal Plain of southern Georgia that cuts across the entire crystalline crust (Nelson et al., 1987). The zone is truncated by an interpreted Moho reflection at approximately 11-12 seconds two-way time (33-36 km) and is roughly coincident with the Brunswick magnetic anomaly (COCORP lines 13, 14, 16, 19 in Nelson et al., 1987). These results support the interpretation of the Brunswick anomaly as the magnetic signature of the Alleghanian suture between Laurentia and Gondwana, possibly reactivated during Mesozoic rifting (Nelson et al., 1987). The fact that COCORP images the Moho truncating dipping reflectors possibly related to shearing indicates that the Moho is mobile and can reform (Jarchow

and Thompson, 1989). However, it is important to note that these COCORP images were not migrated, and thus may not be a true representation of the physical characteristics of the Moho.

The 1985 Appalachian Ultra-Deep Core Hole (ADCOH) experiment in the southern Appalachian Inner Piedmont and eastern Blue Ridge (Coruh et al., 1987; Hatcher et al., 1987; Hubbard et al., 1991) yields higher resolution crustal images, especially within the Inner Piedmont, than the COCORP profiles, and indicates a thinner crystalline package (2-3 km) beneath the Blue Ridge than previously interpreted on COCORP lines (6-13 km) (Coruh et al., 1987; Nelson et al., 1987). Both studies give valuable insights into structure of the crust, but because the seismic sources were restricted to frequencies greater than 8 Hz, neither was able to image structure beneath the Moho.

Imaging and interpreting the intricacies of the Moho has been a geologic target of much research throughout the world. Studies show that the Moho can be transitional with up to several kilometers that exhibit complex petrology and structure that vary laterally and with depth (Meissneer, 1967; 1973; Fuchs, 1969; Jarchow and Thompson, 1989). The continental Moho transitional zone could have many components including layers of partial melt, mantle intrusions, thrust slices of upper mantle material, or metasedimentary packages depending on tectonic history, illustrating just how variable and complex this discontinuity can be (Meissner, 1973). It has been suggested that Moho formed during the Precambrian may be difficult to image because mantle temperatures were generally higher during this time and therefore there was an increase in partial melts during the formation of the crust leading to a smoother velocity gradient. In contrast, the Phanerozoic was cooler and should exhibit a sharper transition that is more readily imaged (Jarchow and Thompson, 1989). The fact that high-frequency active source COCORP and ADCOH profiles imaged what is interpreted as Moho indicates that the Moho

must be a sharp discontinuity. However, their interpreted Moho tends to be a series of subhorizontal reflectors (~1-2 s thick) in the Coastal Plain (Nelson et al., 1987) and the Inner Piedmont and Blue Ridge (Coruh et al., 1987; Hubbard et al., 1991), indicating that the crust-mantle transition beneath the southern Appalachians does have some complexities or layering present. Layering of the Moho has also been imaged beneath the Blue Ridge using wide-angle reflection profiles (Hawman, 2008). Although it appears that the Moho over the Blue Ridge, Inner Piedmont, Carolina Terrane, and Coastal Plain is a layered, yet short-wavelength discontinuity, there are other subcrustal discontinuities that may be more transitional in nature. The lower frequencies used in passive source seismic investigations should have the ability to image transitional discontinuities, which makes these studies a valuable supplement to the active source COCORP profiles.

Thesis Overview

The principal goal of this study was to use earthquake data (in particular, reflections generated by global seismic phases) to image the lithosphere beneath the southern Appalachians. Specific targets include the Moho, structure within the subcrustal lithosphere, the lithosphere-asthenosphere boundary (LAB), and structure within the underlying asthenosphere. By using low frequency reflections, broad upper mantle structures can be constrained in addition to shorter wavelength structure previously imaged in the COCORP (McBride and Nelson, 1988; Cook et al., 1979) and ADCOH (Coruh et al., 1987; Hatcher et al., 1987; Hubbard et al., 1991) profiles, leading to a more comprehensive understanding of the mechanical response of the lithosphere to Alleghanian collision and subsequent Mesozoic extension. Additional objectives of this study are to determine an effective workflow for utilizing the global phases PKIKP and PKiKP for analysis of deep structure and to build on previous analyses in the region based on

both Sp (Abt et al., 2010; Hopper et al., 2017) and Ps (Parker et al., 2013; 2015) receiver functions as well as active source wide angle profiles (Hawman, 2008; Hawman et al., 2012). This technique aims to construct an uninterrupted profile along the provinces of the southern Appalachians to track variations in the detailed structure of the crust-mantle transition from Grenville basement beneath the Valley & Ridge to accreted terranes beneath the Coastal Plain and across the boundary between Laurentian and Gondwanan lithosphere. We also investigate the scale of layering in the uppermost mantle and its possible relation to contrasts in anisotropy.

Several seismic methods exist to image the lithosphere and asthenosphere using distant earthquakes. Both global phases (waves that travel through the core before reaching a receiver) and teleseismic phases (waves that travel through the mantle but not the core) can be used to image the subsurface. Previous work is biased toward traditional methods such as analyzing receiver functions with teleseismic waves. In this standard analysis, source side signals are removed to emphasize signals of converted P-to-S waves at layers beneath a receiver (Burdick and Langston, 1977; Langston, 1977; 1979; Dueker and Sheehan, 1997). From this, an average P-wave velocity is assumed to constrain crustal thickness and Vp/Vs ratios, which can be used to place constraints on average crustal composition. Although this can be an effective method for defining physical characteristics of sediments (Parker et al., 2013; 2015), it requires the stacking of numerous events to increase signal levels. The S-to-P conversion, generated at sharp seismic velocity gradients such as lithology changes or changes in anisotropy (Hopper et al., 2017) is also widely used to study lithospheric structure and the lithosphere-asthenosphere boundary (Abt et al., 2010; Ford et al., 2010; Kind et al., 2012).

Although these seismic techniques unveil important information regarding the nature of the lithosphere, technical problems have arisen when imaging different terranes of the

southern Appalachians. In particular, imaging the low velocity sediments of the Coastal Plain has proven difficult, as it has been plagued by multiples (Parker et al., 2016). Additionally, unveiling reflections from the crystalline-rooted Blue Ridge and Inner Piedmont has proven difficult as well (Nelson et al., 1987). For these reasons, we use the nonstandard analysis of the global seismic phases PKIKP and PKiKP to generate reflection profiles from the SESAME array. The near-vertical incidence of these arrivals should allow for the removal of multiples generated within sediments of the Coastal Plain (using standard deconvolution techniques employed by the petroleum industry) and the construction of an uninterrupted transect across the geologic provinces of the southeastern Appalachians, thus allowing for a complete evaluation of the nature of the Moho and other major discontinuities.

CHAPTER TWO

METHODS

Introduction

The method used in this study is a modification of an approach known as global phase seismic interferometry or "GloPSI" (Ruigrok and Wapenaar, 2012). This approach takes advantage of seismic phases that traverse the core, arrive at a receiver on the other side of the earth with a near-vertical incidence, and then are reflected at Earth's surface, thus acting as a virtual seismic source for generating reflections from interfaces within the crust and the upper mantle. In contrast with more widely used methods for seismic imaging such as receiver function analysis, GloPSI uses only the vertical component of ground motion. Similar approaches have been used to image targets for hydrocarbon exploration (Yu and Schuster, 2001) and deep structure beneath the Himalayas and Tibetan Plateau (Sheng et al., 2003; Ruigrok and Wapenaar, 2012).

Most previous analyses of PKIKP/PKiKP (e.g., Ruigrok and Wapenaar, 2012) have taken advantage of the equivalence of the P-wave reflection response (the wavefield recorded for a coincident source and receiver) to the positive lags of autocorrelation of the transmission response (the wavefield recorded at the surface for a source below the depth range of interest), as first noted by Claerbout (1968). The wide Fresnel zones permit stacking of results for different azimuths for ray parameters up to roughly 0.04 s/km (4.45 s/degree) to enhance signal levels. Unfortunately, in the absence of large numbers of earthquakes for stacking, the lags of the autocorrelation corresponding to the early part of the output section tend to be dominated

by energy associated with the extended earthquake source-time functions. Therefore, we have experimented with a different approach based on deconvolution of the traces prior to stacking using an estimate of the source-time function for each earthquake. This approach is similar to methods employed by Yang et al. (2012) for the analysis of teleseismic waves (waves arriving up to 90 degrees that have traveled through the mantle but not the core). In contrast with other methodologies, we show that this approach is capable of recovering useful signal levels for single earthquakes, even without stacking.

Global seismic phases include three main arrivals of interest: PKiKP, PKIKP, and PKP. PKiKP denotes the phase that reflects off the inner core and becomes prominent at distances beginning around 100 degrees from the receiver. PKIKP also denoted PKPdf, travels through the inner core and begins arriving at distances of approximately 115 degrees. Finally, PKP is a global phase that traverses the outer core but not the inner core. This phase begins arriving at approximately 145 degrees. However, seismic ray paths indicate that low velocities in the outer core cause a geometrical shadow zone from approximately 98-145 degrees, where Snell's law predicts no direct arrivals (Stein and Wysession, 2009). Beyond this shadow zone, PKP has two branches: PKPab and PKPbc (Figure 2.1). These two branches act in opposite manners, because the backward branch (PKPab) arrives with smaller angles of incidence at smaller distances, while the forward branch (PKPbc) has smaller angles of incidence at larger distances (Stein and Wysession, 2009). Although ray theory predicts a shadow zone, arrivals do occur between 98 and 145 degrees because the inner core has a higher P-wave velocity than the outer core, causing waves to refract up into the shadow zone (Stein and Wysession, 2009). Although PKP arrivals, and also S-wave core phases, can be used as virtual sources, it is the main two arrivals from the shadow zone, PKiKP and PKIKP, that we utilize in this study (Figure

2.2). These global phases arrive at near-vertical incidences due to their steep ray path, hit the underside of the array, and act as a virtual source generating near-zero offset P-wave reflections from interfaces within the lithosphere. Note the expected polarity of major discontinuities of interest in this study in Figure 2.2. The upcoming global phase, PKiKP/PKIKP, will arrive with a positive polarity from the upkick of hitting the underside of the array, but it will reverse polarity after hitting the air-rock interface at Earth's surface. Therefore, the phase will have a negative polarity as a downgoing wave, and all "hard reflections" (caused by increases in acoustic impedance), like the Moho, should have a negative polarity and decreases in acoustic impedance, like that expected at the lithosphere-asthenosphere boundary (LAB), will be imaged with a positive polarity. This is important to note for interpretation purposes later in this study.

Before outlining the steps for data selection and processing, it is important to understand the complications of using the GloPSI method. As illustrated in Figure 2.1, there are distance ranges where the three main global phases, PKiKP, PKIKP, and PKP arrive close in time within the shadow zone, causing two branches of PKP, a triplication feature with PKiKP and PKIKP, and a diffraction branch (Stein and Wysession, 2009). This distribution of arrivals, although complex, is still a simplification because it represents the arrivals as smooth lines instead of showing the possible effects of scattering due to heterogeneities in the crust, mantle, and core (Stein and Wysession, 2009). PKiKP arrives at the smallest distances of the three and is the only arrival from approximate distances of 100-115 degrees (in fact, it extends all the way back to zero degrees). PKiKP and the onset of PKIKP have similar ray paths at small distances, but they begin to diverge in ray parameter around 130 degrees. However, this divergence is fairly negligible until approximately 140-145 degrees. At these distances, the diverging ray parameters can cause difficulties in our processing methods that will be described further in the text. The

distance range from approximately 145-160 degrees is problematic as well, because the PKP arrivals have almost twice the ray parameter than that of the first arrival PKIKP (Alberts, 2017). Over the distance range from 160-180 degrees, the arrivals are well separated in time. Unfortunately, however, we do not have any earthquake events from this range. To complicate things further, we observe PKP precursors, unpredicted by ray theory, but assumed to be caused from inhomogeneities in mantle structures, which can arrive up to 20 seconds before PKIKP (Figure 2.3) (Stein and Wysession, 2009). Although they can be useful for investigating small-scale mantle heterogeneities, (Hedlin et al., 1997; Wen and Helmberger, 1998), for the purposes of this study they are a hindrance. Processing and results for each of these distance ranges (excluding 160-180 degrees due to lack of data available from the SESAME array) will be described in the next few sections of text.

Data Selection

A major goal of this study was to determine a streamlined processing technique to generate profiles from single events with usable signal levels. In order to do this, care and attention to detail was taken at each step of the process. Data from the SESAME array is available for download using the IRIS program JWEED. The criteria for choosing an earthquake for analysis include the distance range from 100-180 degrees, magnitude 6.0 and greater, and source depth of at least 50 km. Because this method utilizes the global seismic phases PKIKP and PKiKP and the SESAME array lies in the southeastern United States, most of the usable earthquakes were located in Southeast Asia. Once an event that fits the criteria above was found, it was evaluated for initial signal levels. If the signal level was adequate, the vertical components for each station along all three profiles were downloaded with the time window of 300 seconds before the PKiKP/PKIKP arrival and 600 seconds after the first S arrival.

Data Processing

Before describing the differences in processing by distance range, all generic processing that can be completed regardless of distance will be described. The vertical components from each live station along the three profiles of the SESAME array were downloaded, separated by line, and processed in the IRIS program SAC (Goldstein and Snoke, 2005) to window the length of each trace to a suitable time window of 200 seconds (20 seconds before the direct arrival of PKiKP/PKIKP and 180 seconds after) for analysis. Also in SAC, linear trends and trace means were removed. After completion of the processing in SAC, the traces were combined into one large gather, beginning with crystalline rooted stations of the D line, followed by the northern, crystalline rooted stations of the W line, then the W line stations within the Coastal Plain, followed lastly by stations of the E line (Figure 2.4). The next few steps (outlined below) were applied to the combined gather. This ensured that all three lines would be referred to a common time base.

The next stages of processing depended on the epicentral distance of the particular earthquake, because of the varying nature of interference from unwanted arrivals. At distances between 100 and 115 degrees, the only global phase present is PKiKP, but it is followed shortly after by the free surface reflection, PP. PP has a much larger ray parameter than PKiKP as illustrated in Figure 2.5, and therefore can interfere with processing and subsequent interpretations if included for reasons to be detailed shortly. To avoid complications with PP, the 200 second combination line gather, including the D, W and E lines, was windowed to remove the PP arrival from all traces (Figure 2.6). In the case of the event shown in Figure 2.6, a time window of 65 seconds (20 seconds before PKiKP and 45 seconds after) was selected. At greater distances, (beginning at roughly 120 degrees) where PKIKP is the first arrival, PP arrives much

later (90 seconds). However, each event, regardless of distance range, was either windowed to the necessary time to remove PP effects from traces or it was windowed to 110 seconds (20 seconds before PKIKP and 90 seconds after) for use in the analysis of lithospheric and asthenospheric structure.

After windowing, static corrections were employed to align the direct arrival of the global phase of interest, thus ensuring a common time base for reflections recorded at each station. This process was completed using cross correlation, a measure of the similarity between two waveforms as a function of lag time (time shift) (Dobrin and Savit, 1988), to line up the PKiKP/PKIKP arrival in the combined line gather. A near center trace from the gather was selected as the basis for correlation, and a ten second time window around the direct arrival with a maximum allotted time shift of two seconds were specified. Figure 2.7 illustrates how effective this step can be. In some cases, initial signal levels of an event may cause difficulties in uncovering the direct arrival to perform static corrections. In this case, the gather can be filtered to help determine the necessary parameters and check the effectiveness of the cross correlation. The time shifts that were applied to each trace in order to line up the direct arrival were saved in an output file that could then be used to apply the same time shifts to the original, unfiltered data (Figure 2.8). This ability opens the door for utilizing events that may have originally been discarded due to poor signal levels, and it permits keeping the nature of the event broadband instead of biasing it toward a certain frequency in the filtering.

Upon completion of the static corrections, the combined gather was separated back into individual gathers along each profile (D, W, E), all now with the same time base with the direct arrival (PKiKP/PKIKP) acting as time zero. In addition to the original three profile lines, D, W, and E, a fourth gather was generated for use in determining the source-time function

estimate of the event. The source-time function is a record of slip of the earthquake on a finite fault, and typically lasts 5-10 seconds in duration depending on the magnitude of the event (i.e. the higher the magnitude, the longer the source-time function) (Shearer, 2009). In order to remove this effect from each trace and help uncover true reflections from interfaces within the subsurface, we used the fourth gather generated from the combined line gather. This gather is composed of traces from all crystalline-rooted stations from the D line and northernmost W line. The sediment-rooted portion of the W line and the entire E line were not used in the source-time function determination because of the reverberations and scattering associated with the low-velocity sediments of the Coastal Plain. The combination gather was set up with the D line followed by the crystalline W stations for ease in extracting and generating this profile. To determine the source-time function estimate, all of the traces from this gather were vertically stacked, assuming that over the hundreds of kilometers spanned by the gather, only effects generated from the earthquake should interfere constructively and all structure should vary enough over the large distance range to interfere destructively and zero out. To check the reliability of this process, we examined the twenty second window immediately before "time zero" (i.e. the direct PKIKP/PKiKP arrival) to make sure there was no constructive interference (Figure 2.9). After the source-time function is determined, it can be removed by deconvolution.

As noted previously, in contrast with earlier approaches (e.g. Ruigrok and Wapenaar, 2012), we extract the P-wave reflection response by removing the source pulse and instrument effects through deconvolution instead of autocorrelation. By removing the earthquake source effects in this way, we allow for better resolution of upper crustal structure that has previously been masked by using autocorrelation. The deconvolution was carried out by "spectral division," i.e., completed in the frequency domain by dividing the Fourier transform of

each trace in the gather by the Fourier transform of the stacked source-time function from the crystalline stations. Then, the deconvolved gathers were inverse Fourier transformed back into the time domain, effectively suppressing source effects to a single pulse at zero time. Each profile, D, W, and E, was deconvolved using a "water level" parameter (generally 0.0001) to stabilize the deconvolution (Langston, 1979; Bostock, 1998), and a range of "alpha" values from 1-4. Alpha values control the frequency output of the deconvolution, with higher alpha values yielding sharper waveforms (Figure 2.10). A tapered highpass filter was then applied to each deconvolution output from varying alpha values to help suppress noise and uncover reflections.

If deconvolution is carried out when there is an interfering arrival, i.e. one that does not have a similar ray parameter to the direct arrival and will therefore not stack out during the source-time function generation, artifacts may be generated. This problem stems from the fact that the interfering arrival is included in the source-time function estimate and is therefore removed during the deconvolution, although it is not a representation of the earthquake source effects. Figure 2.11 illustrates the effects of leaving in traces that still have energy from the free surface reflection PP versus windowing effectively to completely remove it. Again, the arrival of this phase soon after the PKiKP arrival at small distances can cause these problems if the distance of each end member station is not carefully analyzed.

As noted earlier, PKIKP and PKiKP begin to noticeably diverge in ray parameter around 140 degrees. Figure 2.12 illustrates the effect if deconvolution of events is completed at this distance range without any special consideration. Note the coherent "ringing" in the pre-event time window, which denotes a problem with the deconvolution. This study attempted to combat this problem by generating small subsections of traces along the gather where the slopes of PKIKP and the later PKiKP arrivals were almost identical and then generating the source-time

function from the vertically stacked traces of that subsection for use in its deconvolution (Figure 2.13). After each subsection was deconvolved separately, the resulting subsections were recombined to complete the profile. Deconvolving the profile this way did effectively remove the problematic effect from the diverging PKIKP and PKiKP; however, it also appears to have removed all reflections from structure as well. The key assumption in generating a source-time function by vertically stacking traces is that the distance between the traces being stacked is great enough that structure is unlikely to interfere constructively. Thus assumption breakdown as the subsection aperture narrows. To preserve the structure sampled by the subsections, a tapered zeroing program was used to isolate the source-time function over a much shorter time window (rather than using the entire stacked trace) for each subsection for deconvolution (Figure 2.14). The resulting deconvolution appears to have artifacts similar to what was seen in the original deconvolution image, but it is likely that these are effects of PKP precursors, observed from ~118-145 degrees (Hedlin et al., 1997), that are amplified during the deconvolution process. The resulting slant stack (slant stacking is described in detail below) for one of the subsections (Figure 2.14) reveals probable lithospheric reflections around zero ray parameter that survived coherency filtering and suppression of pre-event energy. The preservation of these coherent events with limited pre-event energy illustrates the effectiveness of this process for combating the diverging PKIKP and PKiKP arrivals from 140-145 degrees.

Finally, we illustrate results from deconvolution in the distance range between 145 and 160 degrees (Figure 2.15). Notice that the PKP arrival produces artifacts if allowed to remain in the gather prior to deconvolution. To combat this, the PKP arrival can be removed due to its much different ray parameter than PKIKP (Alberts, 2017) through a process of slant stacking, the concepts of which will be discussed later. Removing interfering arrivals only works

if the ray parameters are vastly different than that of the direct arrival, which is why this is not a viable option for removing the slightly diverging PKiKP arrival in the 140-145 degree distance range. For these reasons, results in this study are limited to the distance range of 100-145 degrees.

Although the deconvolved images have the source effects removed, they were still generated from noisy earthquakes, which becomes evident when trying to make accurate interpretations of underlying reflections. For this reason, it is common practice in passive source seismology to stack numerous events to help increase signal levels. The increase in signal level is governed by the square root law (Shearer, 2009), which relates the increase in signal level to the number of events stacked. For example, stacking 16 events would result in an increase in signal levels by a factor of roughly four as compared to a single event. Six events from the E line and 9 events from the D and W lines were vertically stacked in this study to enhance signals, and the results will be discussed in the next chapter. Vertically stacking builds on the assumption discussed when generating the source-time function that if there is a waveform present at the same station and time in multiple events, then the waveform will be reinforced. If the waveforms are out of phase or not present at all, they will be zeroed out.

To further remove background noise and unveil coherent reflections, we use the process of slant stacking. Slant stacking is commonly performed using the simple Radon transform, which sums amplitudes in the time-distance (T(x)) section along linear trajectories of slope "p" and intercept time "Tau" (Phinney et al., 1981). This is completed over a range of slopes and intercepts to compute a complete slant stack (Figure 2.16). For the analysis carried out here, we used a time axis corresponding to the average distance within the spatial window, rather than the intercept (zero distance) time. This made it easier to compare events in the

original trace gather with the apparent slowness (slope) of events in the slant stack and to evaluate their level of coherence.

This technique is commonly used in seismology to enhance visibility when there is poor signal, but artifacts can be produced because of coarsely or unevenly spaced stations (e.g. the SESAME array) and edge effects (Stoffa et al., 1981; Shearer, 2009). Because slant stacking converts points in the T(x) domain into lines in the Tau-p domain, a single seismogram converts into a set of parallel lines, each with a slope given by the station distance and an amplitude related to the amplitude of the sample in the trace. Where lines in the Tau-p domain interfere constructively, they form points, and where they diverge, different frequencies cancel or reinforce causing a wedge shaped aliased region (Stoffa et al., 1981). The lines in the Tau-p domain from the near and far offsets of the original T(x) data experience only limited interference, resulting in edge effects or "alias fans" (Figure 2.17) (Phinney et al., 1981).

Although spatial aliasing can be reduced by choosing a smaller station spacing in the field, using semblance-based coherency filtering can help combat these effects as well. Semblance (Neidell and Taner, 1971) is a measure of coherency that measures the similarity in waveforms between seismic traces. Specifically, it is a measure of the power in the beam (slant stack for a particular p and Tau) normalized by the power in the original samples used to form the beam; values range from 0 (no coherency) to 1 (perfect coherency). Incoherent noise can be suppressed by setting to zero the samples for a particular (p,Tau) with semblance values less than a prescribed threshold. Semblance is a powerful tool that, in addition to suppressing background noise and enhancing signal levels, can be used to help image variations in seismic character due to structure, stratigraphy, lithology, porosity, and fluid presence (Marfurt et al., 1998) in industry and smaller scale, higher resolution seismic studies. In this study, we used a range of coherency

thresholds from 0.25 to 0.99 to increase signal levels and suppress random noise. Figure 2.18 shows a series of slant stacks with increasing coherency thresholds, illustrating that spatial aliasing artifacts, as discussed previously, and random noise are both minimized as the threshold is increased, preserving only what are believed to be true reflections with a small ray parameter range, centered around zero.

The criterion for choosing the coherency threshold was the elimination of energy prior to the direct arrival. When this optimal threshold is determined for each subsection, the slant stack with the appropriate coherency threshold can be inverse transformed back into the T(x) domain (Figure 2.16). Each subsection within a given SESAME array line can, and will most likely, have a different optimal coherency threshold. The inverse transform process causes a loss of high frequency energy, which therefore must be reintroduced by applying the first derivative of the Hilbert transform (Phinney et al., 1981). However, this step may amplify high frequency noise, so a high cut filter must be applied as well. After the optimal threshold for each subsection along a SESAME array line from a single event is determined through slant stacking and is inverse transformed, with high frequencies reintroduced, into the time domain, the individual subsections can be recombined to obtain a complete profile with background noise minimized and all coherent events preserved (Figure 2.19). This is a powerful technique for detecting weak signals for single earthquakes (Figure 2.20).

Finally, for imaging the P-wave reflectivity as an accurate depiction of the subsurface in depth, we utilize an in house 2D migration program. Standard migration algorithms require input traces that are evenly spaced. Because this requirement is violated by the SESAME array, we used a modification of an approach developed for wide-angle reflection data (Hawman, 2008). The following description is modified from Alberts (2017). Because it arrives as a plane

wave at a very steep incidence angle (nearly vertical), the PKIKP/PKiKP arrival will reflect off Earth's surface as a plane wave and travel back down into Earth along a similar nearly vertical path. Therefore it will preferentially image structures with small dips. The operation is applied to slant stacks of narrow-aperture subsections. The algorithm treats each sample in the coherency-filtered slant stack as a reflection from an interface at depth. Each reflection is assumed to arrive as a plane wave across the input subsection. The algorithm proceeds by downward continuing each sample through an assumed velocity model along a ray defined by the appropriate ray parameter, p. A reflector segment then is constructed with a dip determined by the ray parameter and layer velocity and a width controlled by the subsection aperture. The process then is repeated for neighboring (and perhaps overlapping) subsections to build a subsurface image. The edges of individual reflector segments sometimes show concave upward curvature; these "smiles" are measures of the degree of smearing of individual peaks in the slant stack, and thus serve as useful measures of the resolving power of the component subsections (Hawman, 2008).

Migration uses a velocity model to move dipping reflectors to their true subsurface location and to collapse diffractions. For this study, a series of velocity models were constructed for different stations along the SESAME array using a combination of previous wide-angle (Hawman et al., 2012) and SsPmp (Parker et al., 2016) analyses of the study area and COCORP images of Triassic rift basin and Coastal Plain sediments (McBride et al., 1987; McBride, 1991). As expected for the nearly vertical incidence angles for PKIKP/PKiKP noted above, most of the coherent energy in the slant stacks was concentrated at very low apparent slowness (-0.05 to +0.05 s/km), corresponding to small apparent dips. Because of the possibility that energy with larger ray parameters is generated by PKP precursors and therefore not indicative of true subsurface structure, we restricted the migration to this smaller range. The

traces in this range were tapered in time and distance to avoid sharply cutting off coherent events and potentially introducing artifacts. The width of the reflector segment is based in part on the Fresnel radius for plane waves, and this radius was computed using an average velocity of 7.4 km/s and a dominant frequency of 2 Hz. Subsurface structure was imaged to a depth of 300 km. The partial migrated images from individual trace subsections then were summed to generate a complete migrated profile.

CHAPTER THREE

RESULTS

A series of comparisons of several types of events was completed to evaluate and analyze the effectiveness of our modification of the GloPSI method for uncovering lithospheric structure underneath the southern Appalachians. For each comparison, events from a similar distance range were used. These comparisons include results generated from 1) shallow and deep sources, 2) small magnitude and large magnitude events, 3) single events versus stacked events, and 4) a comparison of the resolving power of vertically stacking events versus inverse slant stacking coherency filtered events. Some key examples for each profile line of the SESAME array are shown to illustrate the comparisons.

Comparison: Shallow and Deep Events

The first comparison is a test of the ability of deconvolution to remove source-side events. These phases have ray paths nearly identical to their associated parent P-wave. Otherwise known as depth phases, these arrivals are the result of a reflection from the Earth's surface near the epicenter of the event. These depth phases associated with the PKIKP and PKiKP arrivals of interest arrive soon after the direct arrival (and with almost identical ray parameters) when the source depth is shallow. Because of the similarity in ray parameters, the depth phases can be included in the estimates of the effective source-time function (Figure 3.1). If the depth phase is excluded from the source-time function estimate by zeroing out the stacked trace to include only the source estimate from the direct arrival, it is apparent in the deconvolved gather (Figure 3.2). In this case, the negative polarity reflection at ~36 seconds in Figure 3.2,

which has a similar ray parameter to the direct arrival, is clearly visible. If this underside reflection is left in the deconvolved image, it can mask true lithospheric reflections. However, if the depth phase, i.e. underside reflection, is included in the source-time estimate, it can effectively be removed through deconvolution (Figure 3.3). The comparison of Figure 3.2 and 3.3 illustrates the capabilities of our processing methods.

However, the true test of the efficiency of including depth phases is a comparison of deconvolved sections with an event that has an underside reflection in the profile and a deeper event that does not. Figure 3.4 shows a comparison of a shallow event (z=61 km), 4/11/14 m7.1, which includes depth phases in the source-time function estimate, and a deeper event (z=386 km), 7/7/13 m7.3, one of the only true deep event used in this study, where the underside reflections are not included in the windowed gather. The visibility of reflections at similar times on both of these profiles demonstrates that depth phases can be removed through deconvolution.

Previous studies (Yang et al., 2012) have had difficulties generating consistent profiles for large magnitude, shallow events, like 4/11/14 m7.1, which they attribute to the difficulty in estimating an appropriate source pulse and the complex effects of interference between source wavelet and coda waves (Langston and Ammon, 1991). Our ability to generate consistency in events of differing depths could be attributed to the fact that SESAME records broadband data, where these studies were biased to a certain frequency as controlled by the geophones used in the studies (Yang et al., 2012). The high frequency bias could result in the inability to effectively uncover reflections generated by the lower frequencies that arise from high magnitude earthquakes.

Comparison: Large and Small Magnitude Events

Comparing profiles generated for large and small magnitude events can test the ability of deconvolution to remove long-duration source-time functions associated with large earthquakes. An additional goal of this comparison is to test the ability of our processing method to pull signals from small earthquakes. Two of the truly small magnitude events (6.0-6.2) occur in the distance range with diverging PKiKP and PKIKP (~140-145 degrees). As mentioned in Chapter 2, current attempts at combating this complication appear to produce reliable results; the comparison of these events to large magnitude events outside of this problematic distance range can further support this claim. Consistent coherent events at similar times along the three profile lines of the SESAME array are visible for large and small magnitude events (Figure 3.5-3.7). This is an important result because it increases the number of events that can be used in our adaptation of the GloPSI method. Large magnitude events can be used because their long duration source-time functions can be removed through deconvolution, and now, events in the distance range with diverging PKiKP and PKIKP can be used as well.

Comparison: Single vs Vertically Stacked Events

As with the first two comparisons, this comparison aims to see if the images generated from single earthquakes are repeatable. In order to test this, nine events along the D and W lines and six events along the E line were stacked and compared to deconvolved gathers of single events with high initial signal levels. By stacking nine events, the subsequent stacked image should have three times the signal level of a single event, according to the square root law (Shearer, 2009). The stacked results along the entirely sediment-rooted E line were compared to the deconvolved E line gather using the 7/7/13 m7.3 event. As Figure 3.8 illustrates, there are consistent events; however, there is still an abundant amount of background noise. For a more

effective suppression of noise and increase of signal level, many more events would be necessary. While using the SESAME array, the number of usable events for the GloPSI method is limited; therefore, it is reassuring that the previous comparisons prove there are consistent results using a variety of event types.

Comparison: Vertical Stacking vs Inverse Slant Stacking

As mentioned above, using the GloPSI method and the SESAME array limits the number of usable events to image structure under the southern Appalachians. A goal of this comparison was to determine whether vertical stacking numerous events or inverse slant stacking single events is more effective for suppressing noise. Vertical stacking alone is limited by the square root law and therefore requires many stacked events to significantly improve signal levels. The use of numerous events is not always a luxury, depending on the analysis method chosen. However, as mentioned in Chapter 2, coherent events can be recovered through transformation into the Tau-p domain and increasing semblance-based coherency thresholds to suppress noise. Once this is completed, the slant stacks can be converted back into the Time-Distance domain. Another goal was to determine which method is more effective for recovering reflections from the lithosphere. Recall that any point that remains in the slant stack will be converted to a line in the time domain, where only the coherent events remain. Figure 3.9 illustrates the comparison of the vertically stacked E line with the inverse slant stacked E line gather for the same single event, 7/7/13 m7.3, as in the last comparison. This comparison exemplifies the power of coherency filtering as a tool for suppressing noise. It is important to note that semblance-based filtering provides a quantitative measure of waveform coherency. However, because of its sensitivity to amplitude fluctuations, if the seismic character along a single discontinuity changes laterally, the semblance-filtering technique may not preserve the

reflection. In this case, vertically stacking events may be a more reliable technique.

CHAPTER FOUR

INTERPRETATION OF MIGRATED RESULTS

The key result of this study is the generation of migrated sections for the three SESAME array profile lines from nine individual events, as well as one stacked migration image of all events for each array line (D, W, and E). The goal for this interpretation is determining the distribution of major reflectors in the southern Appalachians to a depth of 300 km, how this distribution compares with previous studies, and the information it provides regarding geologic structure. Additionally, a comparison of results along the Coastal Plain of the W and E lines was completed. Migration results from individual events were compared to the results for stacked migration, and there were consistencies. However, to analyze more complete profiles over the varying terranes in the southern Appalachians, the stacked migrated images are the only interpretations shown. Note that the edges of individual reflection segments on the migrated images sometimes show upward curvature, which, as noted in Chapter 2, are measures of smearing of peaks within the slant stacks, and therefore they can help measure the resolving power of the migration (Hawman, 2008). Also noted in Chapter 2, the migrated sections use station-specific velocity models to image the subsurface as accurately possible. Although these models incorporate layers representing low-velocity sediments of the Coastal Plain and underlying rift basins, no attempt was made to remove the effects of multiples generated within those sequences. The effects of multiples would be strongest at two-way times corresponding to the upper crust and would diminish significantly at times corresponding to the lower crust and upper mantle.

Migration results of this study focus on deeper, longer-wavelength structure than the previous COCORP (McBride and Nelson, 1988; Cook et al., 1979) and ADCOH (Coruh et al., 1987; Hatcher et al., 1987; Hubbard et al., 1991) profiles, which focus on interpreting the allochthonous and parautochthonous crust. This is due in part to the longer wavelength nature of the reflections generated from utilizing the modified GloPSI method and the minimum time window set during the migration parameters (5 seconds) to avoid migrating the direct arrival. In future studies, this minimum time window can be adjusted to try and image more crustal structure. Migration results from Line D, W, and E are shown in Figure 4.1, 4.2, and 4.3 respectively.

Depth Ranges of Prominent Reflections

The following are depths ranges for prominent concentrations of reflections found in the migrated sections along the D, W, and E line respectively. The modified GloPSI method used in this study has unveiled reflectors from new depth ranges of interest, especially below the Moho. Geologic interpretations of some of these reflectors are detailed in the next subsections of text.

D Line

Crust: Reflections from mid-crust to base of crust

Mantle: 80-100 km; 130-160 km; 220-230 km; 180-300 km on southeastern portion of profile are dipping

W Line

Crust: Reflections from mid-crust to base of crust; similar to D line, but perhaps more detailed

Mantle: 50-70 km; 100-110 km; 190-200 km; 230-260 km

E Line

Crust: Reflections from mid-crust to base of crust; reflectors are more continuous than on other lines

Mantle: 50-70 km, matching W line but more continuous here; 90-110 km; 140-150 km; 170 km; 200-230 km; 260-270 km

Crustal Reflections

There are relatively flat-lying negative polarity and positive polarity reflectors at approximately 10-15 km beneath the Blue Ridge, Inner Piedmont, Carolina Terrane, and Coastal Plain. This depth range coincides with a negative velocity gradient observed using wavefield migration of the scattered incident P wavefield (Hopper et al., 2016), and could indicate the interpreted Appalachian detachment or the presence of layered sediments (Hubbard et al., 1991; McBride et al., 2005; Cook and Vasudevan, 2006; Parker et al., 2015; Hopper et al., 2017). However, these discontinuities are likely short-wavelength features, hence the poor spatial resolution in this study. There are gently dipping, positive polarity reflectors over the proposed Alleghenian suture on the W line beginning at ~15 km depth; however, these are not clearly evident on the E line (Figure 4.4). These reflections are similar in geographic location to the steep reflectors seen on COCORP lines (Nelson et al., 1987), but no migration was completed on that study which could explain the variation in dip. Additionally, on COCORP images, this feature is a thick zone of reflections; however, the longer wavelengths used in the modified GloPSI method can only image broad structure and therefore images this zone as two sets of reflectors, likely at the top and base of the suture zone. The negative reflectors at ~30 km in the Coastal Plain, ~33 km beneath the Carolina Terrane, deepening to ~35 km in the Inner Piedmont and ~45 km in the Blue Ridge are likely indicative of the Moho (Cook and Vasudevan, 2006;

French et al., 2009; Hawman et al., 2012; Parker et al., 2013), and they seem to truncate the gently dipping reflectors on the W line. This implies that the Moho has reformed after Mesozoic rifting of Laurentia and Gondwana.

The reflections between the interpreted Appalachian detachment and the Moho are dominantly horizontal beneath the Inner Piedmont and Carolina Terrane, as seen in COCORP profiles (Cook and Vasudevan, 2006), and therefore cannot give age information about the Moho in these terranes because there are no visible truncations. As noted in previous studies (Coruh et al., 1987; Nelson et al., 1987; Hubbard et al., 1991), there are few reflections evident in the Blue Ridge as compared to the Inner Piedmont, possibly due to steeper dips present in the Blue Ridge, the presence of intrusive bodies within the Blue Ridge, or in the case of SESAME data, sparse station spacing. However, other studies note that the Inner Piedmont actually has more granitoid plutons than the Blue Ridge (Miller et al., 2000; Hatcher et al., 2007; Hatcher, 2010), indicating the likely reason for a lack of reflections in the Blue Ridge is due to steep dips or station spacing.

Other than the absence of a clear gently dipping reflector across the proposed Suwannee-Wiggins suture, results from the Coastal Plain portion of the W line and the E line are relatively consistent (Figure 4.4). One key difference between the two are relatively flat-lying reflections at approximately 12-15 km visible on the E line and not apparent on the W line. This could be an implication of the Triassic/Jurassic rift basin sediments present throughout the sediment-rooted portion of the W line, which break up the continuity of these reflectors that are seen in the E line.

Mantle Reflections

Previous Sp receiver function work in the southern Appalachians (Abt et al., 2010) revealed a possible LAB reflection at ~100 km beneath the Carolina Terrane and the

Coastal Plain. Positive polarity reflections (corresponding to negative impedance contrasts) at this approximate depth are evident along the Inner Piedmont, Carolina Terrane, and Coastal Plain, which is the expected polarity for the LAB. If this discontinuity is not indicative of the LAB, it could represent the top of a melt cumulate zone or the lower boundary of an ancient, highly depleted layer of lithosphere (Abt et al., 2010). Above the possible LAB at ~90-95 km, there are prominent subhorizontal negative polarity reflections, which could indicate the Hales discontinuity, marking the phase transition from spinel to garnet peridotite (Hales, 1969). Previous studies have placed this discontinuity at a depth range of 70-115 km (Bostock, 1998; Levin and Park, 2000; Snyder, 2008).

Geodynamic models in the Phanerozoic eastern US predict broad thermal gradients between the lithosphere and the asthenosphere, coupled with moderate mantle upwelling (Abt et al., 2010), indicating a need for mantle hydration, fertility, and/or melt content to sharpen the gradual velocity contrast at the LAB expected by temperature alone (Fischer et al., 2010). The presence of the Central Atlantic magmatic province over much of the study area indicates that there is a large melt content originating from lithospheric processes that drive upper mantle melt generation (Hames et al., 2000). In the case of the interpreted LAB reflection at ~100 km depth, it is possible that the lack of clear reflections for this discontinuity under the deep crustal root of the Blue Ridge is an indication of a transition to a more thermal boundary (Abt et al., 2010).

The motion between the asthenosphere and the tectonic plates of the overlying lithosphere is accommodated at the LAB by either diffusion or dislocation creep (Eaton et al., 2009). Diffusion creep occurs with small grain size and/or low stress levels, where dislocation creep occurs with large grains sizes and/or high stress levels, resulting in the development of

lattice-preferred orientation, typically of olivines, within the mantle (Eaton et al., 2009). This change to lattice-preferred orientation can help explain the prevalence of anisotropy in the upper 200 km of the mantle. Laboratory studies from Eaton et al. (2009) indicate that dislocation creep dominates in the asthenosphere and lowermost lithosphere. While this change in creep mechanism can occur much shallower in the lithosphere depending on water content present (Eaton et al., 2009), it is likely, in the case of the hydrated lithosphere present in the southern Appalachians, that this boundary will coincide closely with the expected LAB. This change from diffusion creep to dislocation creep can also indicate the expected boundary between "frozen" anisotropy in the lithosphere to preserved present plate motion in the dislocation creep dominated asthenosphere (Anderson, 1979; Eaton et al., 2009).

Lithospheric and Asthenospheric Anisotropy

If the discontinuity at ~100 km is the LAB, then the complex reflections between Moho depths to ~100 km could be a manifestation of the intricate lithospheric anisotropy beneath the accreted terranes of the southern Appalachians (Wagner et al., 2012), while the reflections at greater depth (~150-250 km) could be indicative of present plate motion. The negative polarity reflections, resulting from an increase in acoustic impedance, at 270 to 280 km could represent a reflection from the base of an asthenospheric low velocity zone (Li et al., 2002). Southeast dipping reflectors beneath the proposed LAB are clearly evident on the D line migration (Figure 4.1) from ~100-300 km, but the origin of these reflectors is difficult to explain; corresponding reflectors on the W and E lines are relatively horizontal. Deschamps et al. (2008) have identified two zones of lithospheric anisotropy, 30-70 km and 70-150 km, from shear-wave splitting, which record motion parallel to the Grenville and Appalachian fronts and plate motion during the Mesozoic respectively. Note that Deschamps et al. (2008) observe stratified

anisotropy to depths of ~150 km, indicating a deeper LAB than proposed in this study; however, that study included areas of the interior craton of the southern United States where a deeper LAB would be expected. In this study, we notice reflectors beneath Moho to ~70 km depth, but the profiles of the SESAME array are out of plane with the NE-SW direction of the Grenville and Appalachian fronts. Reflectors from ~70 km to the base of the lithosphere (~100 km) have a northern dip, which is most evident on the E line. These preserved layers of anisotropy contain a record of lithospheric evolution of the southern United States, which involved at least two distinct phases of thickening as indicated by the differing directions of anisotropy present (Deschamps et al., 2008).

CHAPTER FIVE

CONCLUSIONS

This study has important implications for geologic insight into the southern Appalachians as well as the utilization of the modified GloPSI method for generating lithospheric and sub-lithospheric reflections. We use semblance-based coherency filtered slant stacks to ensure only coherent signals are migrated and not noise. This leads to migrated sections along the three profile lines of the SESAME array that image detailed structure from mid-crust up to 300 km depth across a complete transect from the Blue Ridge to the Coastal Plain, with relatively high frequency content as compared to Sp receiver function analyses. Key possible interpretations from these migrated images include:

- Appalachian detachment from ~10-15 km in Blue Ridge, Inner Piedmont, and Carolina Terrane
- S-dipping reflectors in Coastal Plain relating to SWS
- Moho reflections from ~30 km beneath the Coastal Plain to ~45 km beneath the Blue Ridge
- Anisotropy from fossil plate motions:
    - Moho depths to ~70 km
        - Grenville or Appalachian fronts
    - ~70 km to LAB (~100 km)
        - North America relict plate motion in Mesozoic
- Hales discontinuity at ~90-95 km

- LAB at ~100 km
- Anisotropy from present plate motion ~100-250 km
- Base of low velocity zone in asthenosphere at ~270-280 km

The workflow generated in the study has proven effective for removing underside reflections, large duration source-time functions, combating the 140-145 degree distance range where PKIKP and PKiKP diverge, and unveiling coherent reflections from individual earthquakes. Future work utilizing the methods from this study include slant stacking and coherency filtering subsections for individual events over a wide range of alpha values to see if varying the frequency output of the deconvolution can better image different lithospheric discontinuities. Then, migration outputs of these varying frequencies can be added together for a more complete subsurface image. Additionally, more work can be completed to combat crustal multiples, such as predictive deconvolution techniques (Robinson and Treitel, 1980; Yu et al., 2015).

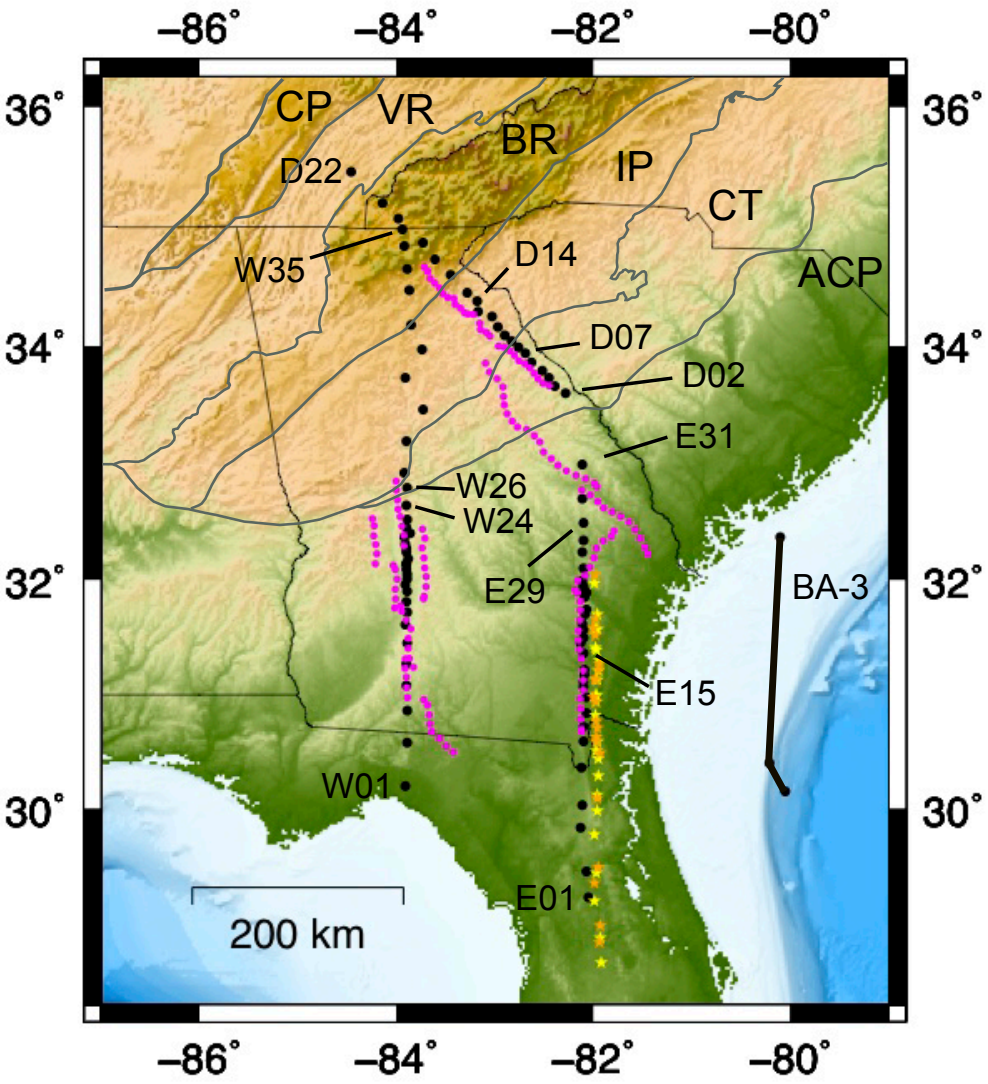

Figure 1.1 This figure is from Parker et al. (2016). The black dots indicate stations of the SESAME broadband array, which is divided into three profiles. The NW-SE trending Line D is approximately 200 km and extends from the Valley & Ridge through the Blue Ridge, Inner Piedmont, and Carolina Terrane. The N-S trending Line W is approximately 530 km and extends from the Blue Ridge in North Georgia down to the Coastal Plain in Florida. The final line of the SESAME array is the approximately 420 km N-S trending Line E that is entirely sediment rooted in the Coastal Plain. These

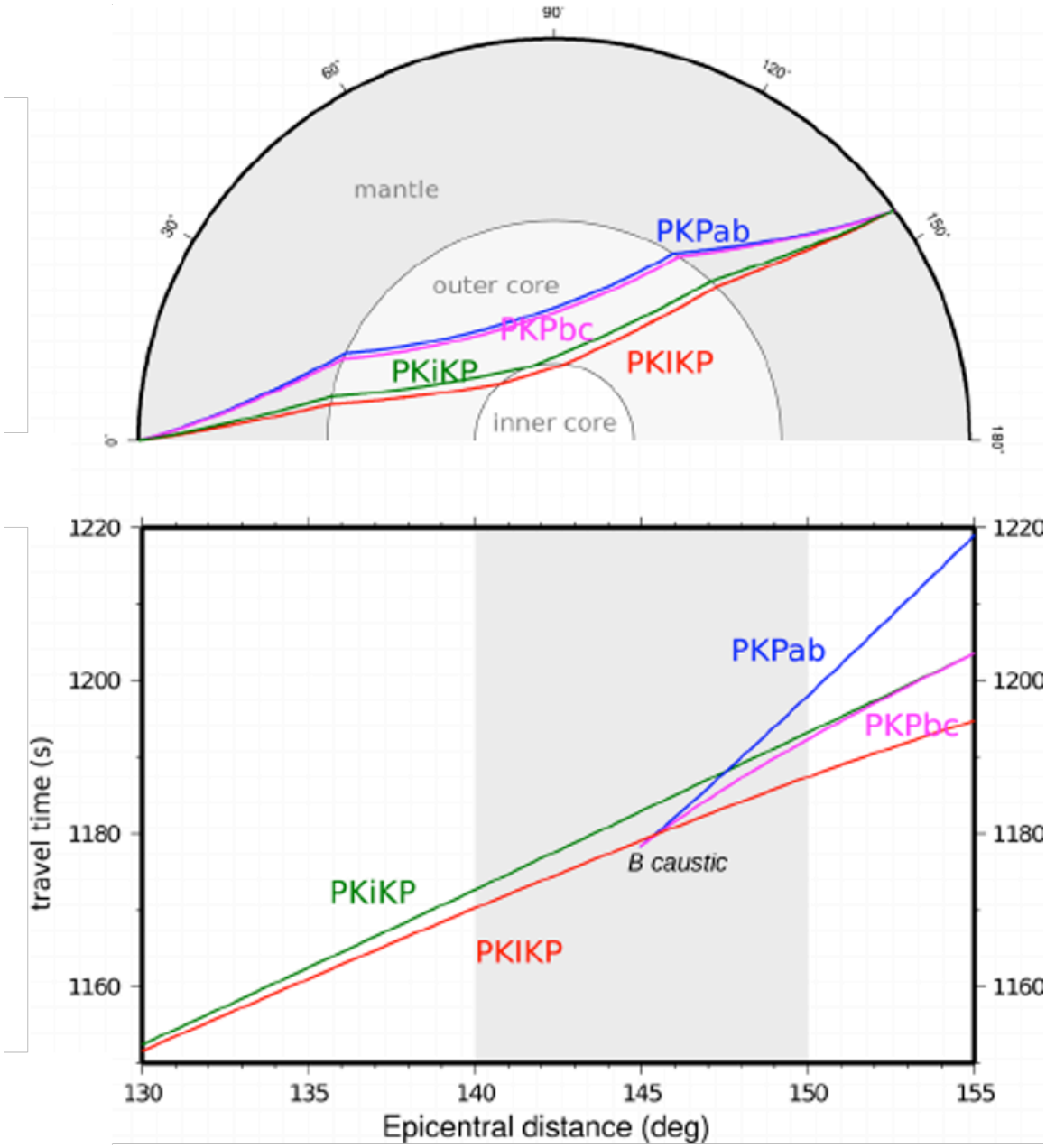

Figure 2.1 An illustration of the expected arrival times and distances of the global seismic phases, PKiKP, PKIKP, and the branches of PKP (PKPab and PKPbc) from Ma et al. (2016). Notice the varying ray parameters of these arrivals with distance.

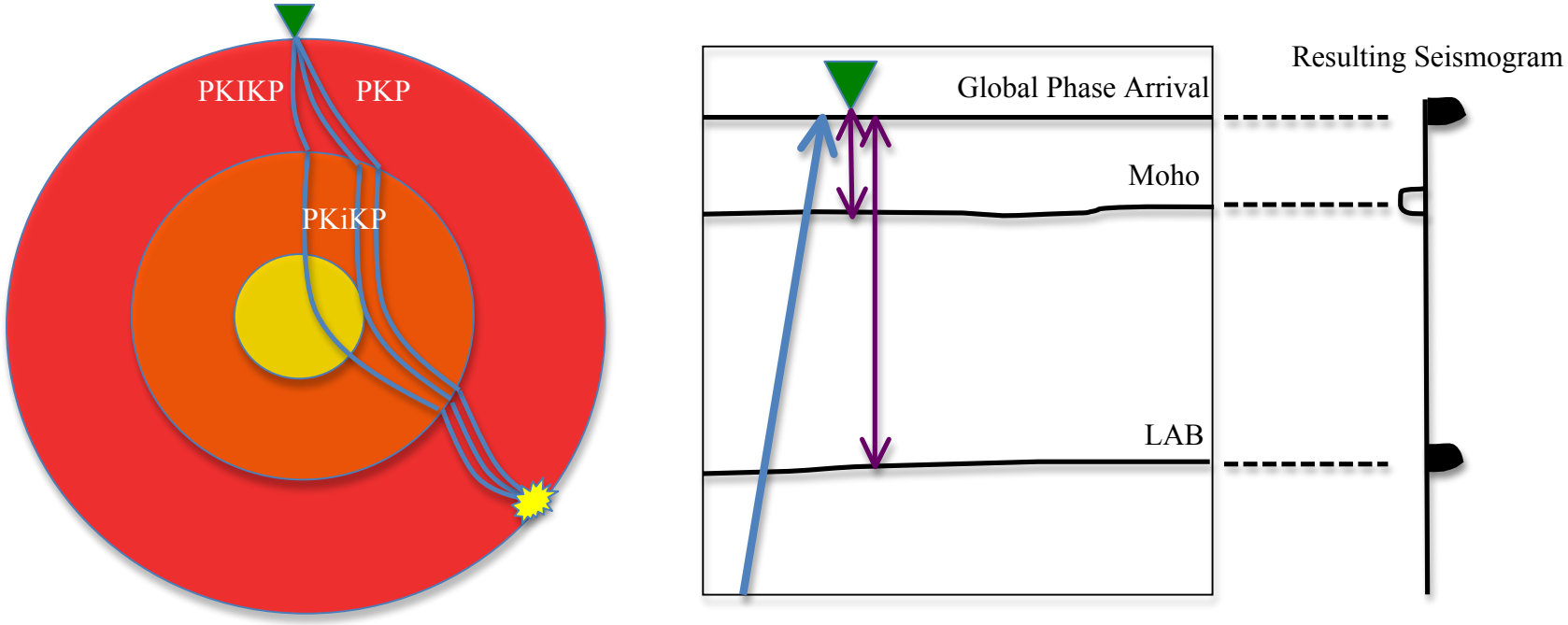

Figure 2.2 The GloPSI method can utilize any global seismic phase, but of particular interest are the arrivals PKIKP, PKiKP, and PKP. PKIKP travels through the inner core, while PKiKP reflects off of the inner core boundary, and PKP traverses the outer core (Figure regenerated from Ruigrok and Wapenaar, 2012). All of these phases arrive at a seismic receiver on the other side of the earth at near vertical incidence, where they reflect off of the surface and act as a virtual source for reflections off of lithospheric discontinuities (as illustrated by the purple lines). Finally, note the expected positive polarity of the direct, global phase arrival, the negative polarity of the Moho, and the positive polarity of lithosphere-asthenosphere boundary (LAB). Negative polarity events will result from increases in acoustic impedance, while positive polarity events will result from decreases in acoustic impedance.

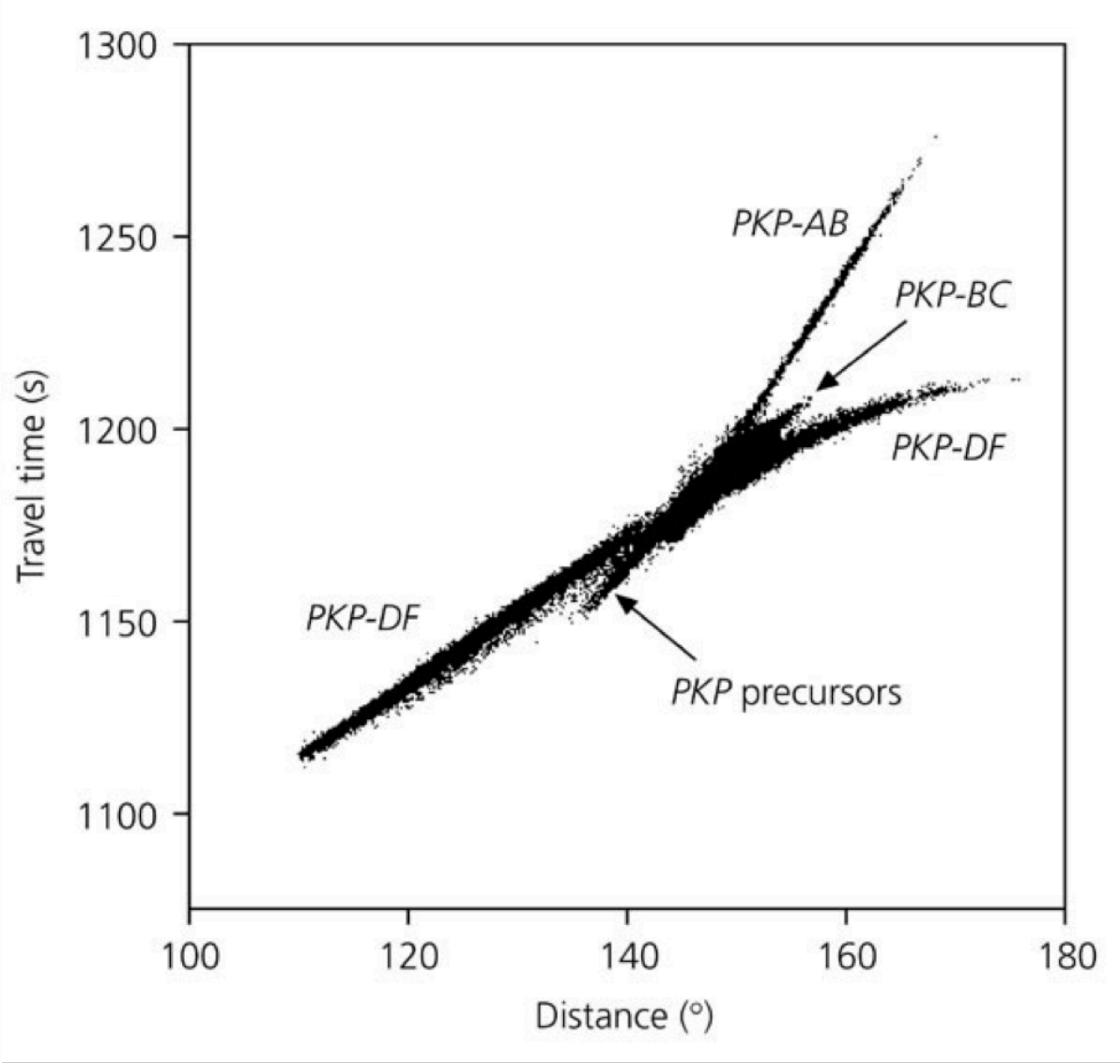

Figure 2.3 This image from Stein and Wysession (2009) illustrates the arrival of PKP precursors, which appear to be a continuation of the PKPab branch. These precursors, with their large ray parameters, yet not as steep as PKIKP, can arrive up to 20 seconds before the PKIKP (PKPdf) arrival, causing complications in our processing steps and subsequent results.

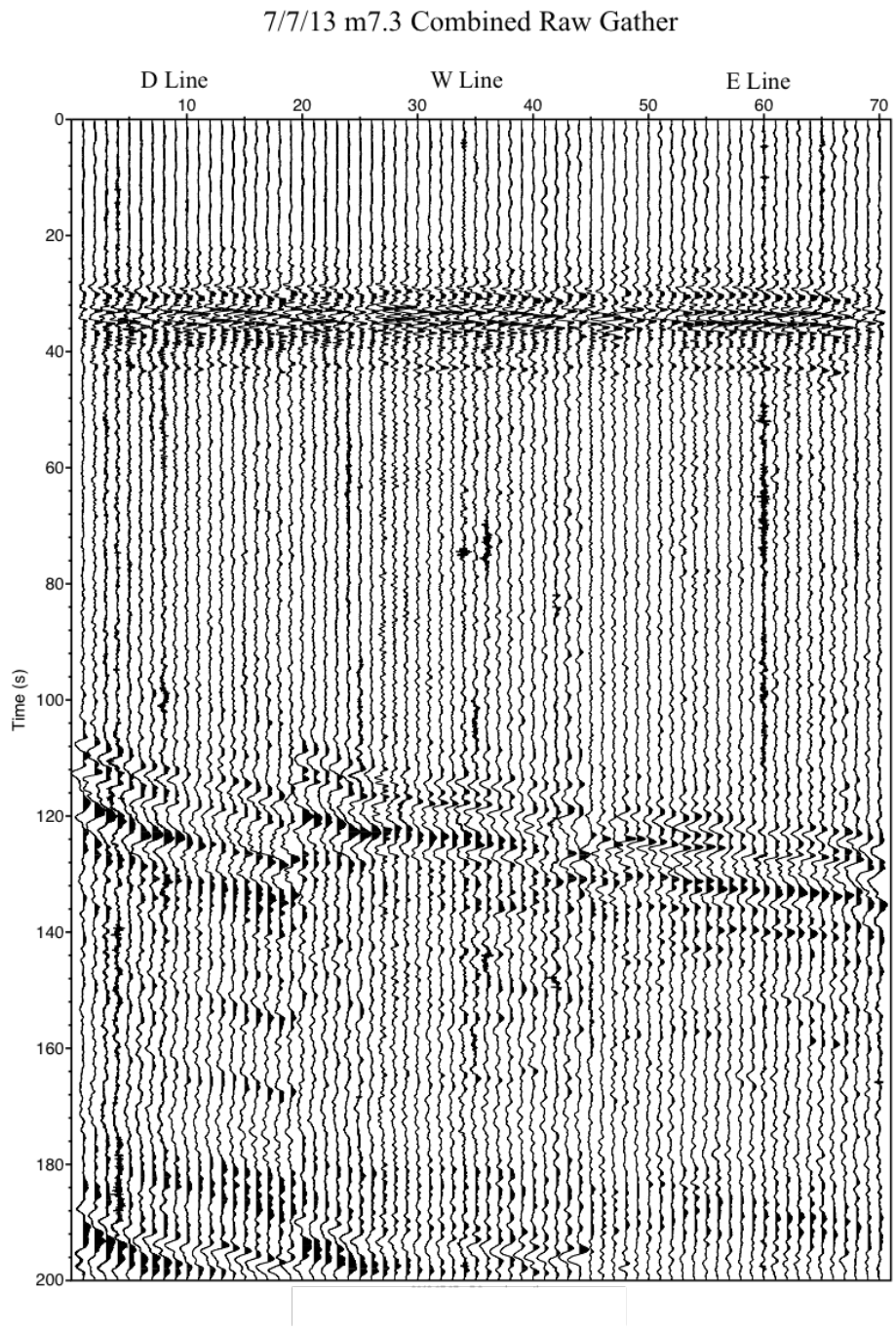

Figure 2.4 After reviewing the quality of individual traces in each line from the preliminary gathers, a combined gather is made with traces from all three lines of the SESAME array to ensure a common "zero-time" reference. Line D is plotted on the far left, starting with the northernmost stations of the Valley & Ridge, Blue Ridge Mountains, and Inner Piedmont, followed by the northern portions of the crystalline line W to the stations of the Coastal

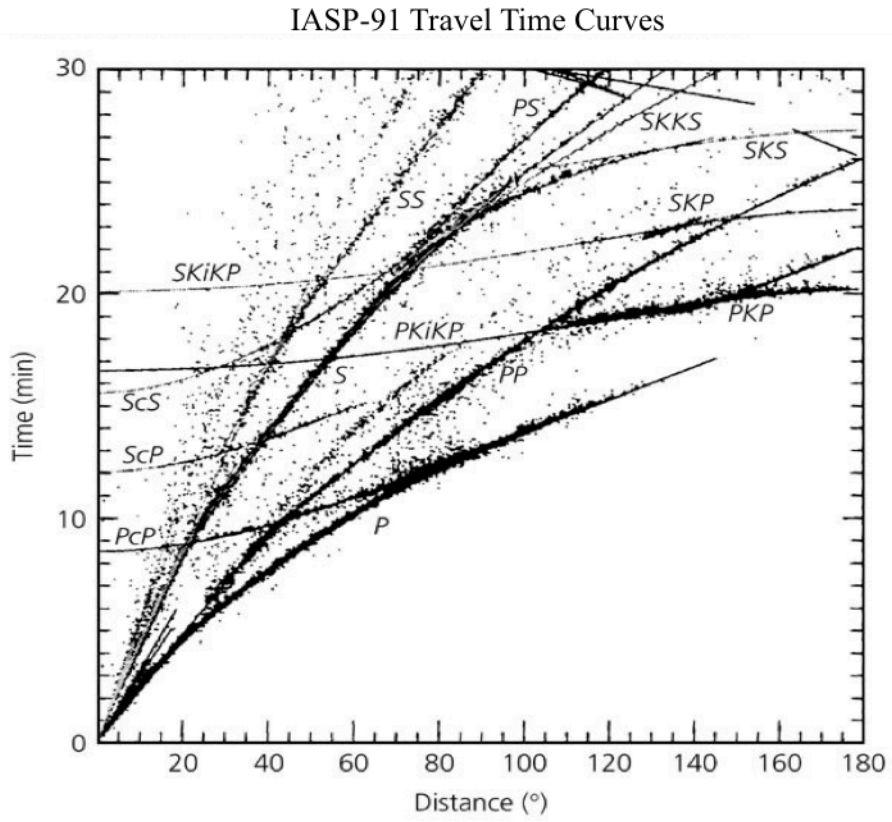

Figure 2.5 The travel time curves (Stein and Wysession, 2009) generated from IASP-91 indicate the distance range (~100-120 degrees) where the free surface reflection PP arrives shortly after the direct PKiKP of PKIKP arrival.

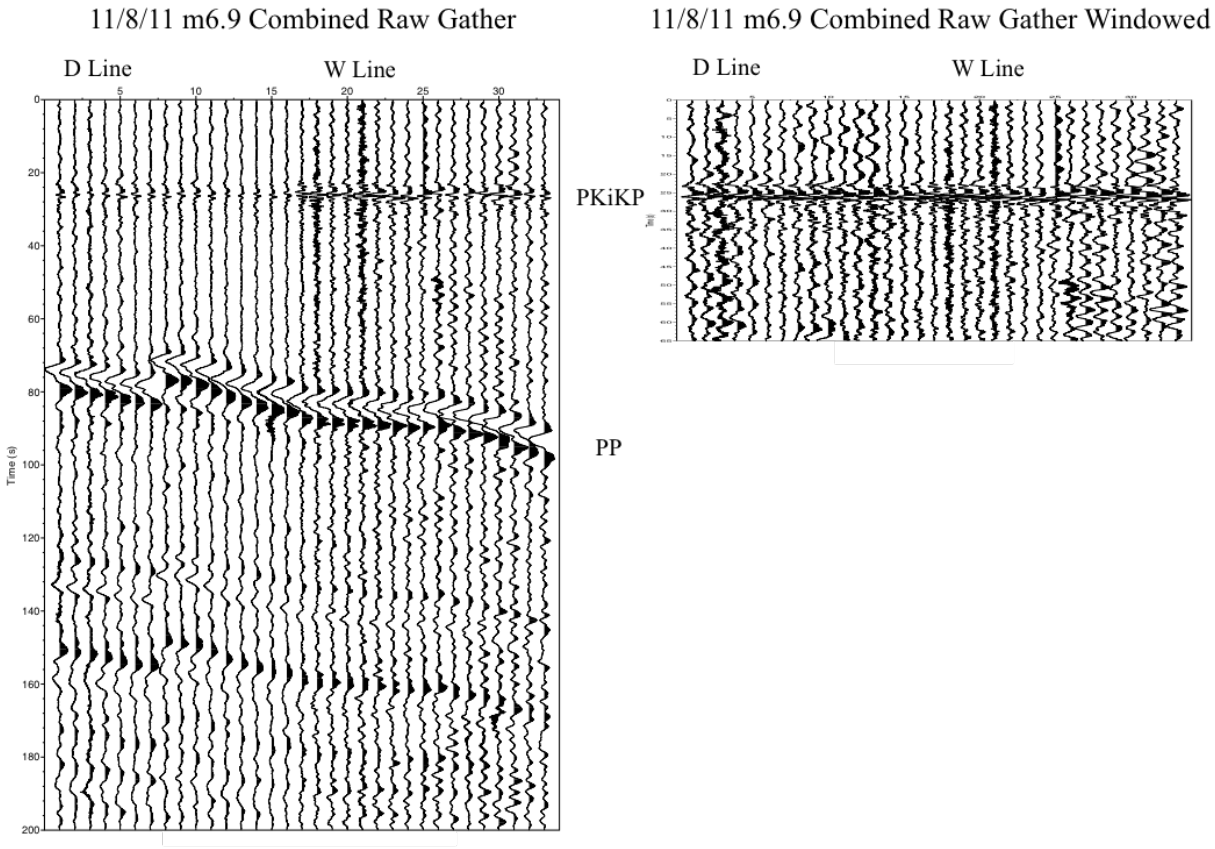

Figure 2.6 On the left, **t**he interfering arrival of PP arriving approximately 50 seconds after the direct PKiKP arrival for the magnitude 6.9 event on 11/8/11 (Δ=113 degrees) can clearly be seen to have a different ray parameter than PKiKP. On the right, the combined gather has been windowed to 65 seconds in order to remove the PP arrival from all traces.

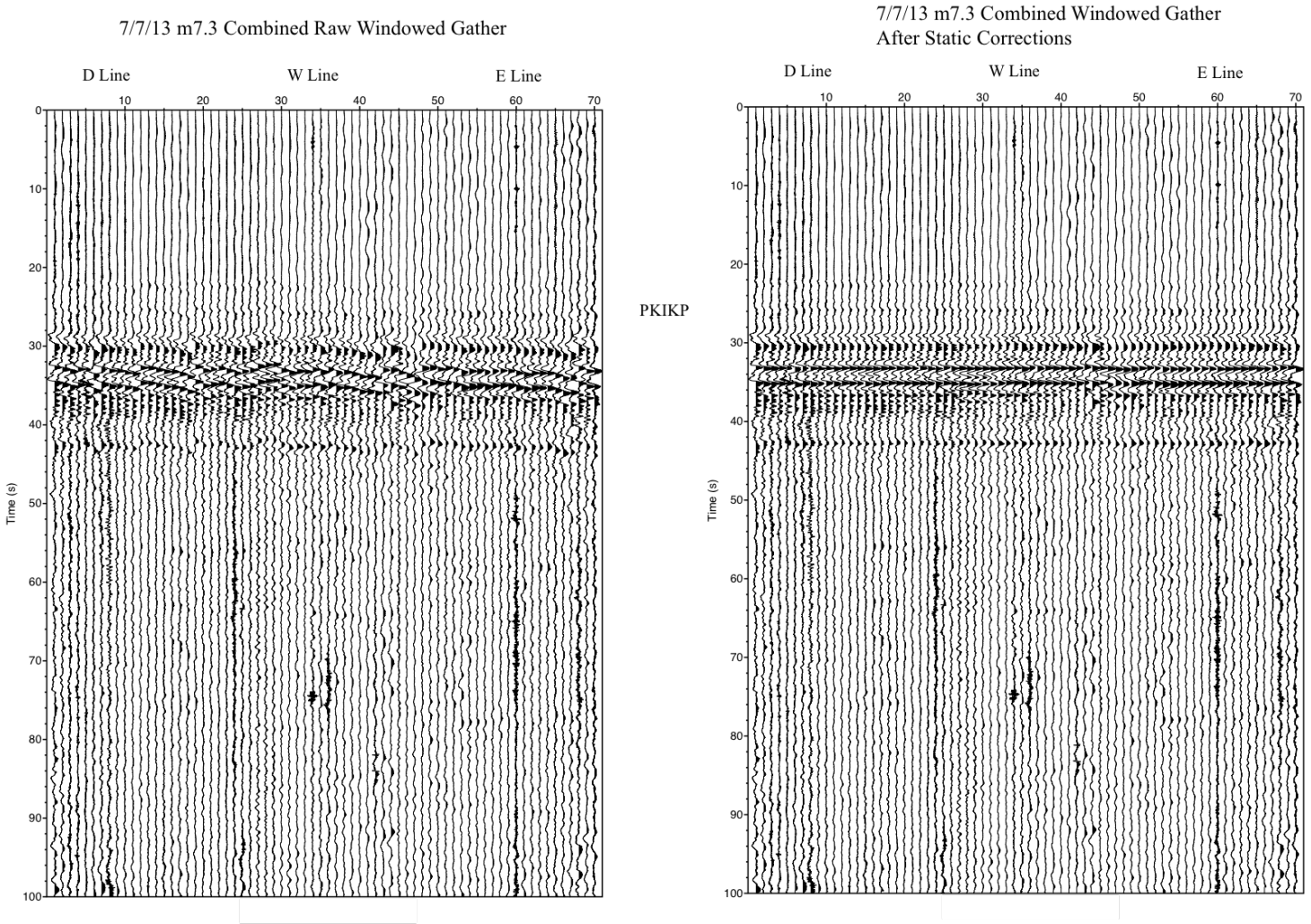

Figure 2.7 After windowing to ensure the removal of any effects from PP, the combination gathers are statically corrected, using cross correlation, to line up the direct PKIKP arrival. The image on the left is the raw gather, and the image on the right is the gather after static corrections. This example is the 7/7/13 m7.3 event, which has very good initial signal levels sue in part to its large magnitude.

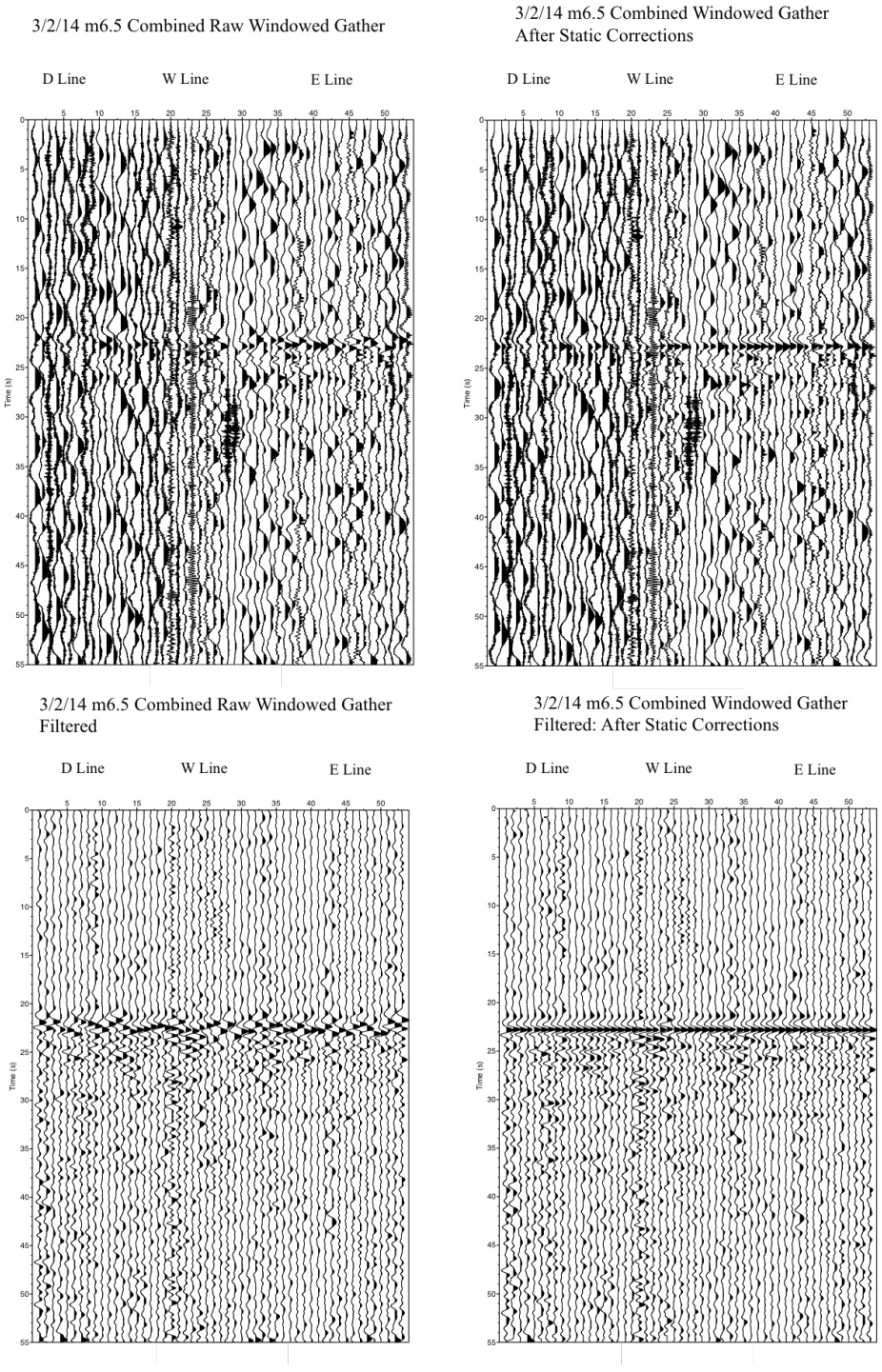

Figure 2.8 Bandpass filtering can be used to suppress noise in order to perform static corrections, as in this example for the 3/2/14 m6.5 event. The necessary time shifts for the corrections can then be applied to the original, unfiltered data to preserve its broadband nature. The top two images illustrate the raw, unfiltered data and the subsequent static corrections applied and the bottom is the filtered data.

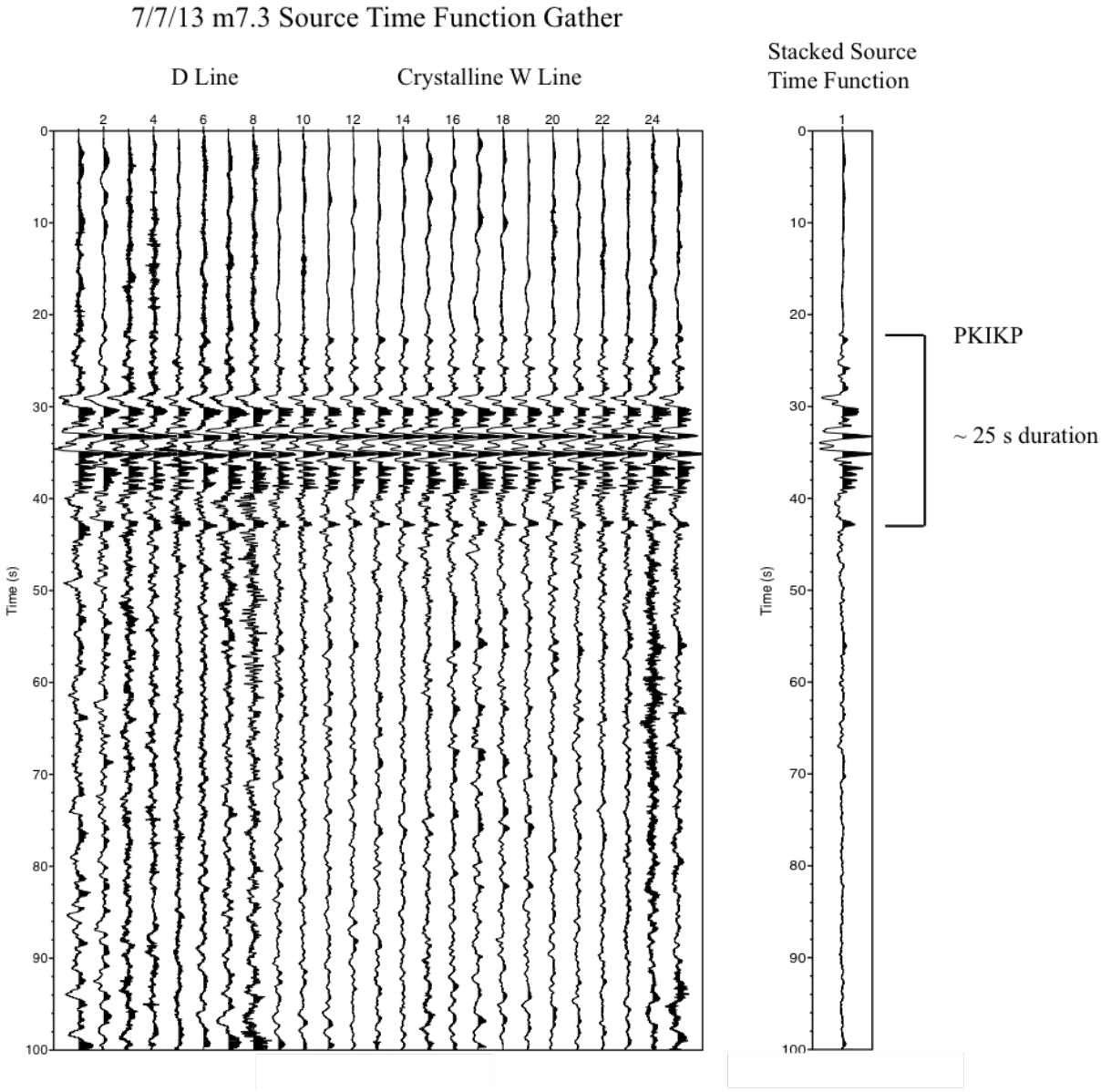

Figure 2.9 The source time function, a manifestation of the finite slip of the earthquake, can be determined by stacking individual traces from the crystalline rooted stations of the D and W lines. The image on the left is the source-time function gather generated with these stations, and the image on the right is the result of vertically stacking. Notice how the pre event time (0 - ~20s) is zeroed out, as well as deeper structure. The large magnitude of this event (m=7.3) yields a long duration source-time function.

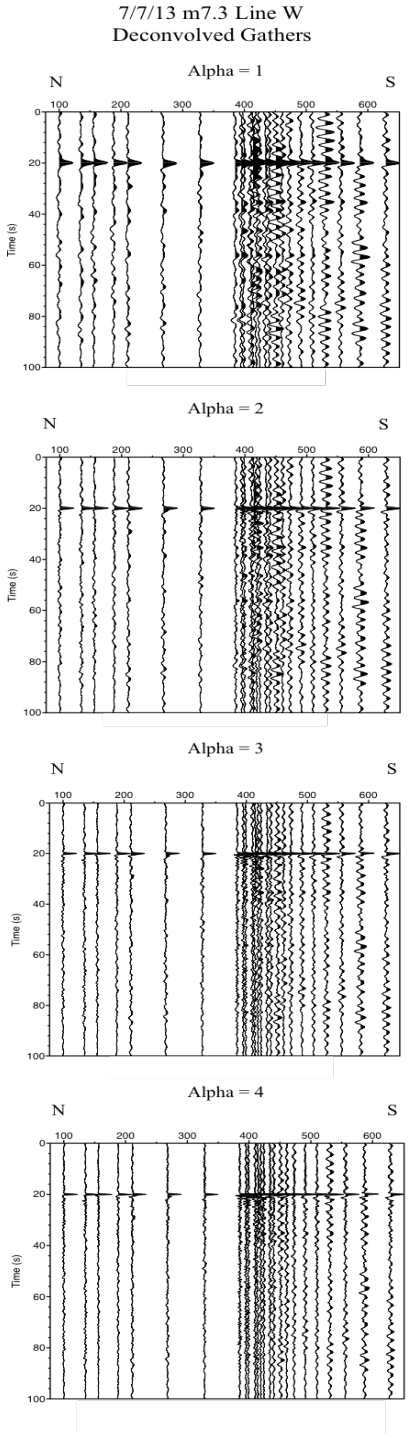

Figure 2.10 This figure illustrates the effect of the alpha parameter, which controls frequency outputs of deconvolved sections. These results from the W line deconvolution of the 7/7/13 m7.3 event show the lowest alpha value used in this study of 1 in the top plot, increasing to the highest alpha value used of 4 in the bottom plot. Note the increase in the sharpness of the

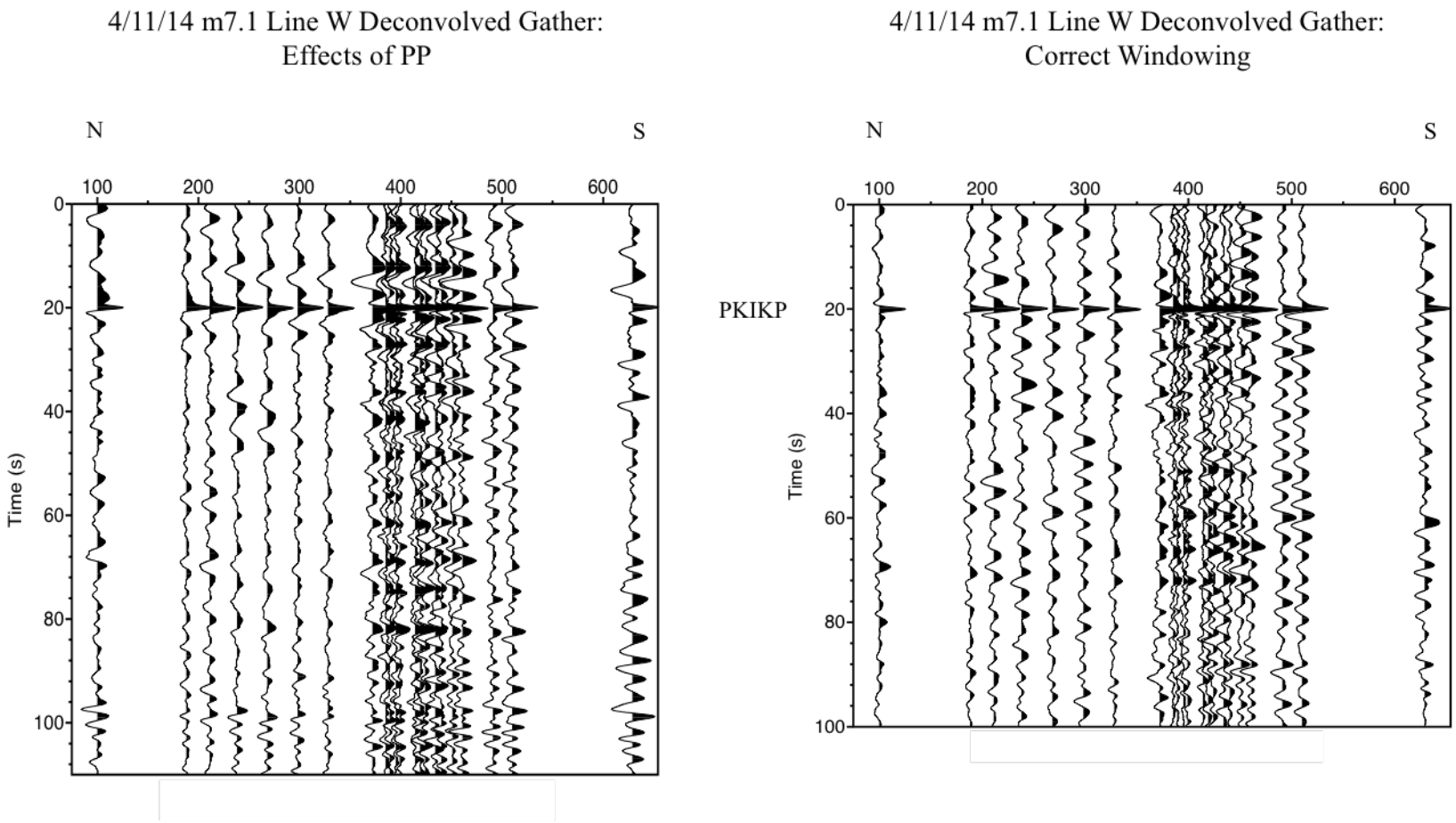

Figure 2.11 The image on the left shows the deconvolution results (alpha=2) of the W line for the event 4/11/14 m7.1 when initial windowing unintentionally included a trace that included the free surface PP arrival, which was included in the source-time function estimate. When windowed correctly to completely remove this interfering arrival, there is less pre-event coherency in the deconvolution (alpha=2) results in the image on the right. Pre-event coherency or continuity of waveforms are an indication that the deconvolution has some sort of interference that is causing these artifacts..

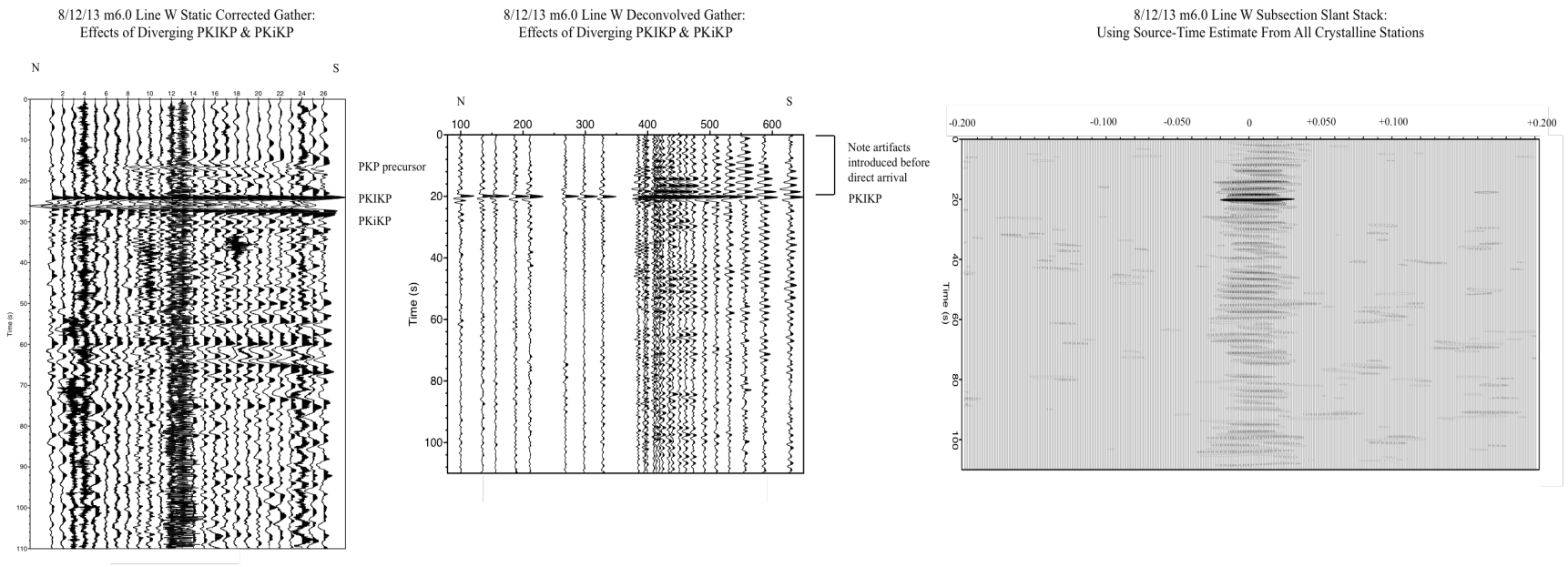

Figure 2.12 Deconvolution in the distance range of 140-145 degrees can be problematic, as illustrated by the deconvolved profile of Line W for the magnitude 6.0 event on 8/12/13, if the slightly diverging ray parameters of PKIKP and PKiKP are not addressed. The diverging arrivals can be seen in the statically corrected Line W gather on the left; however, it is important to note that the traces are plotted evenly instead of with true spacings.

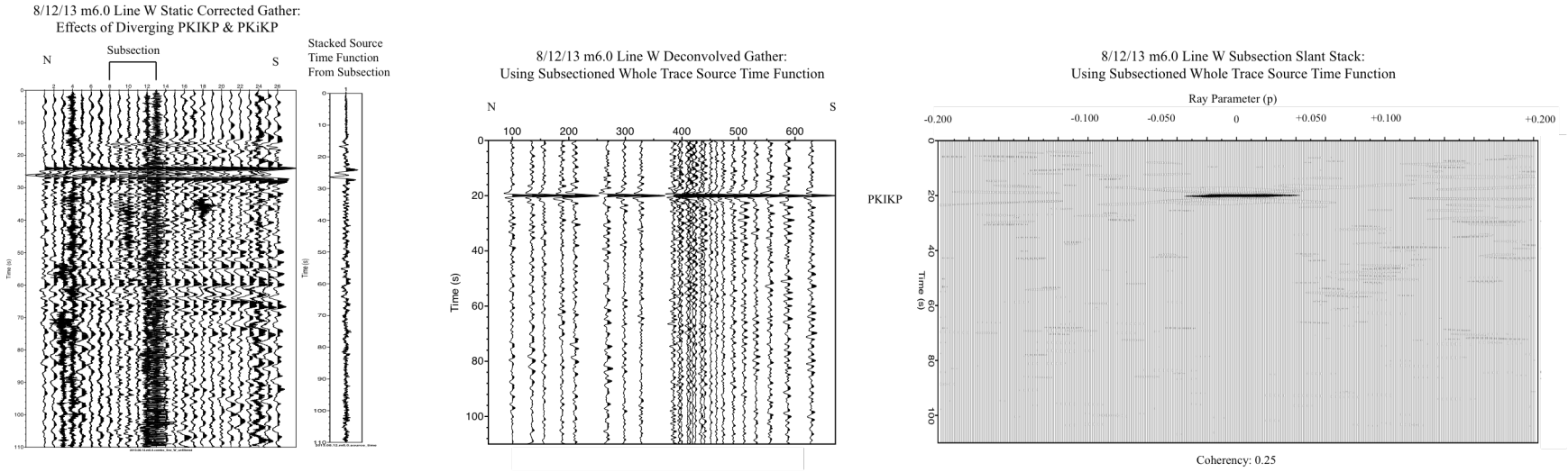

Figure 2.13 When using the whole stacked trace from small subsections for use as the source time function estimate, all structure is zeroed out during deconvolution. Note that pre event time has not been zeroed out on the source time function estimate because the trace spacing of the small subsections is not large enough to cause noise or structure to interfere destructively when stacked. This is evident by the complete lack of seismic energy in the slant stack at zero ray parameter, even on the lowest coherency threshold used of 0.25.

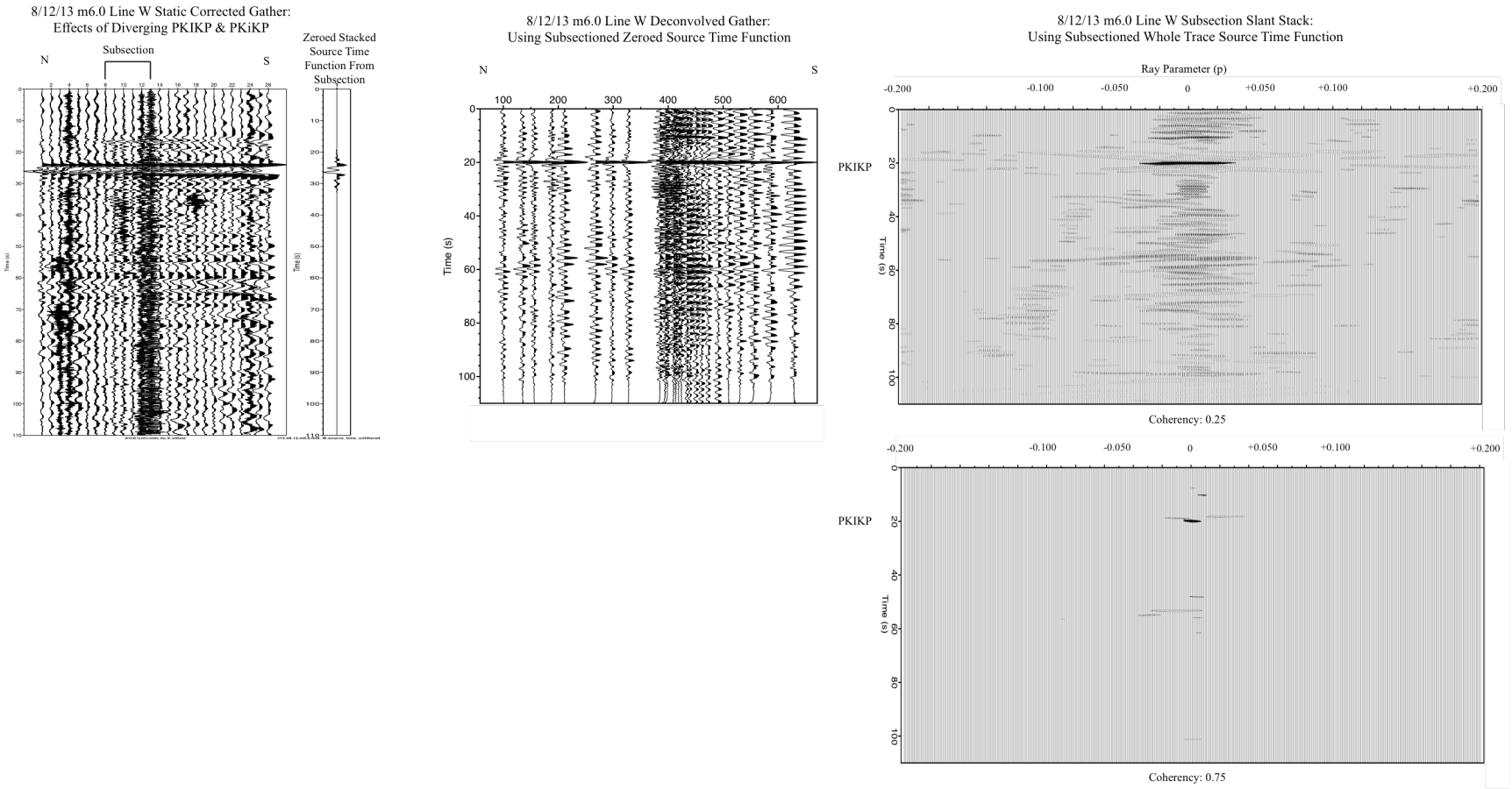

Figure 2.14 Deconvolution of this event using a tapering program to zero out all seismic energy other than the generated source time function for each subsection appears to introduce artifacts. However, these are likely manifestations of PKP precursors, although they do have similar ray parameter to the direct arrival and underlying reflections. The visibility of energy at a near zero ray parameter that can be preserved as the coherency threshold is increased is evidence of the effectiveness of this processing technique.

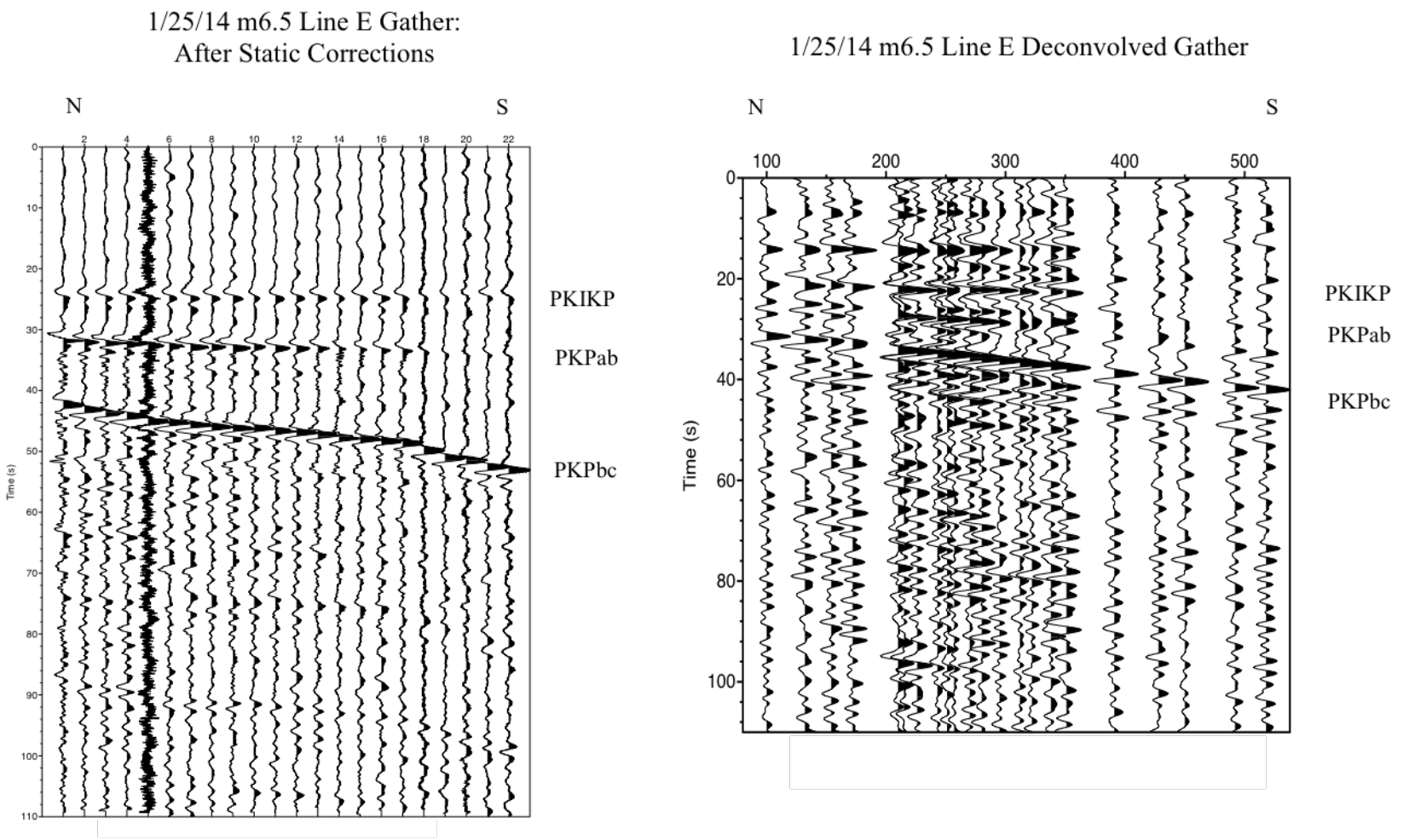

Figure 2.15 The statically corrected gather (left) and the deconvolution for Line E (right) of the event on 1/25/14 m6.1 side by side show the effects of PKP. PKPab comes in too soon after PKIKP, followed by PKPbc. Both PKP arrivals have much different ray parameters than PKIKP, which will not stack out in the generation of the source time function, and therefore, cause artifacts in the deconvolution and masks true reflections.

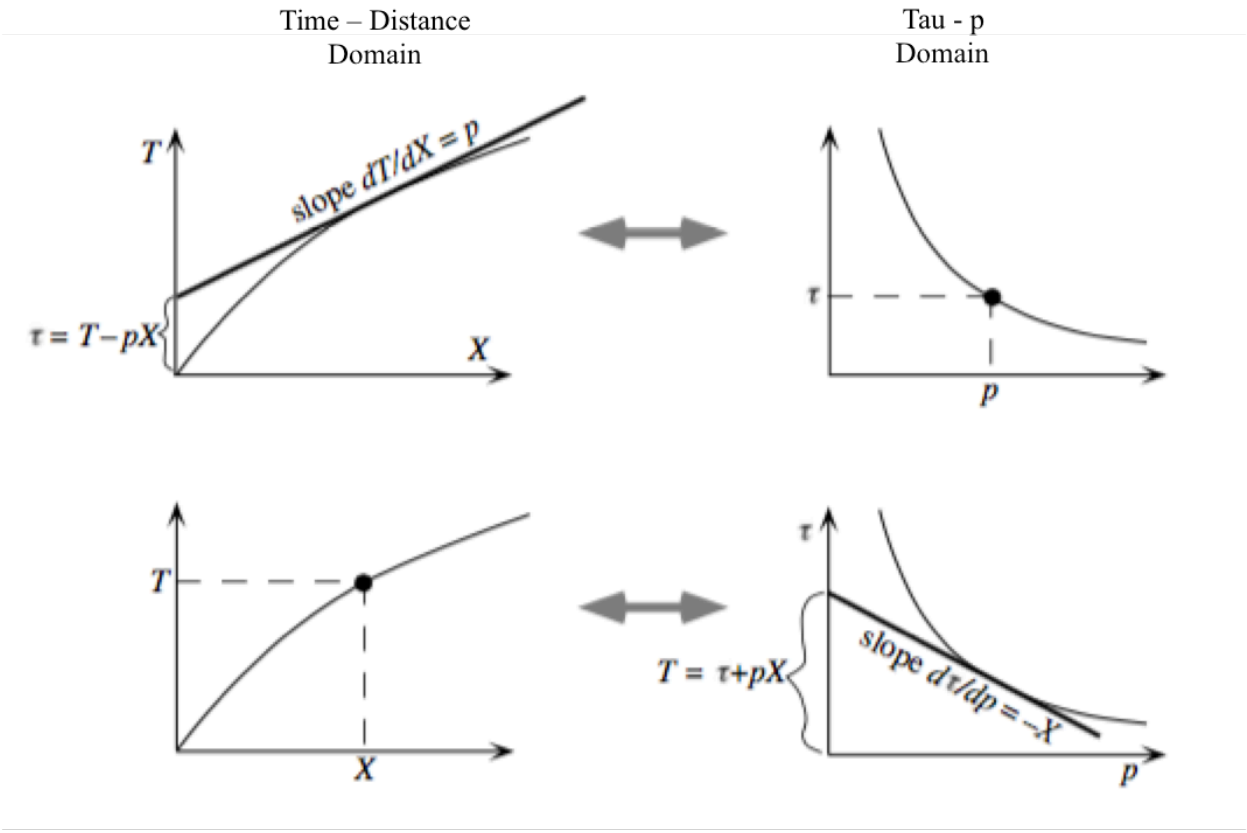

Figure 2.16 This diagram from Shearer (2009) illustrates the conversion from the T(x) domain to the Tau(p) domain and vice versa. Lines in the T(x) domain and converted to points in the Tau(p) domain.

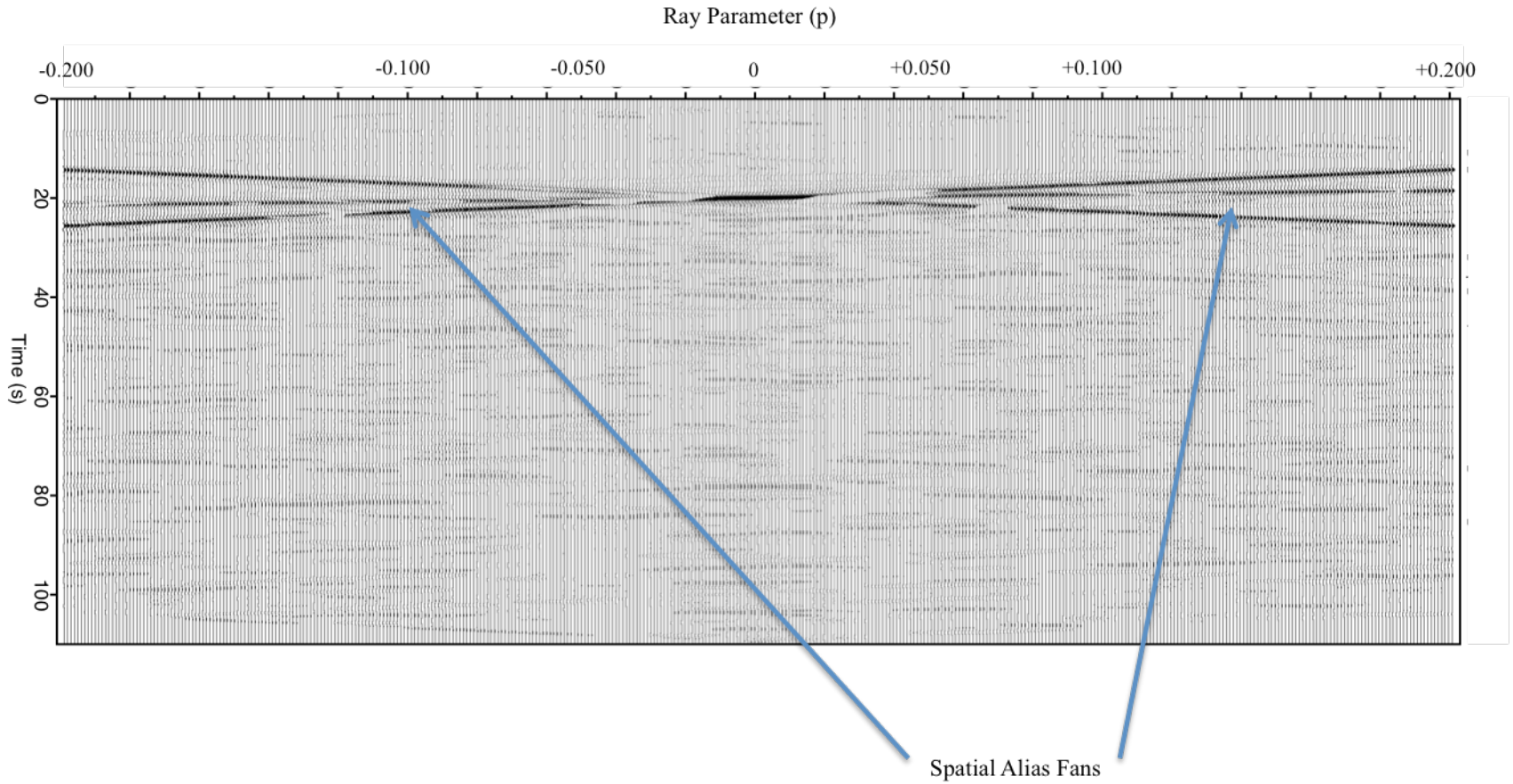

Figure 2.17 Spatial alias fans are present on the near and far offsets of the subsection, and the direct arrival of PKIKP is focused at a zero ray parameter.

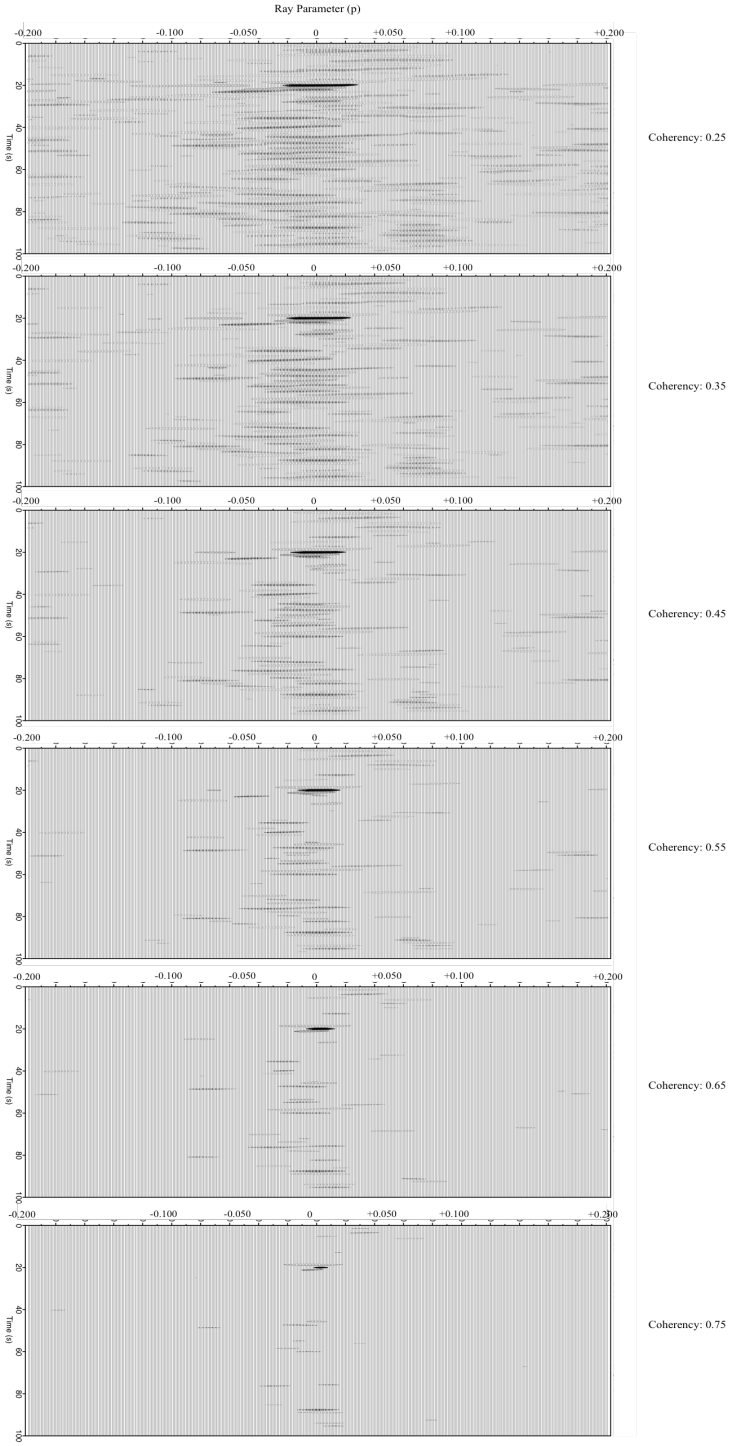

Figure 2.18 The top image, with a low coherency filter of 0.25, has a lot of background noise, but this is removed as the coherency threshold is progressively increased to 0.75 in the bottom image. Note that only energy with low ray parameter (p) is preserved (low p = small dip). These slant stacks were generated from the m7.1 event on 4/11/14 for a subsection along the

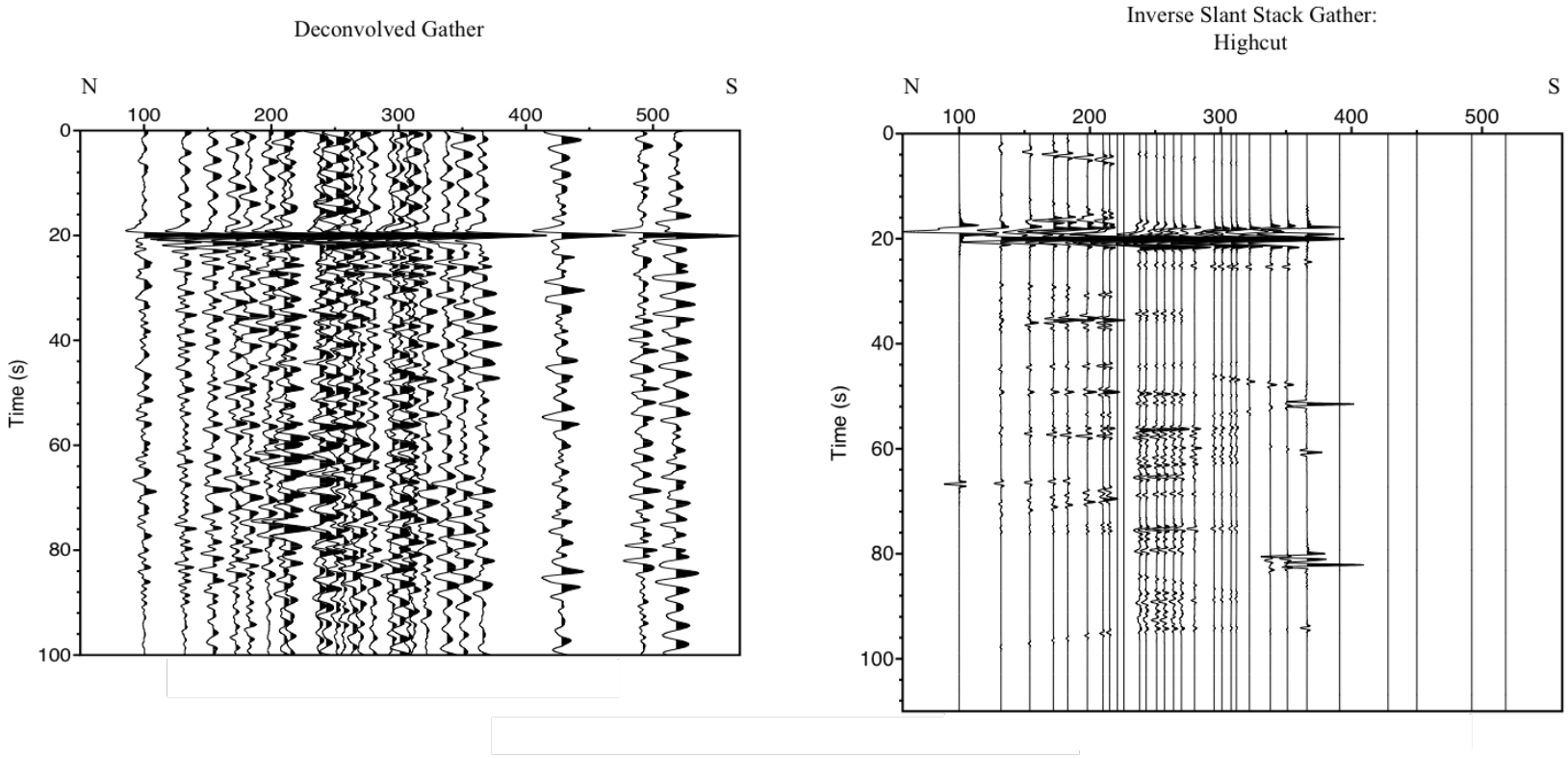

Figure 2.19 The image on the left is the original deconvolution image of the 7/7/13 m7.3 Line E. While some coherent events are visible in the deconvolved profile (alpha=2) of the E line, the process of slant stacking, coherency filtering, and inverse slant stacking drastically removes background noise.

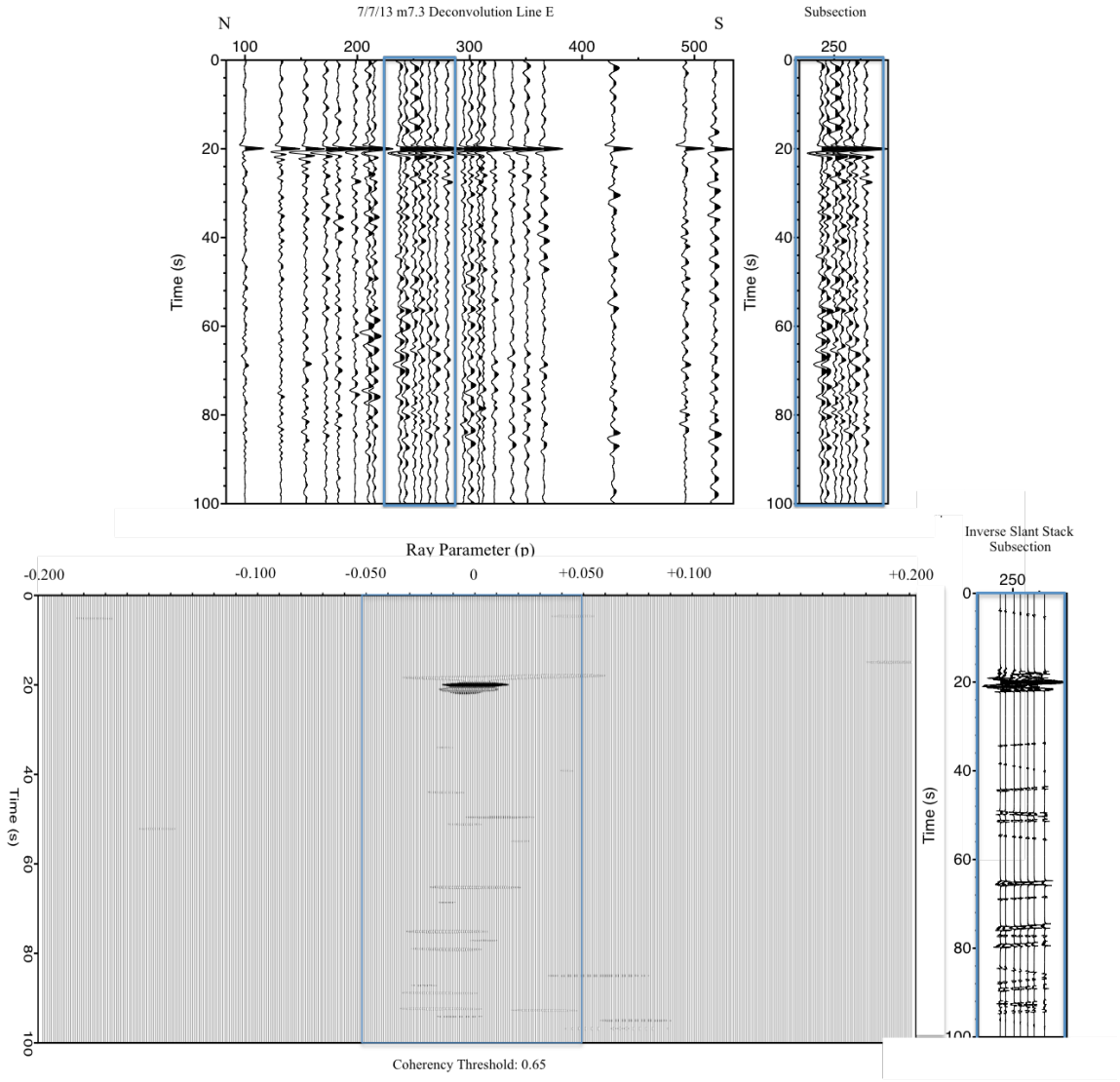

Figure 2.20 The image summarizes the processing steps. Increasing the threshold of the slant stack to 0.65 eliminates spatial alias effects and other incoherent noise. Most of the remaining coherent energy is concentrated at small p (i.e. small dips).

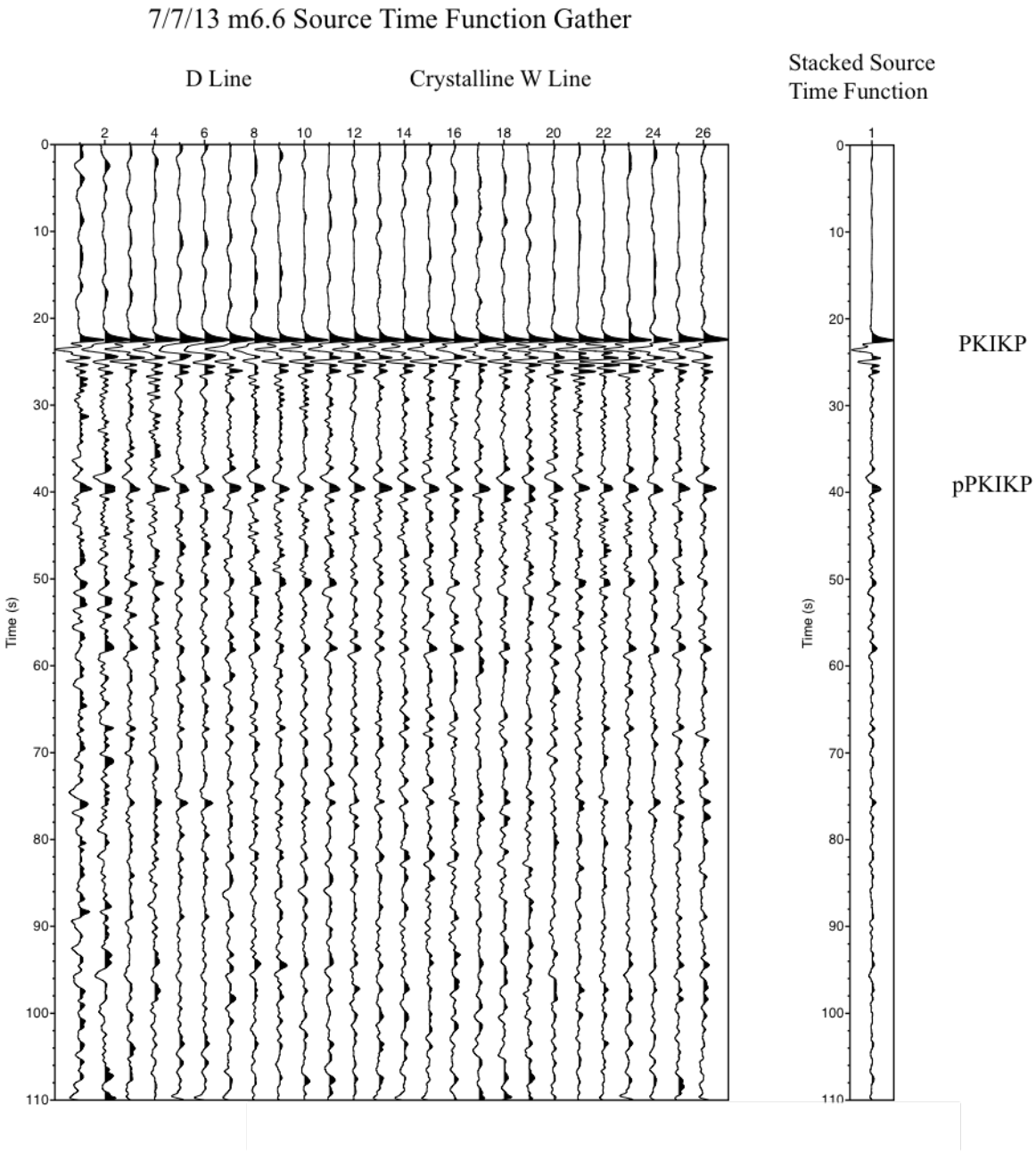

Figure 3.1 The source time function gather of the D line and crystalline W line for the shallow (62.0 km) magnitude 6.6 event on 7/7/13, illustrates the depth phase pPKIKP. Notice that, due to its similarity in ray parameter to the direct arrival, pPKIKP interferes constructively in the stacking of traces to generate the single trace source time function

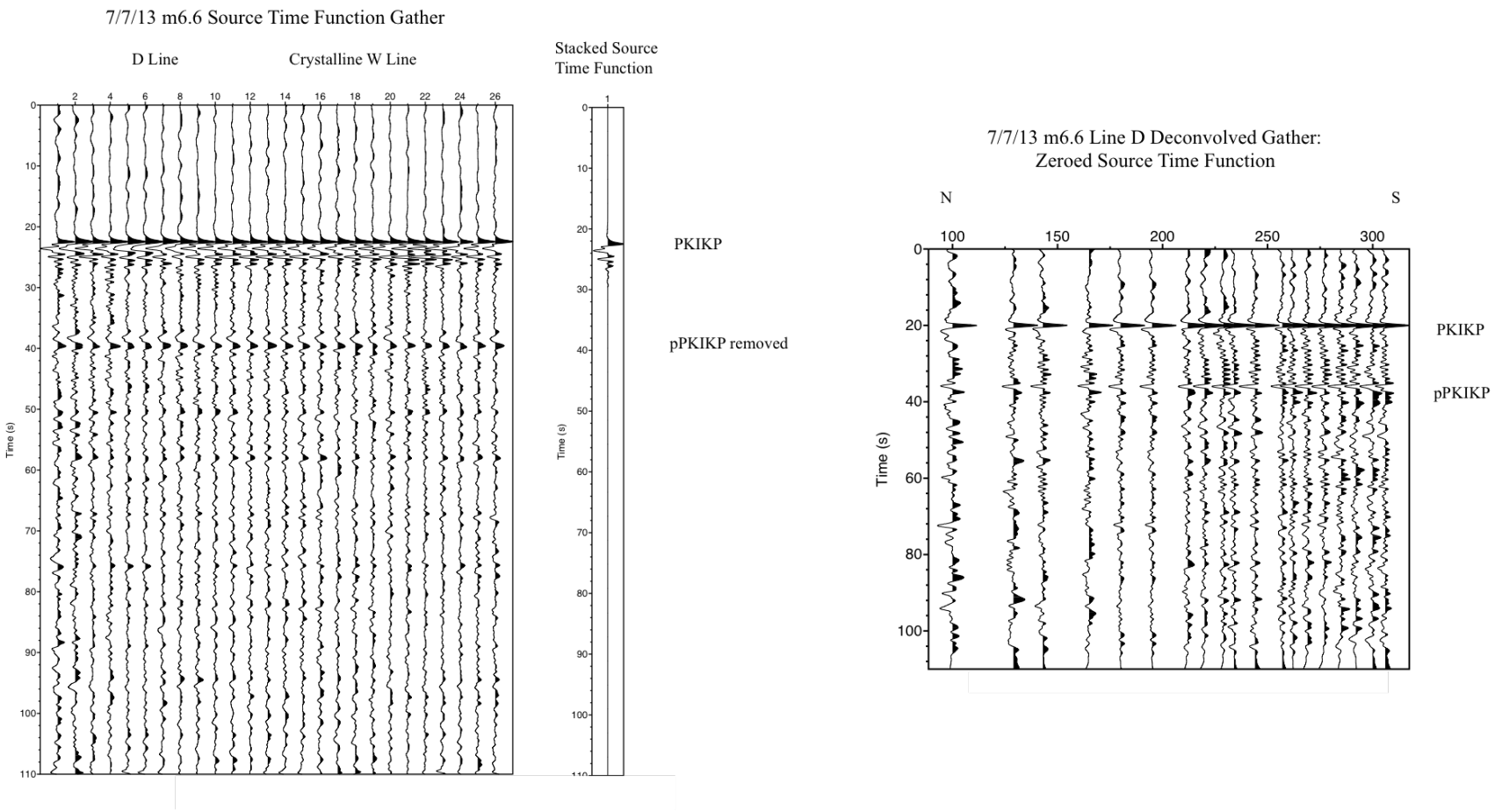

Figure 3.2 The depth phase pPKIKP is apparent on the deconvolved gather (right) of the shallow (62.0 km) 7/7/13 m6.6 at its expected arrival time from IASP-91 travel time estimates. The source-time function estimate, generated from all crystalline D and W stations, has been zeroed, removing the underside reflection pPKIKP from the stacked source-time function.

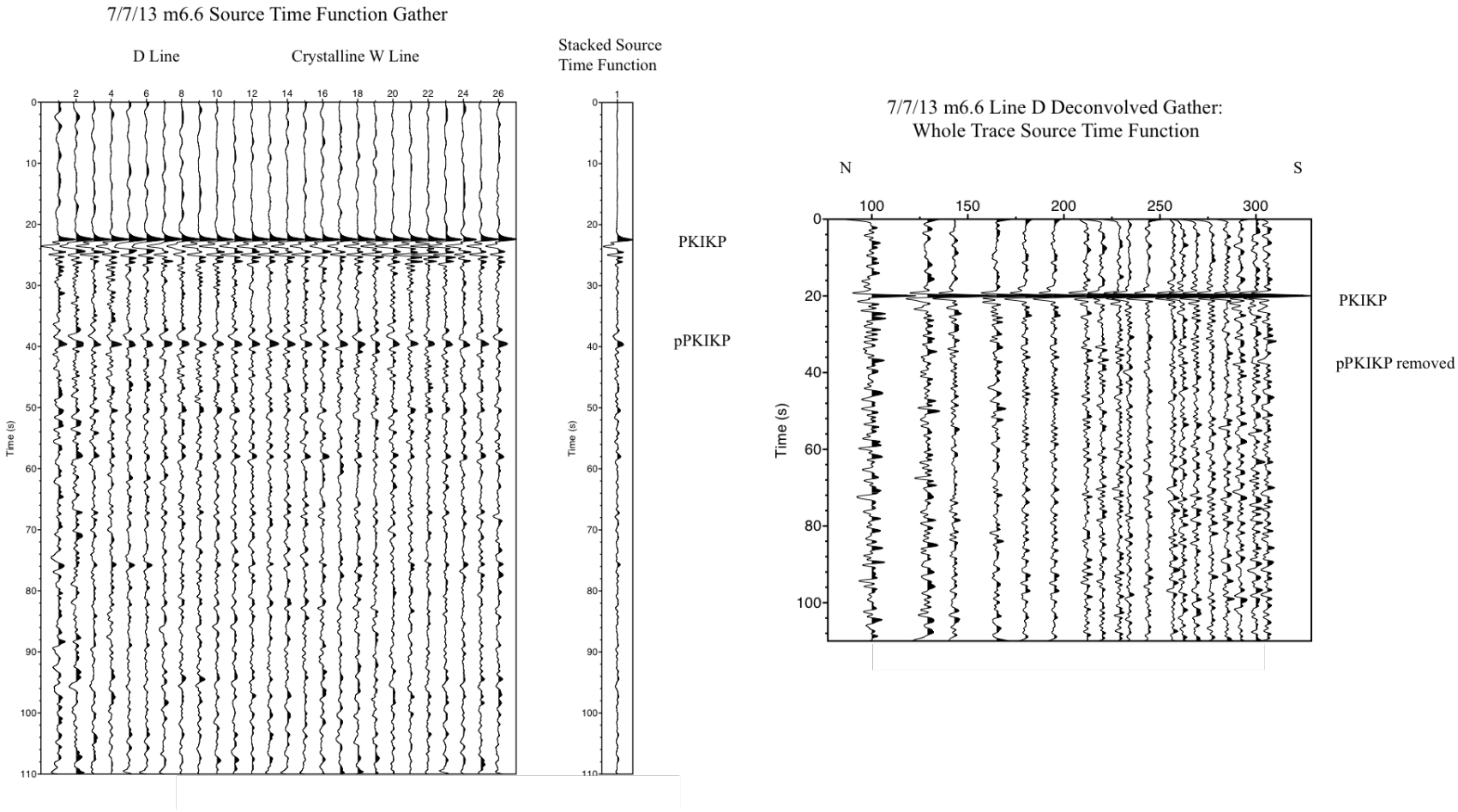

Figure 3.3 The pPKIKP depth phase has been effectively removed through deconvolution (image on the right) by including the underside reflection in the source time function estimate (left).

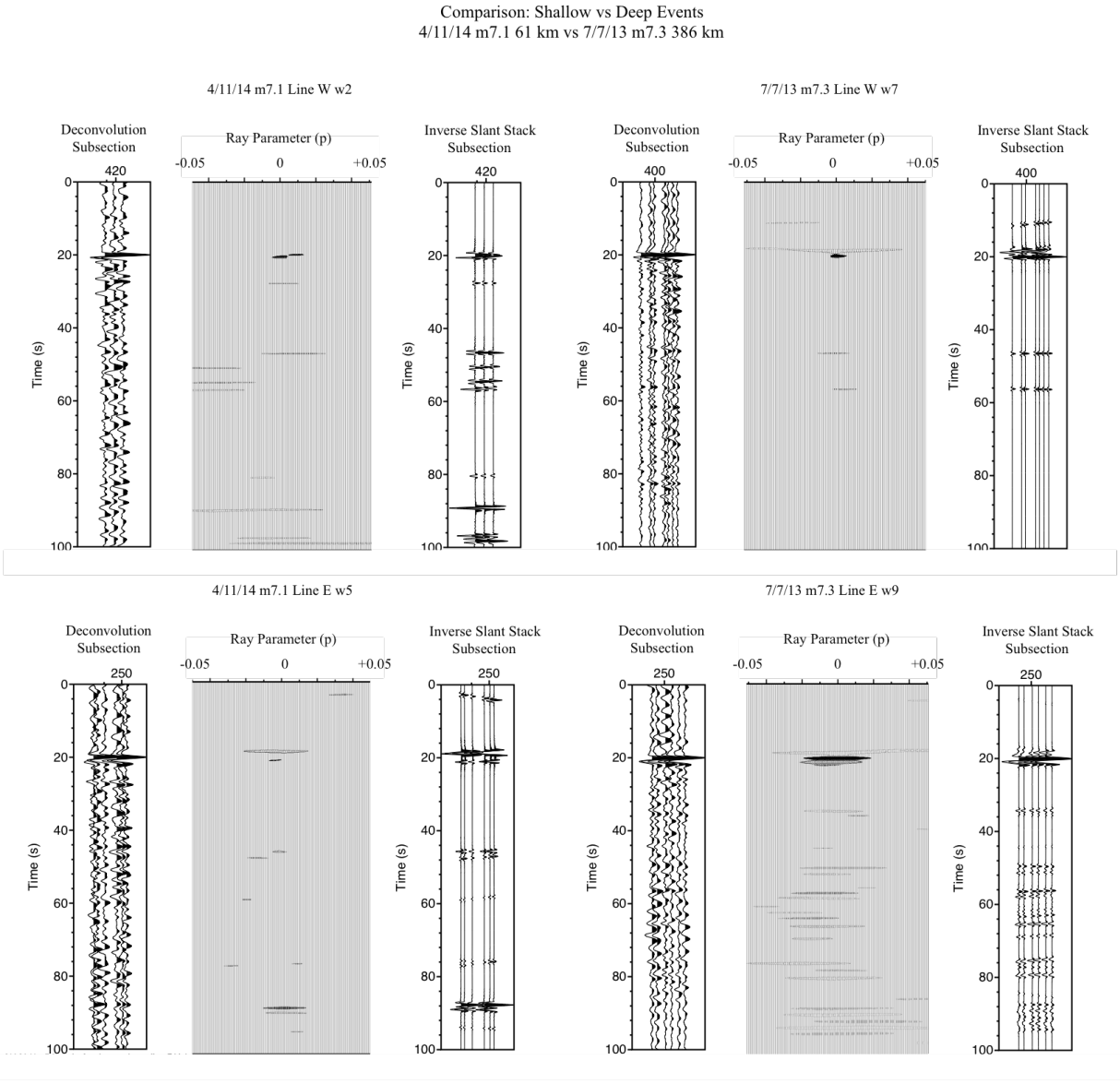

Figure 3.4 The shallow epicentral depth (61 km) of the 4/11/14 m7.1 event included the underside reflection pPKIKP in the source time function estimate and subsequent removal through deconvolution. The consistent reflection at ~45 seconds on the deconvolved gather along the W line of the Coastal Plain for the shallow 4/11/14 event is comparable to that of the 7/7/13 m7.3 event that has an epicentral depth of 386 km, thus proving the ability to remove

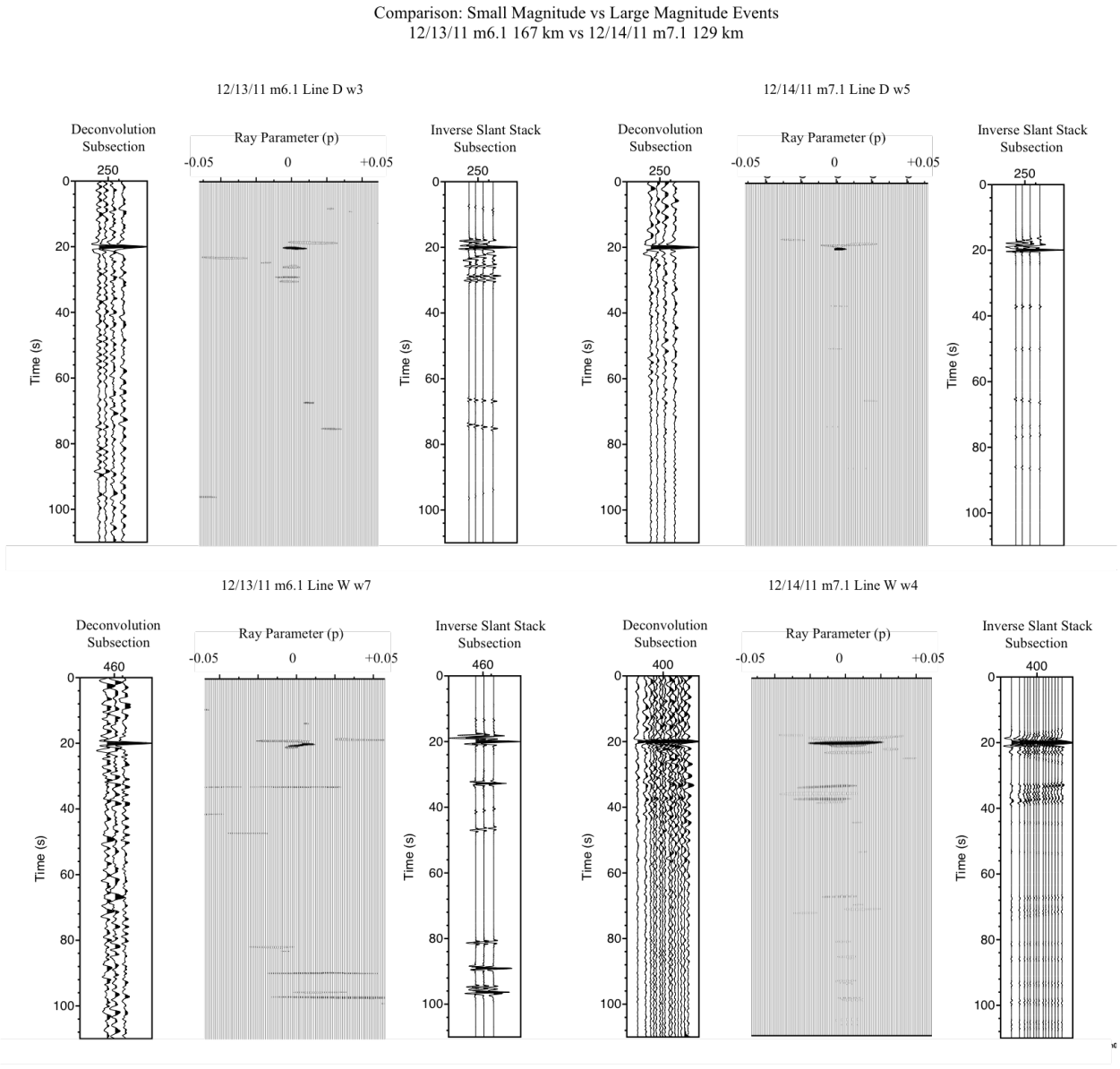

Figure 3.5 The shallow epicentral depth (61 km) small magnitude event 12/13/11 m6.1 shows consistency of reflections with the larger magnitude 12/14/11 m7.1 event. Note that there is less smearing when more stations are included in the slant stack (12/14/11 m7.1 Line W w6 vs

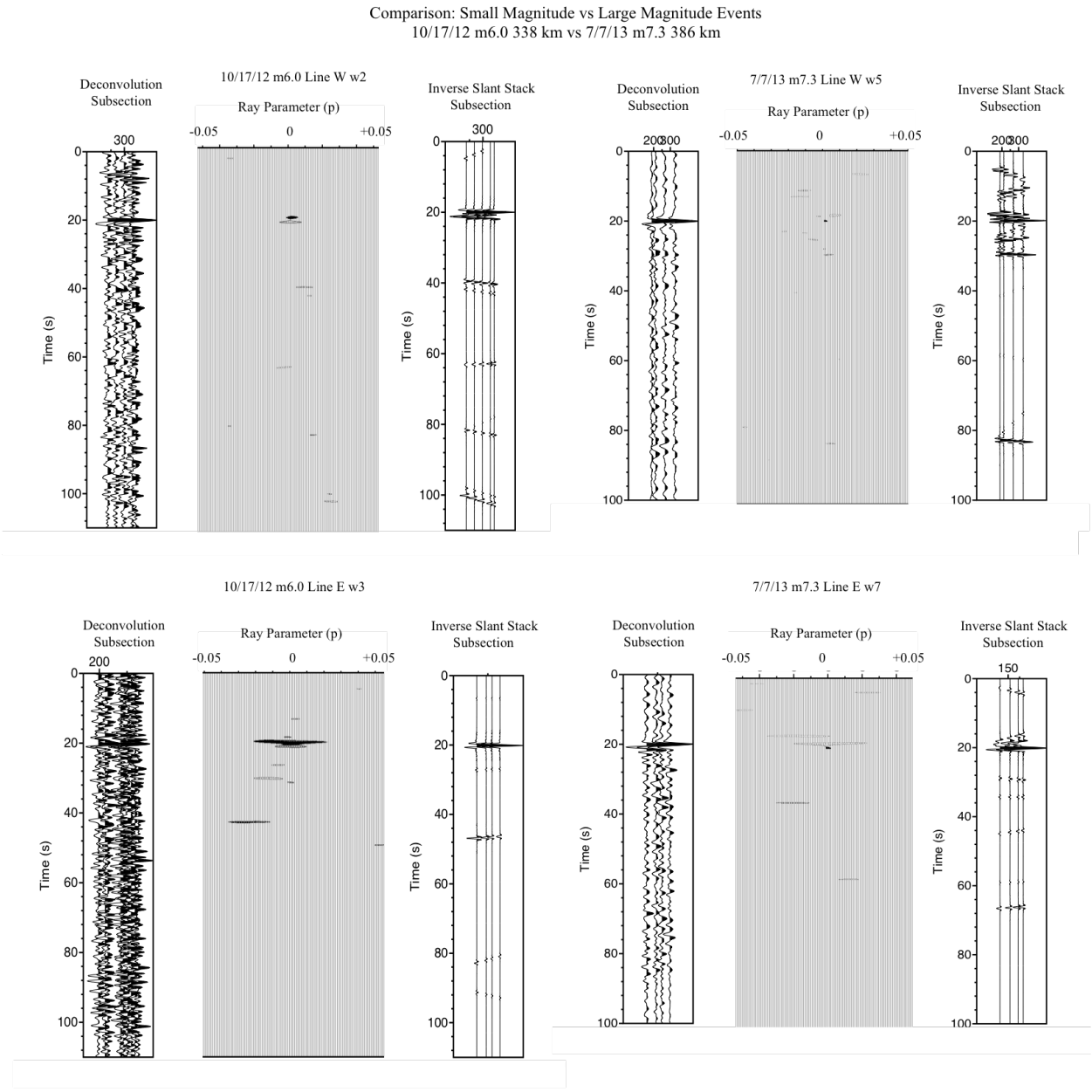

Figure 3.6 The small magnitude event 10/17/12 has lower initial signal levels than the high magnitude 7/7/13 m7.3 event, but there are still consistent reflections at ~80 seconds in the Inner Piedmont of the W line and ~45 seconds in the Coastal Plain of the E line.

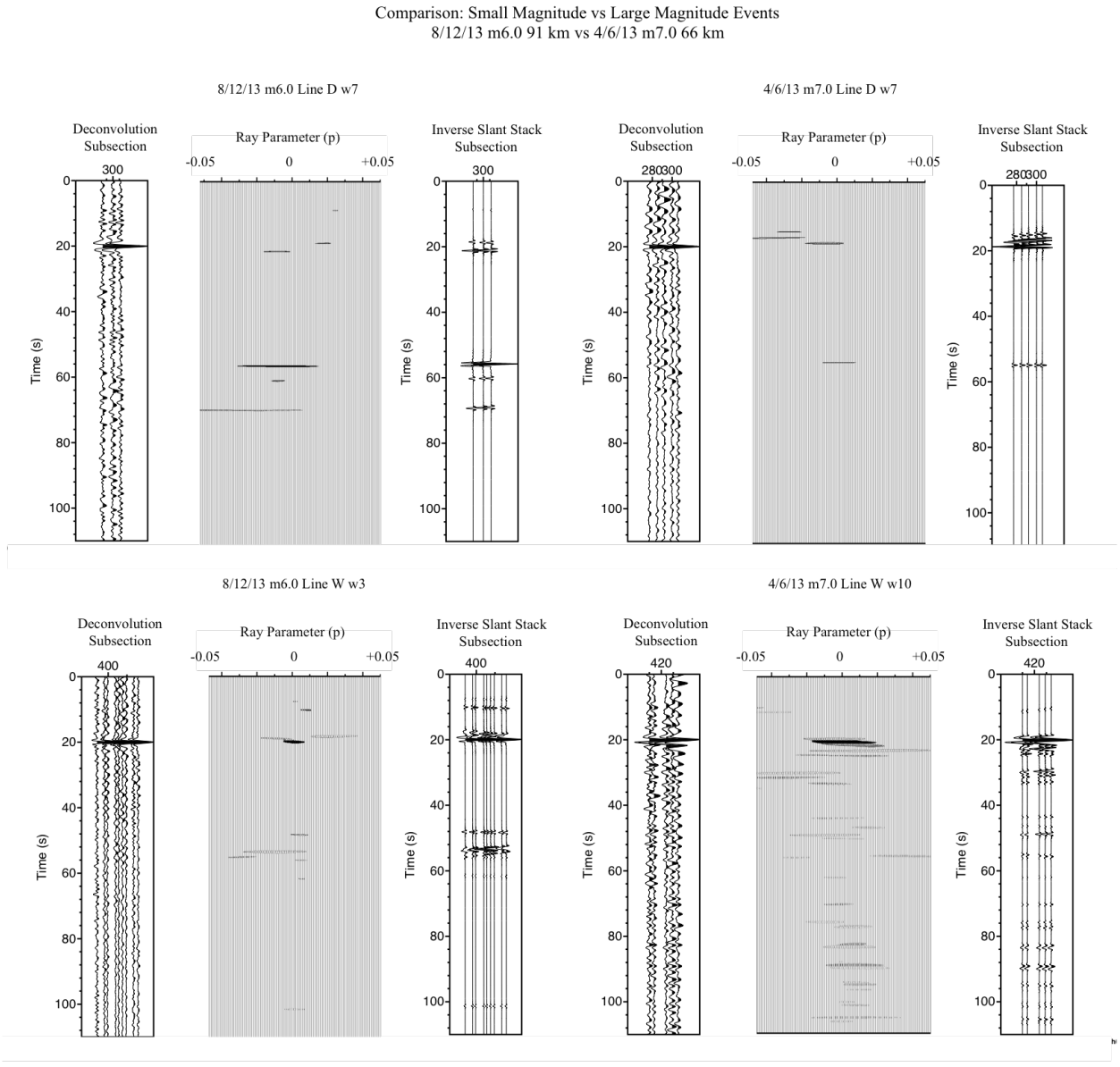

Figure 3.7 The small magnitude event 18/12/13 m6.0, which lies in the distance range with diverging PKIKP/PKiKP (140-145 degrees) shows consistency of reflections with the larger magnitude 4/6/13 m7.0 event. The top lines shows a consistent reflection at ~ 55 seconds in the Carolina Terrane of the D line, and the bottom line shows consistent reflections at ~50 and 100 seconds in the Coastal Plain of the W line. This specific example is especially important because it illustrates that our new processing method to combat the diverging PKIKP/PKiKP arrivals is reliable.

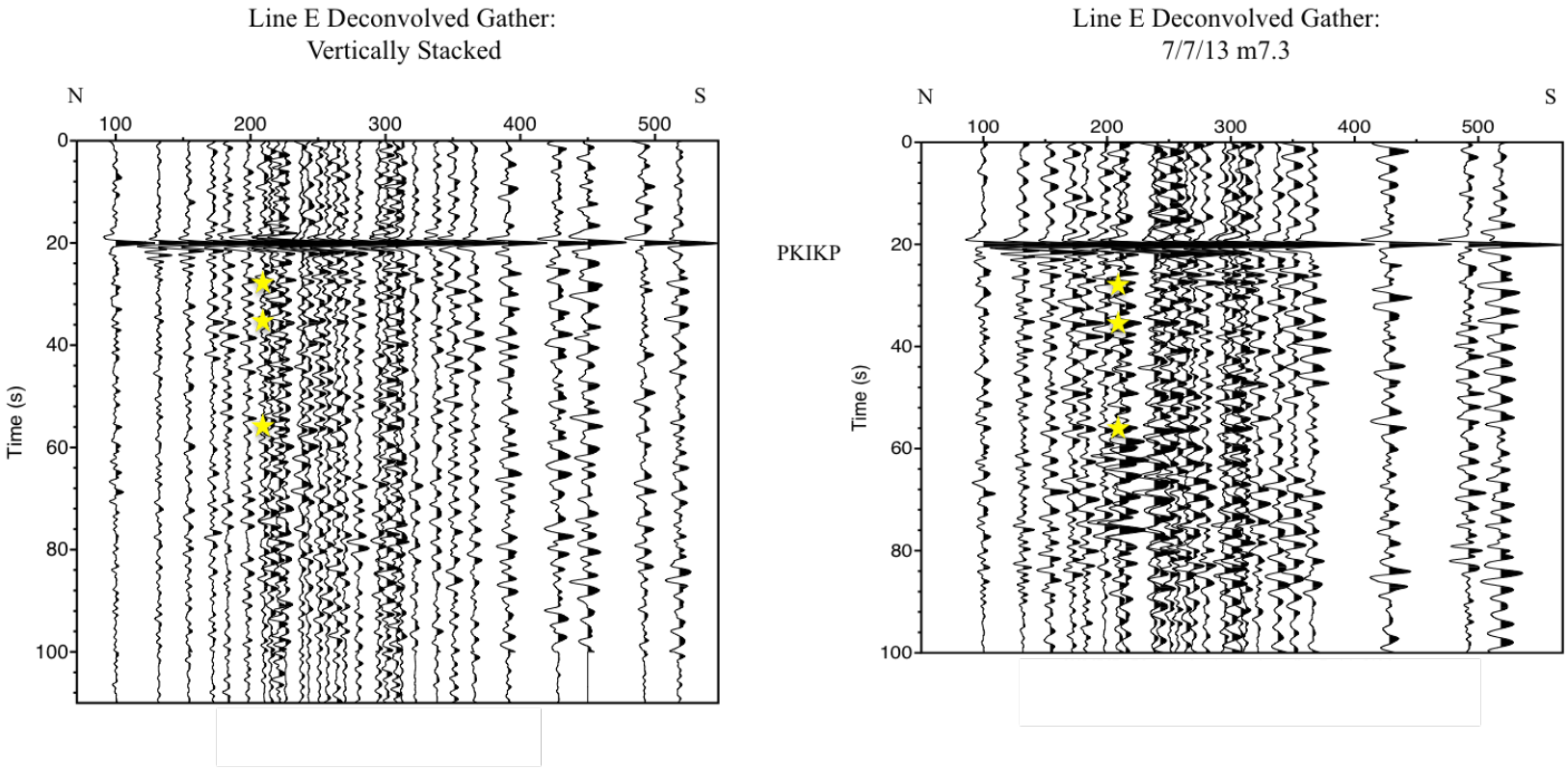

Figure 3.8 The image on the left is the result of vertically stacking deconvolved gathers for six events along the E line. The image on the right is the deconvolved gather from a single event, 7/7/13 m7.3. Note the consistent events at ~8, 35, and 55 seconds as indicated by the yellow stars. This comparison helps illustrate that our adaptation of the GloPSI method can yield usable signal levels from a single event.

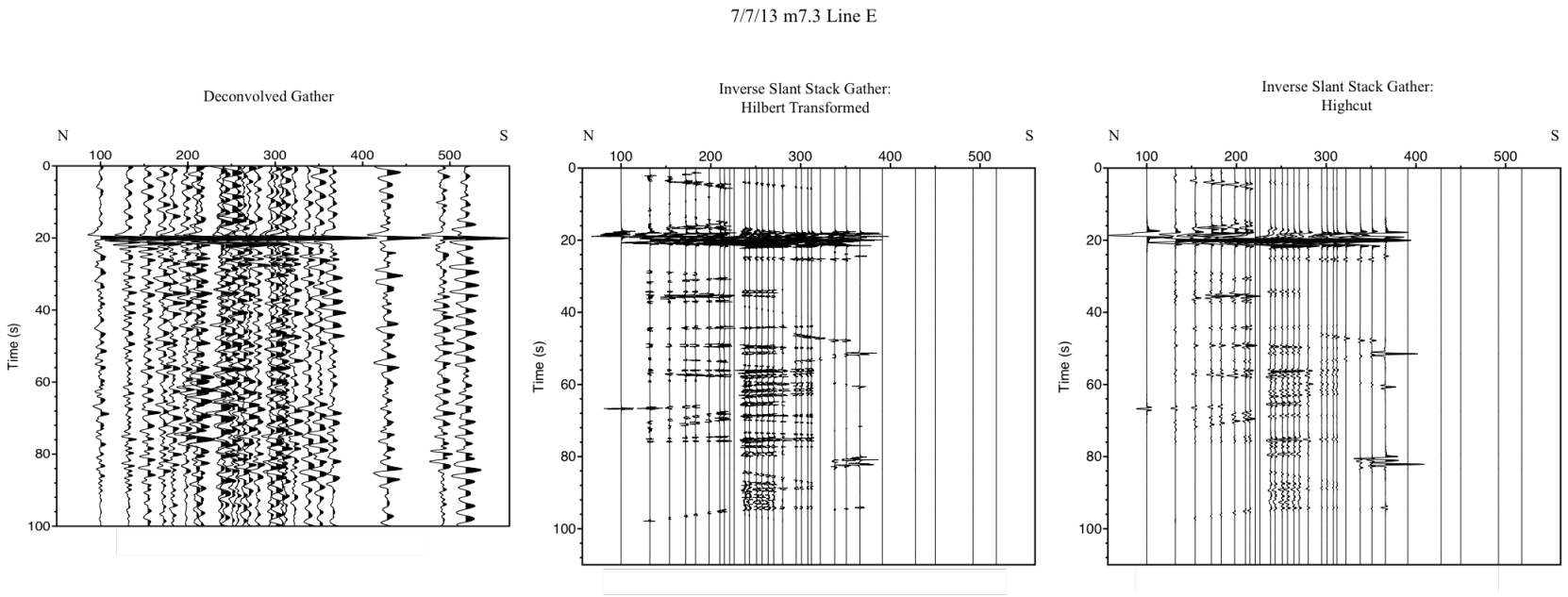

Figure 3.9 The deconvolved image on the left has some visible reflections, however, it is important to note that this is a large magnitude event with high initial signal levels. This is not always the case when working with earthquake sources. Despite the high signal levels, it is still difficult to interpret reflections. The process of slant stacking, coherency filtering, and inverse slant stacking back into the time domain is an effective way to unveil coherent reflections from single events. During the inverse slant stacking process, high frequencies are lost, so they must be reintroduced through the Hilbert transform. This transform overwhelms the image with high frequencies, so a highcut filter is applied as well.

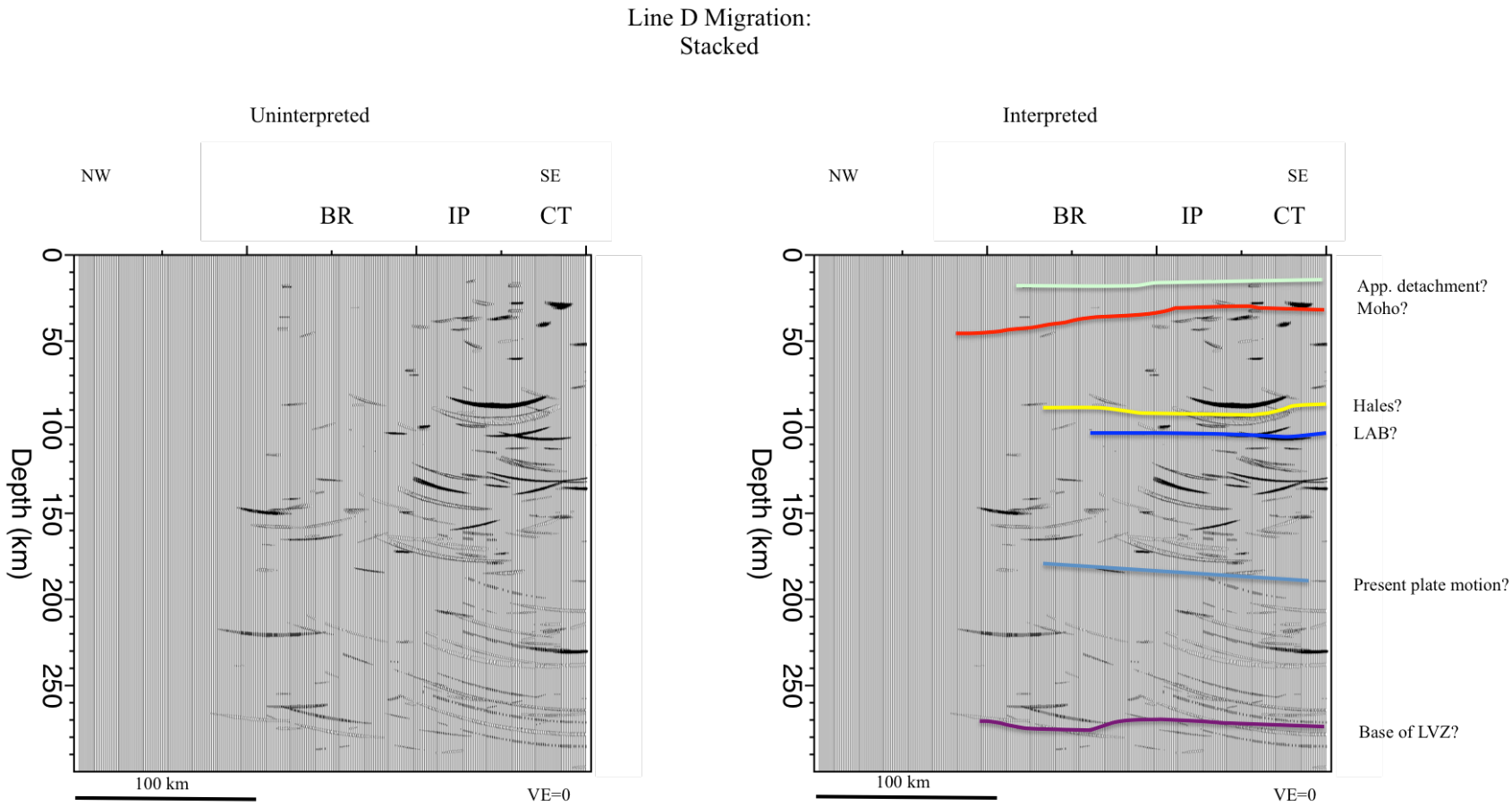

Figure 4.1 The images represent migration results along the NW-SE trending D Line, which spans the Valley & Ridge, Blue Ridge (BR), Inner Piedmont (IP), and Carolina Terrane (CT). See text for explanation on possible geologic source of reflectors. The events used for the stacked migration include: 7/7/13 m7.3, 4/11/14 m7.1, 7/7/13 m6.6, 4/17/12 m6.9, 12/14/11 m7.1, 4/6/13 m7.0, 10/17/12 m6.0, 12/13/11 m6.1, and 8/12/13 m6.0. More information regarding these events can be found in Appendix C.

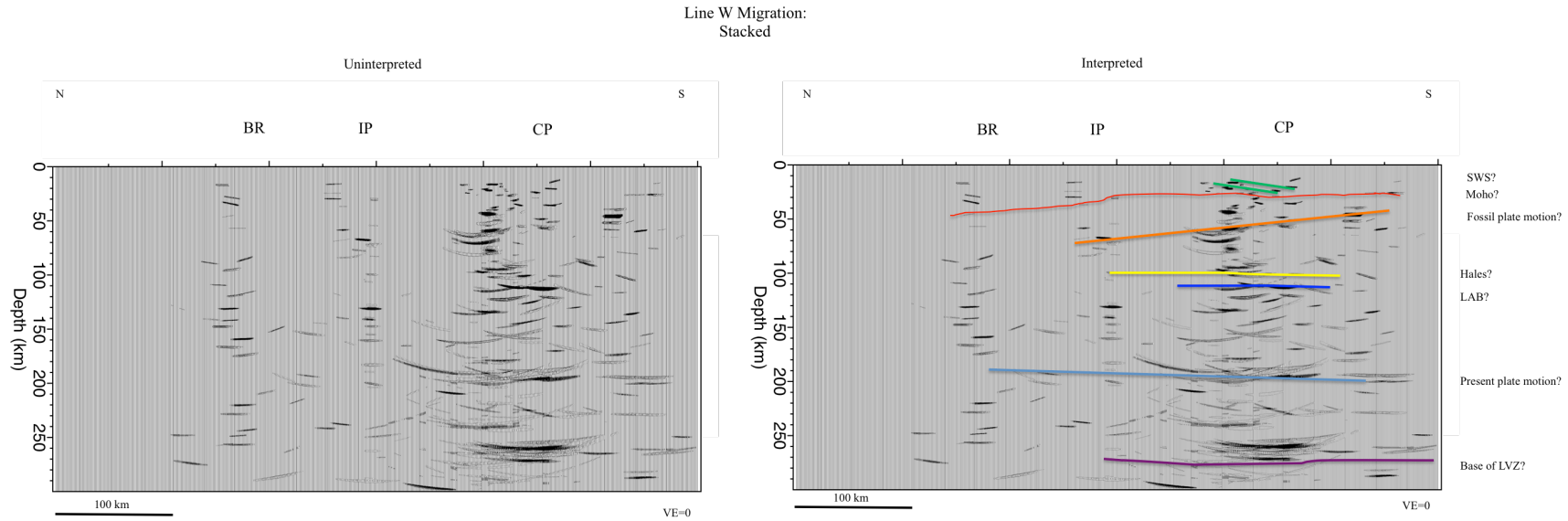

Figure 4.2 The images represent migration results along the N-S trending W Line, which covers the Blue Ridge, Inner Piedmont, and Coastal Plain provinces. See text for possible geologic source of reflectors. One challenge is that station spacing is fairly large at the north end of the array. The events used for the stacked migration include: 7/7/13 m7.3, 4/11/14 m7.1, 7/7/13 m6.6, 4/17/12 m6.9, 12/14/11 m7.1, 4/6/13 m7.0, 10/17/12 m6.0, 12/13/11 m6.1, and 8/12/13 m6.0. More information regarding these events can be found in Appendix C.

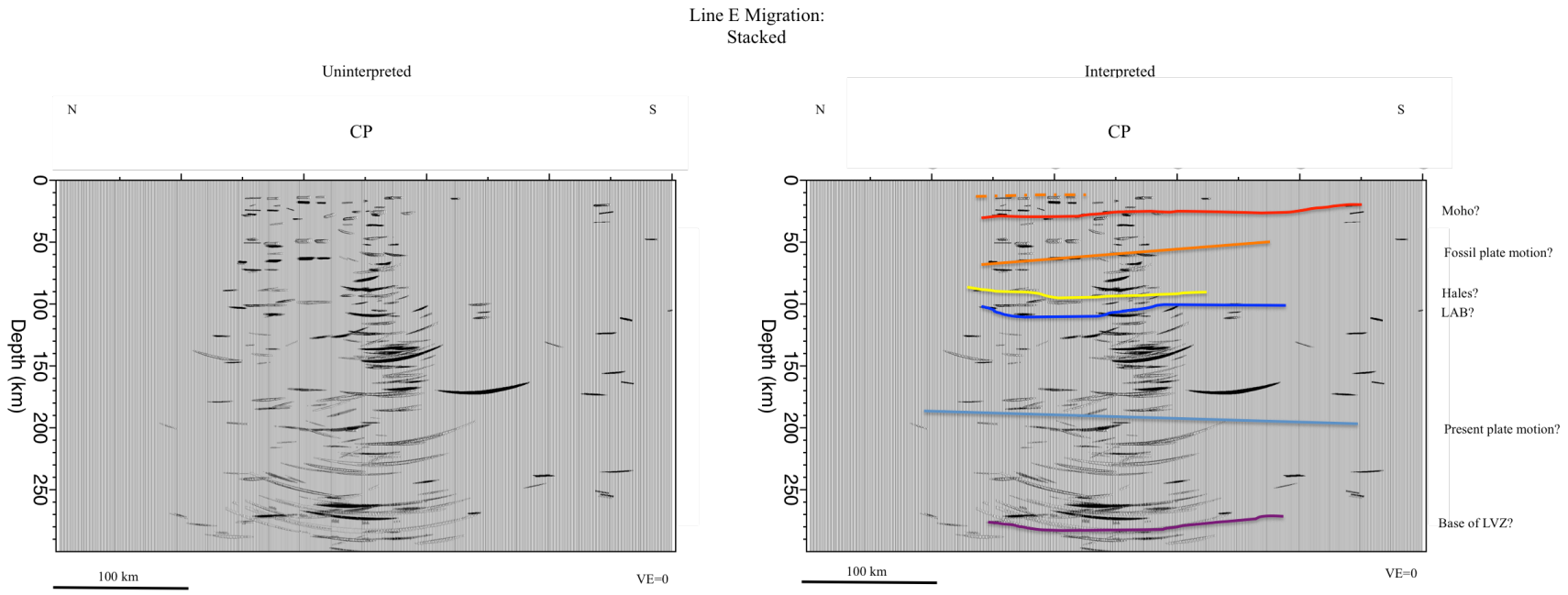

Figure 4.3 The image illustrated migrated results along the sediment rooted E line. See text for possible geologic source of reflectors. 7/7/13 m7.3, 4/11/14 m7.1, 7/7/13 m6.6, 4/6/13 m7.0, 10/17/12 m6.0, and 8/12/13 m6.0. More information regarding these events can be found in Appendix C.

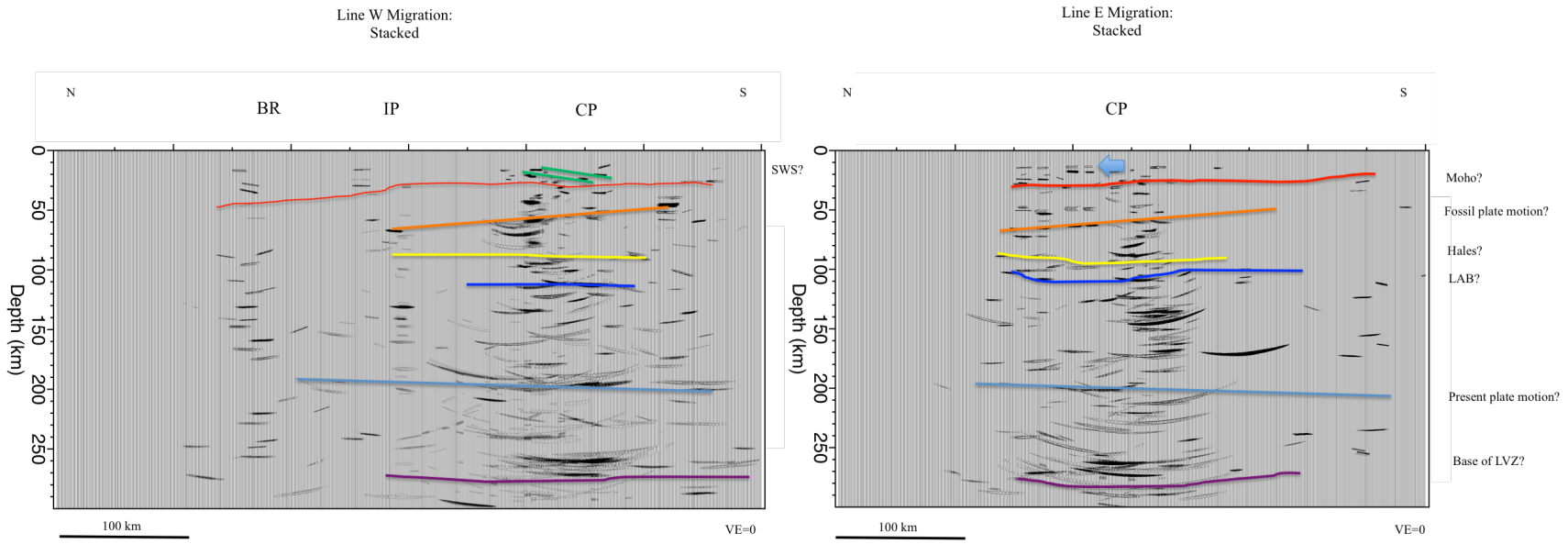

Figure 4.4 The Coastal Plain sediments on the W and E lines have similar reflections. Line E appears to have more flay lying reflections in the shallow lithosphere that are not present on the W line, as indicated by the blue arrow.

REFERENCES

Abt, D. L., Fischer, K. M., French, S. W., Ford, H. A., Yuan, H., & Romanowicz, B. (2010). North American lithospheric discontinuity structure imaged by Ps and Sp receiver functions. *Journal of Geophysical Research: Solid Earth*, *115*(B9).

Alberts, E. C. (2017). *Global Phase Seismic Interferometry (GloPSI) and Broadband Reflection Techniques: An Investigation of the Southeastern Suture of the Appalachian Margin Experiment* (master's thesis). University of Georgia, Athens, Georgia.

Anderson, D. L. (1979). The deep structure of continents. *Journal of Geophysical Research: Solid Earth*, *84*(B13), 7555-7560.

Biryol, C. B., Wagner, L. S., Fischer, K. M., & Hawman, R. B. (2016). Relationship between observed upper mantle structures and recent tectonic activity across the Southeastern United States. *Journal of Geophysical Research: Solid Earth*, *121*(5), 3393-3414.

Bostock, M. G. (1998). Mantle stratigraphy and evolution of the Slave province. *Journal of Geophysical Research: Solid Earth*, *103*(B9), 21183-21200.

Burdick, L. J., & Langston, C. A. (1977). Modeling crustal structure through the use of converted phases in teleseismic body-wave forms. *Bulletin of the Seismological Society of America*, *67*(3), 677-691.

Claerbout, J. F. (1968). Synthesis of a layered medium from its acoustic transmission response. *Geophysics*, *33*(2), 264-269.

Cook, F. A., Albaugh, D. S., Brown, L. D., Kaufman, S., Oliver, J. E., & Hatcher, R. D. (1979). Thin-skinned tectonics in the crystalline southern Appalachians; COCORP seismic-reflection profiling of the Blue Ridge and Piedmont. *Geology*, *7*(12), 563-567.

Cook, F. A., & Vasudevan, K. (2006). Reprocessing and enhanced interpretation of the initial COCORP Southern Appalachians traverse. *Tectonophysics*, *420*(1), 161-174.

Coruh, C., Costain, J. K., Hatcher, R. D., Pratt, T. L., Williams, R. T., & Phinney, R. A. (1987). Results from regional vibroseis profiling: Appalachian ultra-deep core hole site study. *Geophysical Journal International*, *89*(1), 147-156.

Dallmeyer, R. D., Wright, J. E., Secor, D. T., & Snoke, A. W. (1986). Character of the Alleghanian orogeny in the southern Appalachians: Part II. Geochronological constraints on the tectonothermal evolution of the eastern Piedmont in South Carolina. *Geological Society of America Bulletin*, *97*(11), 1329-1344.

Deschamps, F., Lebedev, S., Meier, T., & Trampert, J. (2008). Stratified seismic anisotropy reveals past and present deformation beneath the East-central United States. *Earth and Planetary Science Letters*, *274*(3), 489-498.

Dobrin, M. B.; Savit, C. H. 1988: Introduction to geophysical prospecting. 4th ed. New York, McGraw Hill.

Dueker, K. G., & Sheehan, A. F. (1997). Mantle discontinuity structure from midpoint stacks of converted P to S waves across the Yellowstone hotspot track. *Journal of Geophysical Research: Solid Earth*, *102*(B4), 8313-8327.

Eaton, D. W., Darbyshire, F., Evans, R. L., Grütter, H., Jones, A. G., & Yuan, X. (2009). The elusive lithosphere–asthenosphere boundary (LAB) beneath cratons. *Lithos*, *109*(1), 1-22.

Fischer, K. M. (2002). Waning buoyancy in the crustal roots of old mountains. *Nature*, *417*(6892), 933-936.

Fischer, K. M., Ford, H. A., Abt, D. L., & Rychert, C. A. (2010). The lithosphere-asthenosphere boundary. *Annual Review of Earth and Planetary Sciences*, *38*, 551-575.

Ford, H. A., Fischer, K. M., Abt, D. L., Rychert, C. A., & Elkins-Tanton, L. T. (2010). The lithosphere–asthenosphere boundary and cratonic lithospheric layering beneath Australia from Sp wave imaging. *Earth and Planetary Science Letters*, *300*(3), 299-310.

French, S. W., Fischer, K. M., Syracuse, E. M., & Wysession, M. E. (2009). Crustal structure beneath the Florida-to-Edmonton broadband seismometer array. *Geophysical Research Letters*, *36*(8).

Fuchs, K. (1969). On the properties of deep crustal reflectors. *Z. Geophys*, *35*(2).

Gaherty, J. B. (2004). A surface wave analysis of seismic anisotropy beneath eastern North America. *Geophysical Journal International*, *158*(3), 1053-1066.

Goldstein, P., & Snoke, A. (2005). SAC availability for the IRIS community. *Incorporated Research Institutions for Seismology Newsletter*, *7*(UCRL-JRNL-211140).

Hales, A. L. (1969). A seismic discontinuity in the lithosphere. *Earth and Planetary Science Letters*, *7*(1), 44-46.

Hames, W. E., Renne, P. R., & Ruppel, C. (2000). New evidence for geologically instantaneous emplacement of earliest Jurassic Central Atlantic magmatic province basalts on the North American margin. *Geology*, *28*(9), 859-862.

Hatcher, R.D. (1972). Developmental model for the southern Appalachians. *Geological Society of America Bulletin*, *83*(9), 2735-2760.

Hatcher, R. D. (1978). Tectonics of the western Piedmont and Blue Ridge, Southern Appalachians; review and speculation. *American Journal of Science*, *278*(3), 276-304.

Hatcher Jr, R. D., (1989). Tectonic synthesis of the U.S. Appalachians, in *The Geology of North America*, vol. F-2, *The Appalachian-Ouachita Orogen in the United States*, edited by R. D. Hatcher, Jr., W. A. Thomas, and G. W. Viele, pp. 511-535, Geol. Soc. Of Am., Boulder, Colo.

Hatcher, R. D. (2002). Alleghanian (Appalachian) orogeny, a product of zipper tectonics: Rotational transpressive continent-continent collision and closing of ancient oceans along irregular margins. *Special Paper-Geological Society of America*, (364), 199-208.

Hatcher, R. D. (2010). The Appalachian orogen: A brief summary. *Geological Society of America Memoirs*, *206*, 1-19.

Hatcher Jr, R. D., Costain, J. K., Coruh, C., Phinney, R. A., & Williams, R. T. (1987). Tectonic implications of new Appalachian Ultradeep Core Hole (ADCOH) seismic reflection data from the crystalline southern Appalachians. *Geophysical Journal International*, *89*(1), 157-162.

Hatcher, R. D., Bream, B. R., & Merschat, A. J. (2007). Tectonic map of the southern and central Appalachians: A tale of three orogens and a complete Wilson cycle. *Geological Society of America Memoirs*, *200*, 595-632.

Hawman, R. B. (2008). Crustal thickness variations across the Blue Ridge Mountains, southern Appalachians: An alternative procedure for migrating wide-angle reflection data. *Bulletin of the Seismological Society of America*, *98*(1), 469-475.

Hawman, R. B., Khalifa, M. O., & Baker, M. S. (2012). Isostatic compensation for a portion of the Southern Appalachians: Evidence from a reconnaissance study using wide-angle, three-component seismic soundings. *Geological Society of America Bulletin*, *124*(3-4), 291-317.

Hedlin, M. A., Shearer, P. M., & Earle, P. S. (1997). Seismic evidence for small-scale heterogeneity throughout the Earth's mantle. *Nature*, *387*(6629), 145-150.

Heffner, D. M., Knapp, J. H., Akintunde, O. M., & Knapp, C. C. (2012). Preserved extent of Jurassic flood basalt in the South Georgia Rift: A new interpretation of the J horizon. *Geology*, *40*(2), 167-170.

Hopper, E., Fischer, K. M., Rondenay, S., Hawman, R. B., & Wagner, L. S. (2016). Imaging crustal structure beneath the southern Appalachians with wavefield migration. *Geophysical Research Letters*, *43*(23).

Hopper, E., Fischer, K. M., Wagner, L. S., & Hawman, R. B. (2017). Reconstructing the end of the Appalachian orogeny. *Geology*, *45*(1), 15-18.

Hubbard, S. S., Çoruh, C., & Costain, J. K. (1991). Paleozoic and Grenvillian structures in the southern Appalachians: Extended interpretation of seismic reflection data. *Tectonics*, *10*(1), 141-170.

Jarchow, C. M., & Thompson, G. A. (1989). The nature of the Mohorovicic discontinuity. *Annual Review of Earth and Planetary Sciences*, *17*(1), 475-506.

Karner, G. D., & Watts, A. B. (1983). Gravity anomalies and flexure of the lithosphere at mountain ranges. *Journal of Geophysical Research: Solid Earth*, *88*(B12), 10449-10477.

Kind, R., Yuan, X., & Kumar, P. (2012). Seismic receiver functions and the lithosphere–asthenosphere boundary. *Tectonophysics*, *536*, 25-43.

Langston, C. A. (1977). Corvallis, Oregon, crustal and upper mantle receiver structure from teleseismic P and S waves. *Bulletin of the Seismological Society of America*, *67*(3), 713-724.

Langston, C. A. (1979). Structure under Mount Rainier, Washington, inferred from teleseismic body waves. *Journal of Geophysical Research: Solid Earth*, *84*(B9), 4749-4762.

Langston, C. A., & Ammon, C. J. (1991). Scattering of teleseismic body waves along the Hayward-Calaveras fault system. *Bulletin of the Seismological Society of America*, *81*(2), 576-591.

Levin, V., & Park, J. (2000). Shear zones in the Proterozoic lithosphere of the Arabian Shield and the nature of the Hales discontinuity. *Tectonophysics*, *323*(3), 131-148.

Li, A., Fischer, K. M., van der Lee, S., & Wysession, M. E. (2002). Crust and upper mantle discontinuity structure beneath eastern North America. *Journal of Geophysical Research: Solid Earth*, *107*(B5).

Ma, X., Sun, X., Wiens, D. A., Wen, L., Nyblade, A., Anandakrishnan, S., ... & Wilson, T. (2016). Strong seismic scatterers near the core–mantle boundary north of the Pacific Anomaly. *Physics of the Earth and Planetary Interiors*, *253*, 21-30.

Manspeizer, W. (1988). Triassic–Jurassic rifting and opening of the Atlantic: an overview. In *Developments in Geotectonics,* (Vol. 22, pp. 41-79). Elsevier.

Marfurt, K. J., Kirlin, R. L., Farmer, S. L., & Bahorich, M. S. (1998). 3-D seismic attributes using a semblance-based coherency algorithm. *Geophysics*, *63*(4), 1150-1165.

McBride, J. H. (1991). Constraints on the structure and tectonic development of the early Mesozoic South Georgia rift, southeastern United States; seismic reflection data processing and interpretation. *Tectonics*, *10*(5), 1065-1083.

McBride, J. H., Nelson, K. D., & Brown, L. D. (1987). Early Mesozoic basin structure and tectonics of the southeastern United States as revealed from COCORP reflection data and the relation to Atlantic rifting. In Beaumont, C and Tankard, A. J., ed. *Sedimentary Basins and Basin-forming mechanisms*, Canadian Society of Petroleum Geologists Memoir 12, pp. 173-184.

McBride, J. H., & Nelson, K. D. (1988). Integration of COCORP deep reflection and magnetic anomaly analysis in the southeastern United States: Implications for origin of the Brunswick and East Coast magnetic anomalies. *Geological Society of America Bulletin*, *100*(3), 436-445.

McBride, J. H., Nelson, K. D., & Brown, L. D. (1989). Evidence and implications of an extensive early Mesozoic rift basin and basalt/diabase sequence beneath the southeast Coastal Plain. *Geological Society of America Bulletin*, *101*(4), 512-520.

McBride, J. H., Hatcher, R. D., Stephenson, W. J., & Hooper, R. J. (2005). Integrating seismic reflection and geological data and interpretations across an internal basement massif: The southern Appalachian Pine Mountain window, USA. *Geological Society of America Bulletin*, *117*(5-6), 669-686.

Meissner, R. (1967). Exploring deep interfaces by seismic wide angle measurements. *Geophysical Prospecting*, 15(4), 598-617.

Meissner, R. (1973). The 'Moho'as a transition zone. *Surveys in Geophysics*, *1*(2), 195-216.

Miller, C. F., Hatcher, R. D., Ayers, J. C., Coath, C. D., & Harrison, T. M. (2000). Age and zircon inheritance of eastern Blue Ridge plutons, southwestern North Carolina and northeastern Georgia, with implications for magma history and evolution of the southern Appalachian orogen. *American Journal of Science*, *300*(2), 142-172.

Mueller, P. A., Heatherington, A. L., Foster, D. A., Thomas, W. A., & Wooden, J. L. (2014). The Suwannee suture: Significance for Gondwana-Laurentia terrane transfer and formation of Pangaea. *Gondwana Research*, *26*(1), 365-373.

Neidell, N. S., & Taner, M. T. (1971). Semblance and other coherency measures for multichannel data. *Geophysics*, *36*(3), 482-497.

Nelson, K. D., McBride, J. H., Arnow, J. A., Wille, D. M., Brown, L. D., Oliver, J. E., & Kaufman, S. (1987). Results of recent COCORP profiling in the southeastern United States. *Geophysical Journal International*, *89*(1), 141-146.

Odom, A. L., Hatcher Jr, R. D., & Hooper, R. J. (1982). A pre-metamorphic tectonic boundary between contrasting Appalachian basements, southern Georgia Piedmont. In *Geological Society of America Abstracts with Programs* (Vol. 14, p. 579).

Parker, E. H., Hawman, R. B., Fischer, K. M., & Wagner, L. S. (2013). Crustal evolution across the southern Appalachians: Initial results from the SESAME broadband array. *Geophysical Research Letters*, *40*(15), 3853-3857.

Parker, E. H., Hawman, R. B., Fischer, K. M., & Wagner, L. S. (2015). Constraining lithologic variability along the Alleghanian detachment in the southern Appalachians using passive-source seismology. *Geology*, *43*(5), 431-434.

Parker Jr, E. H., Hawman, R. B., Fischer, K. M., & Wagner, L. S. (2016). Estimating crustal thickness using SsPmp in regions covered by low‐velocity sediments: Imaging the Moho beneath the Southeastern Suture of the Appalachian Margin Experiment (SESAME) array, SE Atlantic Coastal Plain. *Geophysical Research Letters*, *43*(18), 9627-9635.

Petersen, T. A., Brown, L. D., Cook, F. A., Kaufman, S., & Oliver, J. E. (1984). Structure of the Riddleville basin from COCORP seismic data and implications for reactivation tectonics. *The Journal of Geology*, *92*(3), 261-271.

Phinney, R. A., Chowdhury, K. R., & Frazer, L. N. (1981). Transformation and analysis of record sections. *Journal of Geophysical Research: Solid Earth*, *86*(B1), 359-377.

Robinson, E. A., & Treitel, S. (2000). *Geophysical signal analysis*. Society of Exploration Geophysicists.

Ruigrok, E., & Wapenaar, K. (2012). Global‐phase seismic interferometry unveils P‐wave reflectivity below the Himalayas and Tibet. *Geophysical Research Letters*, *39*(11).

Russell, G. S. (1978). *U-Pb, Rb-Sr, and K-Ar Isotopic Studies: Bearing on the Tectonic Development of the Southernmost Appalachian Orogen, Alabama* (Doctoral dissertation, Florida State University).

Rychert, C. A., Fischer, K. M., & Rondenay, S. (2005). A sharp lithosphere–asthenosphere boundary imaged beneath eastern North America. *Nature*, *436*(7050), 542-545.

Rychert, C. A., Rondenay, S., & Fischer, K. M. (2007). P-to-S and S-to-P imaging of a sharp lithosphere-asthenosphere boundary beneath eastern North America. *Journal of Geophysical Research: Solid Earth*, *112*(B8).

Shearer, P. M. (2009). *Introduction to seismology*. Cambridge University Press.

Sheng, J., Schuster, G. T., Pankow, K. L., Pechmann, J. C., & Nowack, R. L. (2003, December). Coherence-weighted wavepath migration of teleseismic data. In *AGU Fall Meeting Abstracts*.

Snyder, D. B. (2008). Stacked uppermost mantle layers within the Slave craton of NW Canada as defined by anisotropic seismic discontinuities. *Tectonics*, *27*(4).

Stein, S., & Wysession, M. (2009). *An introduction to seismology, earthquakes, and earth structure*. John Wiley & Sons.

Stoffa, P. L., Diebold, J. B., & Buhl, P. (1981). Inversion of seismic data in the τ-p plane. *Geophysical Research Letters*, *8*(8), 869-872.

Tull, J. F. (1978). Structural development of the Alabama Piedmont northwest of the Brevard zone. *American Journal of Science*, *278*(4), 442-460.

Tull, J. F. (1982). Stratigraphic framework of the Talladega slate belt, Alabama Appalachians. *Tectonic Studies in the Talladega and Carolina slate belts, Southern Appalachian Orogen: Geological Society of America, Special Paper*, *191*, 3-18.

Vauchez, A., & Barruol, G. (1996). Shear-wave splitting in the Appalachians and the Pyrenees: importance of the inherited tectonic fabric of the lithosphere. *Physics of the earth and planetary interiors*, *95*(3-4), 127-138.

Wagner, L. S., Long, M. D., Johnston, M. D., & Benoit, M. H. (2012). Lithospheric and asthenospheric contributions to shear-wave splitting observations in the southeastern United States. *Earth and Planetary Science Letters*, *341*, 128-138.

Wen, L., & Helmberger, D. V. (1998). Ultra-low velocity zones near the core-mantle boundary from broadband PKP precursors. *Science*, *279*(5357), 1701-1703.

Yang, Z., Sheehan, A. F., Yeck, W. L., Miller, K. C., Erslev, E. A., Worthington, L. L., & Harder, S. H. (2012). Imaging basin structure with teleseismic virtual source reflection profiles. *Geophysical Research Letters*, *39*(2).

Yu, J., & Schuster, G. T. (2001). Crosscorrelogram migration of IVSPWD data. In *SEG Technical Program Expanded Abstracts 2001* (pp. 456-459). Society of Exploration Geophysicists.

Yu, Y., Song, J., Liu, K. H., & Gao, S. S. (2015). Determining crustal structure beneath seismic stations overlying a low-velocity sedimentary layer using receiver functions. *Journal of Geophysical Research: Solid Earth*, *120*(5), 3208-3218.

Yuan, H., & Levin, V. (2014). Stratified seismic anisotropy and the lithosphere-asthenosphere boundary beneath eastern North America. *Journal of Geophysical Research: Solid Earth*, *119*(4), 3096-3114.

APPENDIX A

SESAME Station Information

Line D

Station	Latitude (degrees)	Longitude (degrees)	Cumulative distance (km) from northernmost station (plus 100 km)
D22	35.4629	-84.4588	100.000
D21	35.1997	-84.1369	129.201
D20	35.074	-83.9803	143.147
D19	34.8721	-83.7338	165.546
D18	34.7342	-83.6121	180.844
D17	34.6044	-83.4507	195.243
D15	34.4498	-83.2799	212.393
D14	34.3765	-83.1811	220.524
D13	34.2943	-83.1662	229.643
D12	34.2462	-83.0333	234.978
D11	34.1565	-82.9731	244.928
D10	34.0917	-82.9032	252.116
D09	34.0448	-82.8278	257.318

D08	33.9938	-82.7566	262.976
D07	33.9376	-82.6864	269.209
D06	33.859	-82.6304	277.928
D05	33.7915	-82.5159	285.415
D04	33.7301	-82.4518	292.225
D03	33.6594	-82.3884	300.067
D02	33.6041	-82.2828	306.201

Line W

Station	Latitude (degrees)	Longitude (degrees)	Cumulative distance (km) from furthest north station (plus 100 km)
W35	34.9762	-83.9438	100.000
W34	34.8376	-83.9204	115.376
W33	34.6547	-83.886	135.666
W32	34.4657	-83.8658	156.633
W315	34.1779	-83.8531	188.558
W31	33.9722	-83.7385	211.375
W30	33.7318	-83.9128	238.040
W29	33.4568	-83.7288	268.541
W28	33.1856	-83.8999	298.620
W27	32.9174	-83.9234	328.365
W26	32.79	-83.8917	342.494
W24	32.64	-83.8967	359.129
W23N	32.5234	-83.886	372.060
W22	32.4492	-83.8973	380.288
W21	32.404	-83.8587	385.300
W20	32.3665	-83.9198	389.459
W19	32.3132	-83.9064	395.370

W18	32.2725	-83.9017	399.883
W17	32.24	-83.9045	403.487
W16	32.1794	-83.8841	410.207
W15A	32.138	-83.8985	414.798
W14N	32.0938	-83.8987	419.699
W13	32.055	-83.8933	424.001
W12	32.0095	-83.8885	429.047
W11N	31.9587	-83.9083	434.680
W10N	31.9025	-83.8937	440.912
W09	31.8051	-83.8981	451.712
W08	31.7165	-83.886	461.536
W07	31.611	-83.911	473.234
W06	31.4486	-83.895	491.240
W05	31.2724	-83.8978	510.777
W04	31.0831	-83.8952	531.765
W03	30.8635	-83.8864	556.112
W02	30.5774	-83.8902	587.830
W01	30.2017	-83.9109	629.480

Line E

Station	Latitude (degrees)	Longitude (degrees)	Cumulative distance (km) from furthest north station (plus 100 km)
E31	32.9866	-82.107	100.000
E30	32.6958	-82.1091	132.250
E29	32.4908	-82.1032	154.984
E28	32.3359	-82.0967	172.162
E27	32.2362	-82.1091	183.218
E26	32.0979	-82.0991	198.554
E25	31.9918	-82.1135	210.319
E24	31.9445	-82.097	215.564
E23	31.8887	-82.0737	221.751
E22R	31.8477	-82.0899	226.297
E21	31.738	-82.071	238.461
E20	31.6967	-82.0796	243.041
E19	31.6177	-82.1113	251.800
E18	31.5665	-82.0996	257.477
E17	31.5016	-82.0986	264.673
E16	31.4505	-82.1299	270.339
E15	31.3632	-82.0969	280.019

E13	31.223	-82.0919	295.563
E12	31.1733	-82.088	301.074
E11	31.1074	-82.1019	308.380
E10	31.0673	-82.1013	312.826
E09	30.9839	-82.0742	322.073
E08	30.8388	-82.0717	338.160
E07	30.718	-82.0979	351.552
E06	30.5853	-82.0999	366.264
E05	30.3617	-82.1176	391.052
E04	30.0271	-82.1095	428.144
E03	29.8296	-82.1318	450.038
E02	29.443	-82.0674	492.891
E01	29.2116	-82.0545	518.539

APPENDIX B

Event Summary Tables

Date	Magnitude	Depth (km)	Latitude (degrees)	Longitude (degrees)	Array	End Member Stations (northernmost-southernmost)	Distance Range (degrees)	Arrival of PP after Direct Arrival (s)	Global Phase Arrival	Ray Parameter Range (s/km)
11/8/11	6.9	228 km	27.3	125.7	D	D17-D08	113-113	52-52	PKiKP	0.0172-0.0172
									PKIKP	N/A
									PKP	N/A
					W	W35-W01	112-116	47-68	PKiKP	0.0171-0.0174
									PKIKP	N/A-0.0172
									PKP	N/A
					E	N/A	N/A		N/A	N/A

Date	Magnitude	Depth (km)	Latitude (degrees)	Longitude (degrees)	Array	End Member Stations (northernmost-southernmost	Distance Range (degrees)	Arrival of PP after Direct Arrival (s)	Global Phase Arrival	Ray Parameter Range (s/km)
12/13/11	6.1	167 km	-0.05	123.1	D	D17-D02	138-139	171-175	PKiKP	0.0184-0.0184
									PKIKP	0.0164-0.0162
									PKP	N/A
					W	W35-W01	137-140	166-179	PKiKP	0.0184-0.0184
									PKIKP	0.0165-0.0161
									PKP	N/A
					E	N/A	N/A		N/A	N/A

Date	Magnitude	Depth (km)	Latitude (degrees)	Longitude (degrees)	Array	End Member Stations (northernmost-southernmost)	Distance Range (degrees)	Arrival of PP after Direct Arrival (s)	Global Phase Arrival	Ray Parameter Range (s/km)
12/14/11	7.1	129 km	-7.5	146.8	D	D17-D02	127-128	120-125	PKiKP	0.0180-0.0180
									PKIKP	0.0171-0.0170
									PKP	N/A
					W	W35-W01	126-127	115-120	PKiKP	0.0179-0.0180
									PKIKP	0.0171-0.0171
									PKP	N/A
					E	N/A	N/A		N/A	N/A

Date	Magnitude	Depth (km)	Latitude (degrees)	Longitude (degrees)	Array	End Member Stations (northernmost-southernmost)	Distance Range (degrees)	Arrival of PP after Direct Arrival (s)	Global Phase Arrival	Ray Parameter Range (s/km)
4/17/12	6.9	208 km	-5.5	147.1	D	D17-D02	125-126	112-116	PKiKP	0.0179-0.0180
									PKIKP	0.0172-0.0171
									PKP	N/A
					W	W35-W01	125-126	111-116	PKiKP	0.0179-0.0180
									PKIKP	0.0171-0.0171
									PKP	N/A
					E	N/A	N/A		N/A	N/A

Date	Magnitude	Depth (km)	Latitude (degrees)	Longitude (degrees)	Array	End Member Stations (northernmost-southernmost	Distance Range (degrees)	Arrival of PP after Direct Arrival (s)	Global Phase Arrival	Ray Parameter Range (s/km)
10/17/12	6.0	338 km	4.2	124.6	D	D22-D02	132-135	146-159	PKiKP	0.0182-0.0183
									PKIKP	0.0168-0.0166
									PKP	N/A
					W	W35-W01	133-136	151-163	PKiKP	0.0182-0.0183
									PKIKP	0.0168-0.0165
									PKP	N/A
					E	E31-E01	135-138	159-173	PKiKP	0.0183-0.0184
									PKIKP	0.0166-0.0163
									PKP	N/A

Date	Magnitude	Depth (km)	Latitude (degrees)	Longitude (degrees)	Array	End Member Stations (northernmost-southernmost	Distance Range (degrees)	Arrival of PP after Direct Arrival (s)	Global Phase Arrival	Ray Parameter Range (s/km)
4/6/13	7.0	66 km	-3.5	138.5	D	D22-D02	129-132	128-142	PKiKP	0.0181-0.0182
									PKIKP	0.0170-0.0168
									PKP	N/A
					W	W35-W02	130-132	133-142	PKiKP	0.0181-0.0182
									PKIKP	0.0169-0.0168
									PKP	N/A
					E	E31-E01	132-134	142-152	PKiKP	0.0182-0.0183
									PKIKP	0.0168-0.0167
									PKP	N/A

Date	Magnitude	Depth (km)	Latitude (degrees)	Longitude (degrees)	Array	End Member Stations (northernmost-southernmost	Distance Range (degrees)	Arrival of PP after Direct Arrival (s)	Global Phase Arrival	Ray Parameter Range (s/km)
7/7/13	6.6	62 km	-6.0	149.7	D	D22-D02	122-125	95-109	PKiKP	0.0177-0.0179
									PKIKP	0.0172-0.0171
									PKP	N/A
					W	W35-W01	123-124	100-105	PKiKP	0.0178-0.0178
									PKIKP	0.0172-0.0171
									PKP	N/A
					E	E31-E01	125-126	109-114	PKiKP	0.0179-0.0179
									PKIKP	0.0171-0.0171
									PKP	N/A

Date	Magnitude	Depth (km)	Latitude (degrees)	Longitude (degrees)	Array	End Member Stations (northernmost-southernmost	Distance Range (degrees)	Arrival of PP after Direct Arrival (s)	Global Phase Arrival	Ray Parameter Range (s/km)
7/7/13	7.3	386 km	-3.9	153.9	D	D22-D02	118-120	81-91	PKiKP	0.0175-0.0177
									PKIKP	0.0172-0.0172
									PKP	N/A
					W	W35-W01	118-120	81-91	PKiKP	0.0175-0.0177
									PKIKP	0.0172-0.0172
									PKP	N/A
					E	E31-E01	120-121	91-95	PKiKP	0.0177-0.0177
									PKIKP	0.0172-0.0172
									PKP	N/A

Date	Magnitude	Depth (km)	Latitude (degrees)	Longitude (degrees)	Array	End Member Stations (northernmost-southernmost	Distance Range (degrees)	Arrival of PP after Direct Arrival (s)	Global Phase Arrival	Ray Parameter Range (s/km)
8/12/13	6.0	95 km	-7.1	129.8	D	D22-D02	138-140	169-178	PKiKP	0.0184-0.0184
									PKIKP	0.0164-0.0161
									PKP	N/A
					W	W35-W01	138-141	169-183	PKiKP	0.0184-0.0185
									PKIKP	0.0164-0.0159
									PKP	N/A
					E	E31-E01	141-143	183-191	PKiKP	0.0185-0.0185
									PKIKP	0.0159-0.0157
									PKP	N/A

Date	Magnitude	Depth (km)	Latitude (degrees)	Longitude (degrees)	Array	End Member Stations (northernmost-southernmost	Distance Range (degrees)	Arrival of PP after Direct Arrival (s)	Global Phase Arrival	Ray Parameter Range (s/km)
1/25/14	6.1	66 km	-8.0	109.3	D	D22-D03	150-152	220-229	PKiKP	0.0186-0.0186
									PKIKP	0.0141-0.0134
									PKPab / PKPbc	0.0372-0.0378 / 0.0232-0.0213
					W	W35-W01	151-155	224-241	PKiKP	0.0186-0.0186
									PKIKP	0.0138-0.0123
									PKPab / PKPbc	0.0375-0.0385 / 0.0221-0.0189
					E	E31-E01	153-156	233-246	PKiKP	0.0186-N/A
									PKIKP	0.0131-0.0119
									PKPab / PKPbc	0.0381-0.0387 / 0.0205- N/A

Date	Magnitude	Depth (km)	Latitude (degrees)	Longitude (degrees)	Array	End Member Stations (northernmost-southernmost	Distance Range (degrees)	Arrival of PP after Direct Arrival (s)	Global Phase Arrival	Ray Parameter Range (s/km)
3/2/14	6.5	119 km	27.4	127.4	D	D22-D03	111-113	40-50	PKiKP	0.0170-0.0172
									PKIKP	N/A
									PKP	N/A
					W	W35-W01	112-115	45-60	PKiKP	0.0171-0.0173
									PKIKP	N/A-0.0172
									PKP	N/A
					E	E31-E02	114-117	55-70	PKiKP	0.0173-0.0174
									PKIKP	0.0172-0.0172
									PKP	N/A

Date	Magnitude	Depth (km)	Latitude (degrees)	Longitude (degrees)	Array	End Member Stations (northernmost-southernmost	Distance Range (degrees)	Arrival of PP after Direct Arrival (s)	Global Phase Arrival	Ray Parameter Range (s/km)
4/11/14	7.1	61 km	-6.6	155.0	D	D22-D03	119-121	79-90	PKiKP	0.0176-0.0177
									PKIKP	0.0172-0.0172
									PKP	N/A
					W	W35-W01	119-120	79-85	PKiKP	0.0176-0.0176
									PKIKP	0.0172-0.0172
									PKP	N/A
					E	E30-E02	121-122	90-95	PKiKP	0.0177-0.0177
									PKIKP	0.0172-0.0172
									PKP	N/A

APPENDIX C

Migration Event Tables

					Subsections												
Date	Magnitude	Depth (km)	Array	Filter Setting (Hz)	w1	w2	w3	w4	w5	w6	w7	w8	w9	w10	w11	w12	w13
12/13/11	6.1	167 km	D	0.25-2.0	D17-D14	D17-D13	D13, D11, D08, D05	D08, D05, D02									
				alpha=2	0.99	None	0.80	None									
					vel_inner_piedmont	N/A	vel_carolina_terrane	N/A									
			W	0.25-2.0	W35, W34, W32	W35, W34, W32, W31, W30	W31-W29	W28, W27, W24	W23-W10	W07, W06, W01	W09-W07						
				alpha=2	None	0.85	None	0.95	None	None	0.90						
					N/A	vel_blue_ridge	N/A	vel_inner_piedmont	N/A	N/A	vel_w06_w08						
			E	N/A	N/A	N/A	N/A	N/A	N/A	N/A	N/A						

12/14/11	7.1	129 km	D	0.25-2.0	D17-D13	D15-D13, D11	D13, D11, D08, D05	D08, D05, D02	D17-D13, D11, D08, D05, D02								
				alpha=2	0.99	0.95	0.85	0.99	0.65								
					vel_inner_piedmont	vel_inner_piedmont	vel_carolina_terrane	vel_carolina_terrane	vel_inner_piedmont								
			W	0.25-2.0	W35, W34, W32	W32, W31, W30	W31-W27	W24-W10	W24-W17	W19-W17	W16-W12	W09-W06	W06-W01				
				alpha=2	None	None	None	0.35	0.65	0.95	0.80	None	0.85				
					N/A	N/A	N/A	vel_w18_w21	vel_w18_w21	vel_w18_w21	vel_w14_w17	N/A	vel_w06_w08				
			E	N/A	N/A	N/A	N/A	N/A	N/A	N/A	N/A	N/A	N/A				

4/17/12	6.9	208 km	D	0.25-2.0	D17-D13	D15-D13, D11	D08, D05, D02										
				alpha=2	None	None	0.95										
					N/A	N/A	vel_carolina_terrane										
			W	0.25-2.0	W23-W19	W16-W13	W12-W09, W07	W06-W01	W35-W32	W30-W27	W15A-W11	W13-W09, W07	W09, W07-W01	W06-W04	W04-W02		
				alpha=2	0.95	0.90	0.85	0.80	0.95	0.95	0.80	0.80	0.75	0.99	0.95		
					vel_w18_w21	vel_w14_w17	vel_w09_w11	vel_w06_w08	vel_blue_ridge	vel_inner_piedmont	vel_w14_w17	vel_w09_w11	vel_w06_w08	vel_w06_w08	vel_w06_w08		
			E	N/A	N/A	N/A	N/A	N/A	N/A	N/A	N/A	N/A	N/A	N/A	N/A		

					Subsections												
Date	Magnitude	Depth (km)	Array	Filter Setting (Hz)	w1	w2	w3	w4	w5	w6	w7	w8	w9	w10	w11	w12	w13
10/17/12	6.0	338 km	D	0.25-2.0	D22-D20	D20-D18	D18-D15	D13-D09	D10-D04	D06-D02							
				alpha=2	None	None	0.99	0.80	0.65	None							
					N/A	N/A	vel_inner_piedmont	vel_carolina_terrane	vel_carolina_terrane	N/A							
			W	0.25-2.0	W25, W33, W32, W31	W30-W26	W23-W18	W16-W08	W06-W04	W04, W03, W01							
				alpha=2	0.90	0.80	0.65	0.65	None	None							
					vel_blue_ridge	vel_inner_piedmont	vel_w18_w21	vel_w12_w13	N/A	N/A							
			E	0.25-2.0	E31-E28	E29-E26	E26-E24, E21-E16	E21-E16	E13-E09	E07-E05	E05-E02	E03-E01					
				alpha=2	None	0.80	0.55	None	0.75	None	0.90	None					
					N/A	vel_e27_e29	vel_e07_e23	N/A	vel_e07_e23	N/A	vel_e01_e06	N/A					

4/6/13	7.0	66 km	D	0.25-2.0	D22, D21, D19	D19-D17	D15-D12	D13-D11	D09-D07	D07-D05	D06-D02						
				alpha=2	None	None	0.95	None	None	0.99	0.95						
					N/A	N/A	vel_inner_piedmont	N/A	N/A	vel_carolina_terrane	vel_carolina_tarrane						
			W	0.25-2.0	W35, W33, W32	W315-E30	W30-W28	W29-W27	W16, W15A, W13	W12-W08	W10-W07	W06-W02	W04-W02	W16, W15A, W13-W11			
				alpha=2	None	None	0.99	None	0.99	None	None	0.85	0.95	0.65			
					N/A	N/A	vel_inner_piedmont	N/A	vel_w14_w17	N/A	N/A	vel_w06_w08	vel_w06_w08	vel_w12_w13			
			E	0.25-2.0	E31-E29	E28-E24	E24, E20, E19	E19-E15	E13-E11	E10-E07	E06-E03	E03-E01					
				alpha=2	None	0.75	0.95	0.75	None	0.90	None	0.95					
					N/A	vel_e27_e29	vel_e07_e23	vel_e07_e23	N/A	vel_e07_e23	N/A	vel_e01_e06					

7/7/13	6.6	62 km	D	0.25-2.0	D22-D19	D18-D14	D15-D11	D09-D02	D06-D02								
				alpha=2	None	0.90	0.80	0.65	0.80								
					N/A	vel_inner_piedmont	vel_inner_piedmont	vel_carolina_terrane	vel_carolina_terrane								
			W	0.25-2.0	W19,W18,W16-W13	W10-W07	W06-W03	W35, W33, W32	W35, W33-W31	W315, W31, W29	W29-W27	W21, W19, W18, W16-W13	W16-W13	W03-W01			
				alpha=2	0.65	None	0.90	None	0.75	None	None	0.65	0.80	None			
					vel_w14_w17	N/A	vel_w06_w08	N/A	vel_blue_ridge	N/A	N/A	vel_w14_w17	vel_w14_w17	N/A			
			E	0.25-2.0	E30-E24	E21-E12	E11-E06	E31-E24	E30-E28	E29-E24, E21, E20	E27-E24, E21, E20	E19-E15	E13-E09	E10-E06	E05, E04, E02, E01		
				alpha=2	0.65	0.55	None	0.65	0.90	0.55	0.65	0.95	None	0.85	None		
					vel_e27_e29	vel_e07_e23	N/A	vel_e27_e29	vel_e27_e29	vel_e24_e26	vel_e24_e26	vel_e07_e23	N/A	vel_e07_e23	N/A		

7/7/13	7.3	386 km	D	0.25-2.0	D22-D20	D19-D14	D15-D12	D13-D11, D09	D08-D02	D04-D02	D06-D02						
				alpha=2	0.95	0.95	0.95	0.90	None	0.99	0.95						
					vel_blue_ridge	vel_inner_piedmont	vel_inner_piedmont	vel_carolina_terrane	N/A	vel_carolina_terrane	vel_carolina_terrane						
			W	0.25-2.0	W21, W19, W18	W16-W13	W11-W07	W35, W33-W31	W315, W31, W29, W27	W21, W19, W18, W16-W13, W11, W10	W21, W19, W18, W16-W13	W19, W18, W16-W13	W09-W02	W03-W01			
				alpha=2	0.95	None	0.80	0.90	0.95	0.65	0.85	0.90	0.65	None			
					vel_e18_e21	N/A	vel_w09_w11	vel_blue_ridge	vel_inner_piedmont	vel_e14_e17	vel_w14_w17	vel_e14_e17	vel_w06_w08	N/A			
			E	0.25-2.0	E30-E24	E21-E15	E13-E09	E08-E06	E31-E29	E30-E27	E29-E26	E26-E24	E21-E16	E21-E10	E13-E10	E13-E07	E06, E04, E02, E01
				alpha=2	0.65	0.65	None	None	0.95	0.80	0.90	None	0.65	0.55	None	0.80	None
					vel_e27_e29	vel_e07_e23	N/A	N/A	vel_e27_e29	vel_e27_e29	vel_e27_e29	N/A	vel_e07_e23	vel_e07_e23	N/A	vel_e07_e23	N/A

					Subsections												
Date	Magnitude	Depth (km)	Array	Filter Setting (Hz)	w1	w2	w3	w4	w5	w6	w7	w8	w9	w10	w11	w12	w13
8/12/13	6.0	95 km	D	0.25-2.0	D22-D20	D20-D18	D18-D15	D13-D11	D11, D09-D07	D09-D06	D04-D02						
				alpha=2	0.90	0.95	0.95	0.99	0.95	None	0.99						
					vel_blue_ridge	vel_blue_ridge	vel_inner_piedmont	vel_inner_piedmont	vel_carolina_terrane	N/A	vel_carolina_terrane						
			W	0.25-2.0	W35, W33-W31	W29-W27	W21, W19, W18, W16-W13, W11, W10	W11-W05	W06-W04	W03-W01							
				alpha=2	0.80	0.90	0.75	0.85	0.99	0.99							
					vel_blue_ridge	vel_inner_piedmont	vel_w14_w17	vel_w09_w11	vel_w06_w08	vel_w06_w08							
			E	0.25-2.0	E31-E28	E28, E25, E24	E21-E15	E13-E09	E08, E06, E04								
				alpha=2	0.90	None	0.65	None	0.99								
					vel_e27_e29	N/A	vel_e07_e23	N/A	vel_e01_e06								

4/11/14	7.1	61 km	D	0.25-2.0	D19-D15	D17-D14	D12, D10, D09	D07-D05	D09, D07-D05, D03	D22, D21, D19							
				alpha=2	0.99	None	0.95	None	None	None							
					vel_inner_piedmont	N/A	vel_carolina_terrane	N/A	N/A	N/A							
			W	0.25-2.0	W21-W18	W15A-W13	W11-W08	W315-W27	W23, W21-W18	W15A-W13, W11-W08	W15A-W13, W11-W08, W06, W05	W21-W18, W15A-W13					
				alpha=2	0.80	0.95	0.95	0.85	0.80	0.65	0.55	0.65					
					vel_e18_e21	vel_e14_e17	vel_w09_w11	vel_inner_piedmont	vel_e18_e21	vel_w09_w11	vel_w09_w11	vel_w18_w21					
			E	0.25-2.0	E30-E28	E22, E20-E18	E16-E13	E10-E08	E25, E24, E22, E20-E18	E22, E20-E18, E16-E13	E20-E18	E15, E13, E10	E05-E02				
				alpha=2	0.95	0.90	0.99	None	0.80	0.75	0.95	None	0.95				
					vel_e27_e29	vel_e07_e23	vel_e07_e23	N/A	vel_e07_e23	vel_e07_e23	vel_e07_e23	N/A	vel_e01_e06				

APPENDIX D

Velocity Models

Blue Ridge: SESAME Stations D18-D22, W32-W35 (vel_blue_ridge)

Layer Number	Slowness (s/km)	Depth to bottom of layer (km)
1	0.1872	0.1
2	0.1856	0.2
3	0.1841	0.3
4	0.1825	0.4
5	0.1810	0.5
6	0.1796	0.6
7	0.1781	0.7
8	0.1767	0.8
9	0.1753	0.9
10	0.1739	1.0
11	0.1725	1.1
12	0.1712	1.2
13	0.1699	1.3
14	0.1686	1.4

15	0.1673	1.5
16	0.1600	2.0
17	0.1599	2.5
18	0.1598	3.0
19	0.1597	3.5
20	0.1597	4.0
21	0.1596	4.5
22	0.1595	5.0
23	0.1591	7.0
24	0.1584	9.0
25	0.1577	11.0
26	0.1569	13.0
27	0.1562	15.0
28	0.1555	17.0
29	0.1548	19.0
30	0.1541	21.0
31	0.1534	23.0
32	0.1527	25.0
33	0.1521	27.0
34	0.1514	29.0

35	0.1507	31.0
36	0.1501	33.0
37	0.1494	35.0
38	0.1488	37.0
39	0.1481	39.0
40	0.1475	41.0
41	0.1468	43.0
42	0.1462	45.0
43	0.1456	47.0
44	0.1450	49.0
45	0.1444	51.0
46	0.1438	53.0
47	0.1432	55.0
48	0.1429	60.0
49	0.123457	300.0

Inner Piedmont: SESAME Stations D12-D17, W29-W315 (vel_inner_piedmont)

Layer Number	Slowness (s/km)	Depth to bottom of layer (km)
1	0.1642	0.1
2	0.1641	0.2
3	0.1641	0.3
4	0.1641	0.4
5	0.1640	0.5
6	0.1640	0.6
7	0.1639	0.7
8	0.1639	0.8
9	0.1639	0.9
10	0.1638	1.0
11	0.1638	1.1
12	0.1638	1.2
13	0.1637	1.3
14	0.1637	1.4
15	0.1636	1.5
16	0.1635	2.0
17	0.1633	2.5
18	0.1631	3.0

19	0.1629	3.5
20	0.1627	4.0
21	0.1626	4.5
22	0.1624	5.0
23	0.1619	7.0
24	0.1611	9.0
25	0.1604	11.0
26	0.1600	13.0
27	0.1599	15.0
28	0.1598	17.0
29	0.1597	19.0
30	0.1596	21.0
31	0.1595	23.0
32	0.1594	25.0
33	0.1594	27.0
34	0.1593	29.0
35	01592	31.0
36	0.1591	33.0
37	0.1590	35.0
38	0.1589	37.0

39	0.1588	39.0
40	0.1588	40.44
41	0.1587	45.0
42	0.123457	300.0

Carolina Terrane: SESAME Stations D02-D11 (vel_carolina_terrane)

Layer Number	Slowness (s/km)	Depth to bottom of layer (km)
1	0.1809	0.1
2	0.1791	0.2
3	0.1773	0.3
4	0.1755	0.4
5	0.1738	0.5
6	0.1721	0.6
7	0.1705	0.7
8	0.1689	0.8
9	0.1673	0.9
10	0.1658	1.0
11	0.1646	2.0
12	0.1640	3.0
13	0.1631	4.0
14	0.1625	5.0
15	0.1618	6.0
16	0.1611	7.0
17	0.1604	8.0
18	0.1597	9.0

19	0.1590	10.0
20	0.1583	11.0
21	0.1576	12.0
22	0.1570	13.0
23	0.1563	14.0
24	0.1557	15.0
25	0.1550	16.0
26	0.1544	17.0
27	0.1537	18.0
28	0.1531	19.0
29	0.1525	20.0
30	0.1518	21.0
31	0.1512	22.0
32	0.1506	23.0
33	0.1494	24.0
34	0.1490	25.0
35	0.1463	26.0
36	0.1462	27.0
37	0.1460	28.0
38	0.1458	29.0

39	0.1456	30.0
40	0.1454	31.0
41	0.1452	32.0
42	0.1450	33.0
43	0.1448	34.0
44	0.1447	35.0
45	0.1445	36.0
46	0.1444	37.0
47	0.1443	38.0
48	0.1442	39.0
49	0.123457	300.0

Coastal Plain: SESAME Stations W18-W21 (vel_w18_w21)

Layer Number	Slowness (s/km)	Depth to bottom of layer (km)
1	0.416667	0.58
2	0.250000	2.00
3	0.166667	4.98
4	0.163676	7.96
5	0.160791	10.94
6	0.158006	13.92
7	0.155316	16.90
8	0.152716	19.88
9	0.150201	22.86
10	0.147768	25.84
11	0.145413	28.82
12	0.143131	31.80
13	0.123457	300.00

Coastal Plain: SESAME Stations W14-W17 (vel_w14_w17)

Layer Number	Slowness (s/km)	Depth to bottom of layer (km)
1	0.416667	0.78
2	0.250000	3.73
3	0.166667	6.71
4	0.163676	9.69
5	0.160791	12.67
6	0.158006	15.65
7	0.155316	18.63
8	0.152716	21.61
9	0.150201	24.59
10	0.147768	27.57
11	0.145413	30.55
12	0.143131	33.53
13	0.123457	300.00

Coastal Plain: SESAME Stations W12-W13 (vel_w12_w13)

Layer Number	Slowness (s/km)	Depth to bottom of layer (km)
1	0.416667	1.07
2	0.250000	4.57
3	0.166667	7.55
4	0.163676	10.53
5	0.160791	13.51
6	0.158006	16.49
7	0.155316	19.47
8	0.152716	22.45
9	0.150201	25.43
10	0.147768	28.41
11	0.145413	31.39
12	0.143131	34.37
13	0.123457	300.00

Coastal Plain: SESAME Stations W09-W11 (vel_w09_w11)

Layer Number	Slowness (s/km)	Depth to bottom of layer (km)
1	0.416667	1.00
2	0.250000	5.20
3	0.166667	8.18
4	0.163676	11.16
5	0.160791	14.14
6	0.158006	17.12
7	0.155316	20.10
8	0.152716	23.08
9	0.150201	26.06
10	0.147768	29.04
11	0.145413	32.02
12	0.143131	35.00
13	0.123457	300.00

Coastal Plain: SESAME Stations W06-W08 (vel_w06_w08)

Layer Number	Slowness (s/km)	Depth to bottom of layer (km)
1	0.416667	1.25
2	0.250000	6.92
3	0.166667	9.90
4	0.163676	12.88
5	0.160791	15.86
6	0.158006	18.84
7	0.155316	21.82
8	0.152716	24.80
9	0.150201	27.78
10	0.147768	30.76
11	0.145413	33.74
12	0.143131	36.72
13	0.123457	300.00

Coastal Plain: SESAME Stations E27-E29 (vel_e27_e29)

Layer Number	Slowness (s/km)	Depth to bottom of layer (km)
1	0.416667	0.95
2	0.166667	3.93
3	0.163676	6.91
4	0.160791	9.89
5	0.158006	12.87
6	0.155316	15.85
7	0.152716	18.83
8	0.150201	21.81
9	0.147768	24.79
10	0.145413	27.77
11	0.143131	30.75
12	0.123457	300.00

Coastal Plain: SESAME Stations E24-E26 (vel_e24_e26)

Layer Number	Slowness (s/km)	Depth to bottom of layer (km)
1	0.416667	1.15
2	0.250000	2.40
3	0.166667	5.38
4	0.163676	8.36
5	0.160791	11.34
6	0.158006	14.32
7	0.155316	17.30
8	0.152716	20.28
9	0.150201	23.26
10	0.147768	26.24
11	0.145413	29.22
12	0.143131	32.20
13	0.123457	300.00

Coastal Plain: SESAME Stations E07-E23 (vel_e07_e23)

Layer Number	Slowness (s/km)	Depth to bottom of layer (km)
1	0.416667	1.30
2	0.166667	4.28
3	0.163676	7.26
4	0.160791	10.24
5	0.158006	13.22
6	0.155316	16.20
7	0.152716	19.18
8	0.150201	22.16
9	0.147768	25.14
10	0.145413	28.12
11	0.143131	31.00
12	0.123457	300.00

Coastal Plain: SESAME Stations E01-E06 (vel_e01_e06)

Layer Number	Slowness (s/km)	Depth to bottom of layer (km)
1	0.416667	1.06
2	0.166667	4.04
3	0.163676	7.02
4	0.160791	10.00
5	0.158006	12.98
6	0.155316	15.96
7	0.152716	18.94
8	0.150201	21.92
9	0.147768	24.90
10	0.145413	27.88
11	0.143131	30.86
12	0.123457	300.00

APPENDIX E

Processing Summary

JWEED

- Vertical components of live traces from the D, W, and E lines of the SESAME array were downloaded with a time window of 300 seconds before PKiKP and 600 seconds after the first S arrival.

SAC

- Direct arrivals were manually picked, and the time window of individual traces was shortened to a more suitable length of 20 seconds before the direct arrival and 180 seconds after.
- Individual traces were detrended and demeaned.

Seismic Unix/In-house Programs

- Multitrace gathers were formed with stations in the following order:

  -stations from the crystalline D line (northernmost-southernmost)

  -stations from the crystalline W line in the north followed by the traces from stations in the Coastal Plain

  -stations from the E line (northernmost-southernmost)
- SAC headers were stripped using in-house program “sacheaderstrip”
- Cross correlation static corrections were completed on the combined multitrace gathers to ensure a common time base.
- After static corrections, the combined multitrace gather was separated into individual gathers (D, W, and E) with a common time base.

- Source-time function estimates were determined by vertically stacking stations from the D line and the crystalline-rooted W line.

  -For distances 100-140 degrees, the entire stacked trace estimate was used, including any underside reflections.

  -For distances where PKIKP and PKiKP diverge (140-145 degrees), source-time function estimates were generated over small subsections of individual line gathers where the PKIKP and PKiKP slopes were similar. The traces included in this subsection were vertically stacked and zeroed out (after ~5-10 seconds depending on the magnitude of the event) to avoid removing reflections generated from structure during deconvolution.

- The stacked source-time function estimates were used to remove source effects through deconvolution.

  -All events were deconvolved with a water parameter of 0.0001 and an alpha range from 1-4.

  -Additionally, a highpass filter using a linear ramp from 0.25-0.75 Hz was applied.

  -The sampling interval for the SESAME array is 0.02 seconds.

- Small subsections from the deconvolved gathers were then slant stacked.

  -The ray parameter increment equals 0.001, and the ray parameter range of the slant stacks was -0.2 - +0.2.

  -A highcut filter of 0.5-1.0 Hz was applied to the semblance trace.

  -Coherency filtering was completed using smooth semblance (in-house program "sembmutebelownonormac") using a threshold range of 0.25-0.99.

  -The optimal threshold range was picked based on the suppression of pre-event energy.

- After slant stacks for subsections from the deconvolved gather were generated with their optimal semblance-based coherency thresholds, the slant stacks were either migrated or inverse slant stacked back into the time-distance domain.
- For migration, the slant stacks were limited to a ray parameter range of -0.05 - +0.05. Additionally, a Fresnel zone factor (fmult=0.1) was applied to help control the width of the resulting reflector. The average velocity used to compute the Fresnel zone radius was 7.4 km/s, and the dominant frequency used was 2 Hz.
- For inverse slant stacking, the slant stack for the optimal coherency threshold was limited to a ray parameter range of -0.05 - +0.05, and tapered in both time and distance to avoid introducing artifacts from sharp cutoffs of reflectors. Then the slant stack was inverse transformed using the in-house program "slantstackinversestation"; a mode of 2, indicating tau is the array center time, was selected and no velocity reduction was applied to the output traces. During the transformation back to the time-distance domain, high frequencies are lost; therefore, the time derivative of the Hilbert transform was applied to reintroduce them. However, the time derivative of the Hilbert transform also amplified high frequency noise, so a high cut filter of frequencies greater than 2 Hz was applied to temper this effect. Then these highcut, Hilbert transformed subsections for individual events along the profile lines of the SESAME array were recombined to produce a complete profile with noise suppressed.